

In situ TEM Observation of Metal-Graphene Interaction

Emi Kano

February 2017

In situ TEM Observation of Metal-Graphene Interaction

Emi Kano

Doctoral Program in Materials Science and Engineering

Submitted to the Graduate School of

Pure and Applied Sciences

in Partial Fulfillment of the Requirements

for the Degree of Doctor of Philosophy in

Engineering

at the

University of Tsukuba

Table of Contents

Table of Contents	i
Abstract.....	iv
Chapter 1 Introduction.....	1
1-1 Characterization of graphene by electron microscopy.....	1
1-1-1 Background.....	1
1-1-2 Electron irradiation effects	8
1-1-3 Objective of the research	11
1-2 Previous studies on graphene	12
1-2-1 Defects in graphene and their engineering	12
1-2-2 Interactions between metals and graphene	17
1-2-3 Originality of the thesis	19
1-3 Thesis outline	21
Chapter 2 Basic principles and experimental methods.....	22
2-1 Electron microscopy	22
2-1-1 Aberration corrector and our equipment component.....	22
2-1-2 Imaging mode (TEM, DF-TEM, STEM)	25
2-1-3 Electron energy-loss spectroscopy (EELS)	33
2-2 Principles of electron irradiation effects	35
2-2-1 Elastic and inelastic scattering.....	35
2-2-2 Energy transfer and binding energy of metal-carbon bond	36
2-2-3 Scattering cross section	38
2-3 Sample preparation	41
2-3-1 Chemical vapor deposition (CVD).....	41
2-3-2 Transfer process	43
2-3-3 <i>In situ</i> heating effects.....	49

Chapter 3 Cu atoms reknit graphene structure.....53

3-1 Introduction.....	53
3-2 Methods	54
3-2-1 Sample preparations	54
3-2-2 TEM imaging experiments	56
3-2-3 First-principles calculations	57
3-3 Results and discussion	58
3-3-1 Cu sites in single-layer graphene.....	58
3-3-2 Reconstruction of graphene.....	60
3-3-3 Transformations promoted by Cu atoms	64
3-3-4 Driving force of the transformations	69
3-3-5 Uniqueness of Cu compared with other transition metals.....	71
3-4 Summary.....	73

Chapter 4 Metal-mediated mending and etching of graphene edges74

4-1 Introduction.....	74
4-2 Methods	75
4-3 Results.....	76
4-4 Discussions	79
4-4-1 Binding energy of metal-carbon bond.....	79
4-4-2 Effects of heating and irradiation	79
4-5 Summary.....	80

Chapter 5 Metal-terminated carbynes on graphene81

5-1 Introduction.....	81
5-2 Methods	82
5-3 Results and discussion	83
5-3-1 Formation and dynamics of carbyne	83

5-3-2 Bending strength of carbyne.....	86
5-3-3 Role of Pt and Cu atoms	87
5-4 Summary	87
Chapter 6 2D copper oxide on graphene	88
6-1 Introduction.....	88
6-2 Methods.....	89
6-2-1 STEM-EELS experiments	89
6-2-2 First-principles calculations.....	90
6-3 Results and discussion	91
6-3-1 STEM-EELS observations	91
6-3-2 DFT calculations and image simulations.....	95
6-3-3 Properties of 2D copper oxide	97
6-4 Summary	98
Conclusions.....	99
Appendix.....	102
List of Figures and Tables	111
List of Abbreviations.....	114
List of Publications	115
References	118
Acknowledgements	136

Abstract

Graphene is a two-dimensional (2D) crystalline form of carbon with a honeycomb lattice structure. It is the fundamental structure of layered bulk graphite and some nanocarbon materials, such as carbon nanotubes. The successful isolation of graphene has greatly influenced the nanocarbon research and has opened a new field of layered 2D materials. Recently, interactions of graphene with metal atoms and clusters have been studied aiming to control the local properties of graphene for applications in electrocatalysts and nanoelectronic devices. Alternatively, placing metal clusters on graphene could lead to the formation of novel low-dimensional nanostructures. Using transmission electron microscopy (TEM), we can directly monitor metal-graphene interactions without the effects of bulk substrate. Atomic-resolution imaging of individual atoms in graphene lattice has become available, due to the recent development in graphene synthesis and spatial resolution improvement brought by correcting aberrations of electron microscope lens.

This thesis investigates structure and interaction dynamics of metal atoms with graphene by atomic-resolution TEM. Previous studies reported that most metal atoms, which strongly interacted with graphene, promoted etching of graphene under electron irradiation. This phenomenon is generally detrimental for the fabrication of graphene-based nanoelectronic devices; on the other hand, it offers a promising method of graphene patterning and of producing graphene nanoribbons. Defects or impurity-doping in graphene is sometimes beneficial for chemical and electrochemical fields, where they can offer active sites for catalysis. It is therefore essential to visualize defect structure of graphene interacting with different chemical elements. Based on our results, we propose that binding energy of metal-C bonds is one of the key factors whether metal atoms can promote structural changes in graphene.

In this thesis, we investigate noble metals, Cu, Pt and Au, because they are promising elements for single-atom catalysis. Cu is known to be the best catalyst for graphene growth, and therefore is expected to catalyze the growth or modification of other carbon nanostructures. Indeed, we found that substitutional Cu atoms promote reconstruction of single-layer graphene, which had been not reported for other metals. During observation, we heated the sample at 150–300 °C to reduce hydrocarbon contamination. In general, thermal energy is a decisive factor of natural movements. However, we found that the energy required for the observed transformations was significantly higher than the energy arising from *in situ* heating at the aforementioned temperatures,

so that we conclude that the transformations were not induced by sample heating but by electron irradiation. We operated microscope at a low accelerating voltage of 80 kV to reduce knock-on damage of graphene, yet the incident electrons can transfer some of their energy to C atoms, which is sufficient to modify graphene structure in the presence of Cu atoms. Furthermore, we found that Cu, Pt and Au atoms at graphene edges behave differently: Cu atoms mend graphene edges, Pt atoms etch them, while Au atoms diffuse away from defects rather than affect the graphene structure. Our results suggest that doping different metals in graphene lattice or at graphene edges, combined with high-energy electron beam irradiation, allows us to control the graphene sheet morphology.

In addition to the above-mentioned phenomena, we observed self-assembly of two low-dimensional structures, namely, *metal-terminated carbynes* (monoatomic linear carbon chains) and *one-atom-thick 2D copper oxide with a square lattice*. In the formation of these novel nanostructures, graphene acted as a support membrane, an ultimate thin film for the visualization of materials by TEM. Defects or dopant metal atoms in graphene play an important role in providing nucleation sites. A great advantage of the observed formation is that metal-terminated carbyne chains and 2D copper oxide clusters are built up from single atoms: such a bottom-up approach offers the possibility to synthesize desired nanostructures in parallel rather than in sequentially.

In summary, we report two fundamental phenomena promoted by metal atoms interacting with graphene, using aberration-corrected TEM operated at 80 kV. The first phenomenon shows various structural changes in graphene lattice that were induced by a simultaneous presence of substitutional metal atoms and electron beam irradiation. The second reported phenomenon is the self-assembly of novel low-dimensional structures supported by graphene. Both phenomena are assisted by electron irradiation, which affects light C atoms much more than heavy metal atoms. The 80 keV electron beam irradiation offers energy required to induce the structural transformations in graphene. It also promoted migration of source atoms to create novel low-dimensional materials. Our results provide fundamental insight into the structure of graphene with metal atoms, and offer a promising method of producing nanostructures for a variety of potential applications.

Chapter 1

Introduction

The first section (1-1) introduces general and historical background of electron microscopy investigations of graphene followed by discussion of objectives of this thesis. The second section (1-2) summarizes relevant previous research that influenced our research. The outline of the thesis are concisely described in the last section (1-3).

1-1 Characterization of graphene by electron microscopy

The first subsection describes historical background of graphene research, followed by discussion of the importance of electron microscopy and its recent development. Then we examine the energy scale of electron-beam-induced transformations, since the effect of electron beam irradiation on graphene with noble metal atoms is the most important physics basis for our research. The last subsection is a motivation and objective of our research. For simplicity, technical methods of imaging and sample preparation are explained in Chapter 2, so that this section would make readers understand the essence of this thesis.

1-1-1 Background

Graphene is, strictly speaking, one-atom-thick 2D crystalline form of carbon with a honeycomb structure. It was first prepared by Geim and Novoselov via exfoliation from bulk graphite in 2004 (Figure 1-1, [1]). In their own words “Graphene is a rapidly rising star on the horizon of materials science and condensed-matter physics” [2]. Graphene has attracted tremendous attention since 2004, resulting in a Nobel Prize in Physics in 2010 for Geim and Novoselov. As shown in Figure 1-1(e), one-atom-thick single-layer graphene is the fundamental structure of some other forms of carbon, such as layered bulk graphite and one-dimensional carbon nanotube (CNT), which is a rolled graphene sheet [3]; it is also related to the zero-dimensional spherical carbon molecules, fullerenes [4]. CNTs and fullerenes have been discovered and intensively studied in the 1980–1990s. The interest to them has gradually declined in the 2000s, but has been reinvigorated by the

successful isolation of graphene. In turn, the vast amount of results obtained on CNTs and fullerenes did support and accelerate the graphene research. In this way, graphene has quickly advanced in the nanocarbon field.

The number of researchers has been increasing year by year, because graphene is a promising material for a variety of novel applications: such as nanoelectronic devices [1], [5]–[10], transparent electrodes [11]–[14], support membrane for nanocatalysts [15]–[27], gas sensors [28], [29] and so on. Furthermore, a variety of 2D materials have been found from their bulk layered counterparts in the same way as graphene: single-layer 2D materials can maintain its structure because of strong covalent bonding within a layer, whereas the weak van der Waals forces acting between the layers allow the separation of the material into 2D sheets. Recently 2D materials without layered bulk counterparts have also been found, as described in Chapter 6).

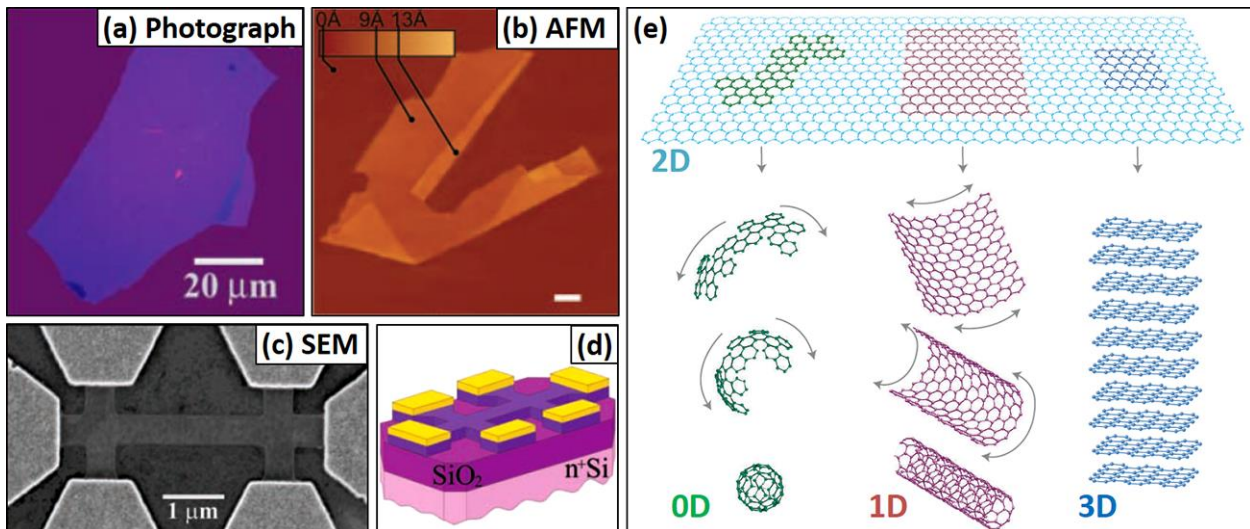


Figure 1-1 Graphene isolation and its structure

Exfoliated graphene images observed by (a) optical microscopy and (b) atomic force microscopy (AFM). (c), (d) Scanning electron microscopy (SEM) image and corresponding schematic of a graphene-based nanoelectronic device. (e) Schematic relation between the 2D graphene sheet and other carbon materials: graphene can be wrapped up into zero-dimensional (0D) fullerene, rolled into one-dimensional (1D) CNT or stacked into three-dimensional (3D) graphite. (a), (c) and (d) are reproduced from Ref. [1], (b) is from Ref. [30] and (e) is from Ref. [2].

Introduction

The enthusiasm for graphene resulted in the remarkably rapid progress in research of graphene and other low-dimensional materials. Nevertheless, graphene-based electronic devices or catalysts are still far from practical application, mostly because methods to obtain desirable forms of graphene are not established yet. For example, the properties of graphene-based nanoelectronic devices are strongly affected by structural defects of graphene (i.e. grain boundaries, impurities, vacancies or dislocations). Alternatively, nanocarbon materials were etched or destroyed by the catalytic activity of metal nanoparticles upon heating in hydrogen or oxygen gas atmosphere. In general, defects decrease mechanical strength and electrical conductivity (Figure 1-2(a), refs. [31], [32]). On the other hand, defects may open new research areas. First, some specific grain boundaries can improve electrical properties of graphene (Fig. 1-2(b), refs. [8], [9], [33]). Second, nano-engineered graphene forms, such as graphene nanoribbons [34]–[38] and graphene quantum dots [39]–[41], are promising materials because of their variable and versatile properties that depend on the material size and edge structure (Figs. 1-2 (c) and (d)). Third, nano-scale pores (nanopores) in graphene can be utilized for DNA sequencing, ion sensors and water desalination (Fig. 1-2(e), refs. [42]–[58]). Finally, defects, such as vacancies or impurities, are essential for chemistry and electrochemistry, where they can offer active sites for catalysis (Fig. 1-2(f), refs. [22], [59]–[77]). Assembling defects in desirable configurations would be beneficial for all the applications mentioned above. A first step in learning how to assemble desired structures is to visualize their behavior under well-controlled conditions. Therefore, it is essential to visualize structures of graphene defects (such as vacancies, dislocations, edges, dopant atoms, etc.) and to understand the mechanisms involved in fabricating such structures.

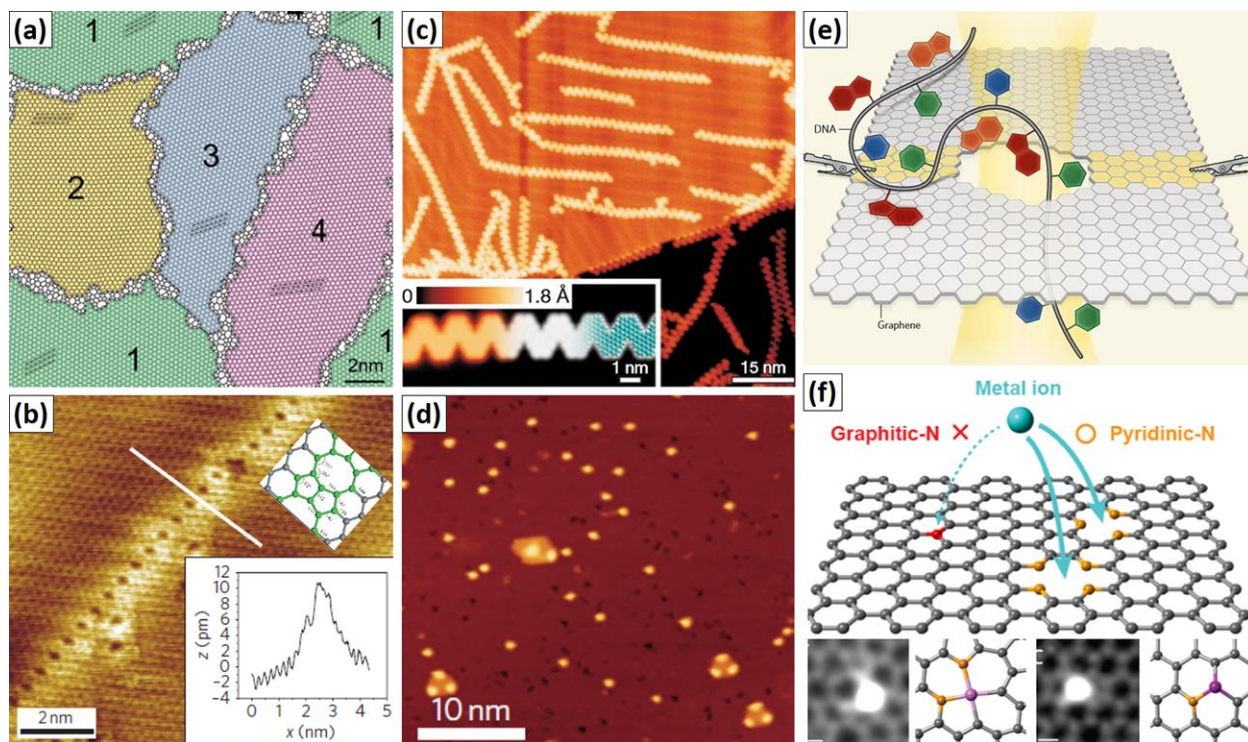


Figure 1-2 Effective utilization of defects in graphene

(a) Atomic model of grain boundaries in polycrystalline graphene [31]. (b) Scanning tunneling microscopy (STM) image of grain boundary that acts as a metallic nanowire [33]. (c) STM image of graphene nanoribbons fabricated by bottom-up method [34]. (d) STM image of graphene quantum dots produced from C_{60} [39]. (e) Schematic of DNA sequencing by graphene nanopores [42]. (f) Pyridinic-nitrogen enhanced adsorption of metal atoms on graphene [74].

Many characterization techniques have been utilized to investigate graphene. Optical microscopy, Raman spectroscopy, SEM, and AFM are important tools for probing the properties of micro- and nano-scale structures. STM and TEM can analyze graphene at the atomic scale. STM is suitable for observation of nanostructures placed on flat substrates as well as their local electronic structure, but generally requires long measurement time. On the other hand, using TEM we can observe free-standing graphene without the effect of a support substrate. TEM provides atomic scale spatial resolution and better time resolution, which are suitable for imaging the structure and dynamics at the atomic scale in real time.

Two recent key developments made it possible to observe individual atoms in single-layer graphene by TEM. The first key development for atomic-resolution imaging is the aberration

Introduction

corrector, which dramatically improves spatial resolution of electron microscopies by reducing the spherical aberration of the lenses. Electron microscopy is a relatively new and growing field compared to other fields in physics. Although Ruska first constructed the prototype electron microscopy in 1931, multipole-based aberration correctors became commercially available only in the late 1990s [78], [79]. Using such correctors, atomic-resolution imaging of graphene was first reported in 2008 by two groups: Meyer *et al.* [80] and Gass *et al.* [81]. As shown in Fig. 1-3, the former group observed detailed structure of graphene in the conventional BF-TEM mode, while the latter performed scanning TEM (STEM) imaging combined with electron energy-loss spectroscopy (EELS).

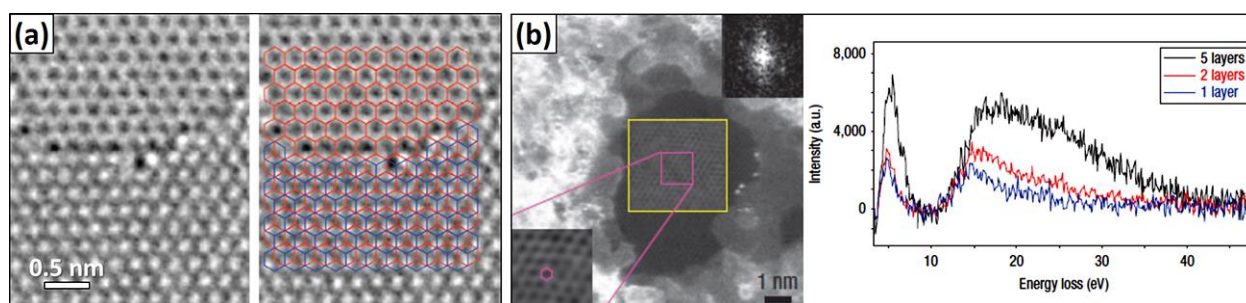


Figure 1-3 Atomic-resolution imaging of graphene in an electron microscope

Atomic structure of graphene observed by (a) TEM and (b) STEM-EELS, reproduced from Refs. [80] and [81], respectively. Image in (a) shows a step between a single-layer (upper part) and a double-layer area (lower part of the image), where the double-layer region exhibited general Bernal (AB) stacking. Image in (b) is an annular dark-field (ADF) STEM image of single-layer graphene, and EEL spectra taken from nearby areas with 1–5 layers thickness.

Another key progress expanding graphene research and potentially leading to applications is availability of reproducible graphene synthesis and sample preparation methods for the experiments. The mechanical exfoliation from graphite is a convenient and simple method to obtain high-quality graphene. The disadvantage is that it only allows to obtain small pieces with lateral dimensions from a few nanometers to a few micrometers. Obtaining free-standing graphene in large area is desirable not only for applications, but also for TEM studies. In 2009, Li *et al.* reported that single-layer graphene can uniformly grow on the entire surface of a Cu foil by chemical vapor deposition (CVD) [82]. They also demonstrated that it can be transferred onto an arbitrary substrate by wet etching method using poly(methyl methacrylate) as a support membrane

[12]. Using CVD graphene grown on a Cu foil followed by wet etching transfer, Bae *et al.* also reported that predominantly single-layer graphene can be produced on an industrial scale (Figure 1-4, [11]). The transfer of graphene onto TEM grids has also been investigated [13], [83]–[85]. Graphene requires special treatment that is different from treatment of typical TEM samples prepared from the bulk, for example by ion milling or microtome cutting. In particular, experiments on graphene are more sensitive to contamination; only a small amount of hydrocarbon residue will disturb atomic-resolution imaging. Sample preparation methods are elaborated in section 2-3.

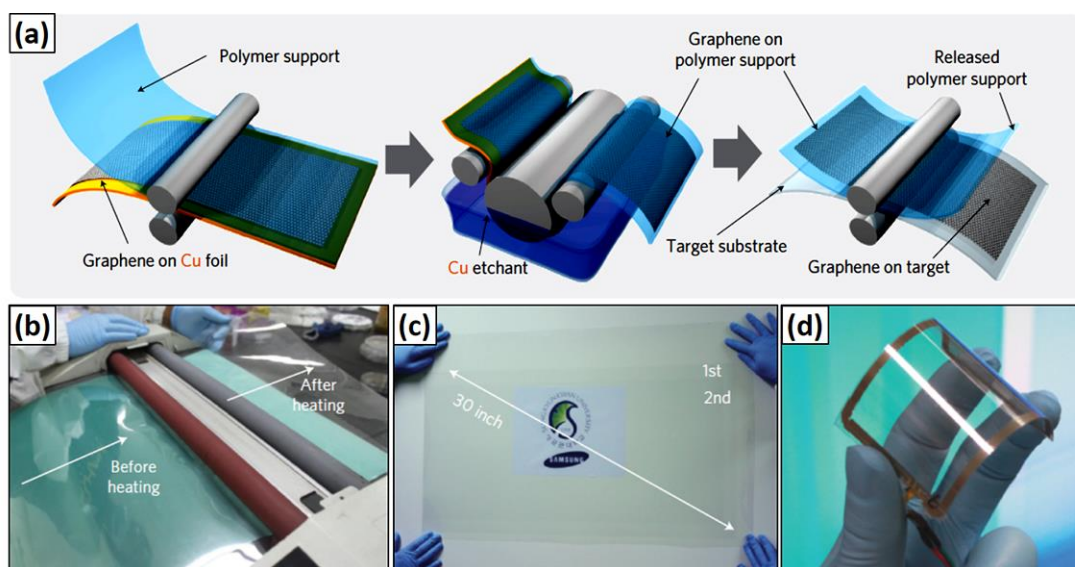


Figure 1-4 Roll-based production of graphene [11]

(a) Schematic of roll-to-roll transfer processes of graphene and (b–d) photographs taken during graphene transfer, after transfer onto a PET film and an assembled graphene/PET touch panel, respectively.

As shown above, the synthesis, transfer, and electron microscopy characterization techniques of graphene have progressed simultaneously and very rapidly starting around 2008–2010. This is because many experimental techniques for CNTs were also suitable for graphene — the CVD equipment is nearly identical for the CNT and graphene synthesis, and electron-irradiation effects on graphene and CNT are also very similar; therefore, many CNT researchers could immediately start studying graphene using the same equipment. Japanese scientists pioneered the study of CNTs both in synthesis and characterization; Endo and his co-workers synthesized multi-walled CNTs in 1976 [86] and Iijima determined the structure of single-walled and multi-walled CNTs via TEM

Introduction

in 1991 [3]. As a result, many outstanding experimentalists in Japan became interested in nanocarbon materials and Japan has been leading the field ever since [87]–[94]. While there are too many to be listed here, the group of Suenaga, which collaborates with Iijima, is famous for atomic-resolution imaging and spectroscopy of carbon nanostructures at low accelerating voltages down to 15 kV (Figure 1-5, refs. [74], [95]–[109]). Their research is conducted in collaboration with JEOL Ltd., a Japanese TEM manufacturer.

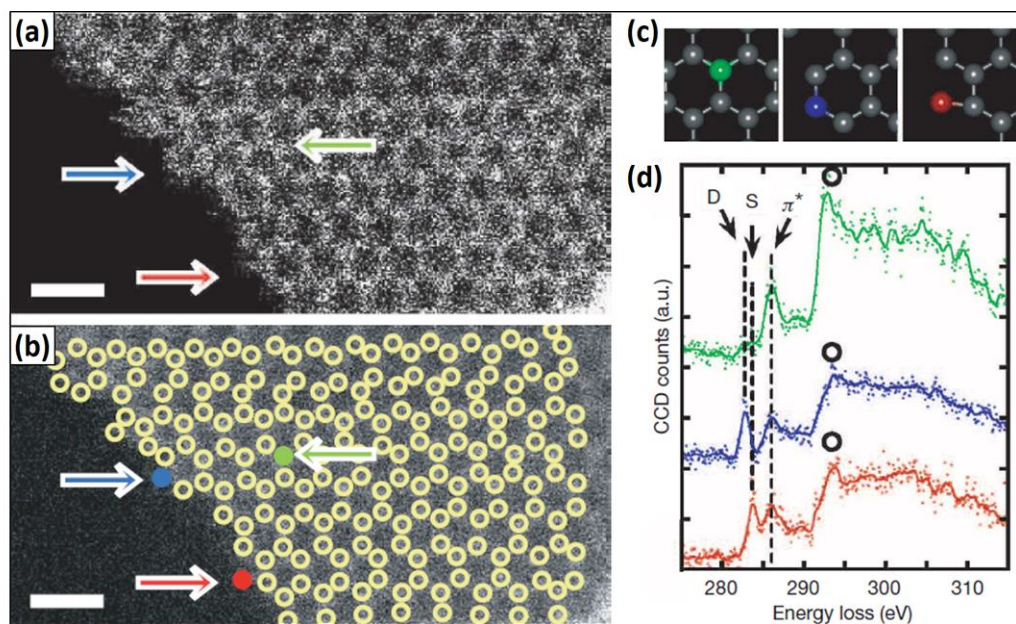


Figure 1-5 Single-atom spectroscopy at graphene edge [99].

(a) A raw ADF-STEM image taken at 60 kV. (b) Low-pass filtered image of (a) with markers indicating C atomic positions. (c) Atomic models of bulk sp^2 C atom (green) and edge atoms (blue and red). (d) EEL spectra of carbon K (1s) edge taken at the color-coded atoms in (b).

1-1-2 Electron irradiation effects

Here we describe main driving force of the structural changes observed during TEM experiments; that is, energy transfer to the C atoms from high-energy incident electron beam. The principles and equations are further described in section 2-2.

Transmission electron microscopes use beams of electrons that are typically accelerated to 80–300 keV for materials science research. When a high-energy incident electron is elastically scattered by an atomic nucleus, it transfers a small part of its energy to the nucleus. The maximum amount of energy transfer is determined by two factors:

- (1) Incident electron energy (E)
- (2) Mass number (A) of the scattering nucleus.

Since the knock-on threshold of atoms is determined by their binding energy, it is essential to use low accelerating voltage to reduce incident electron energy (factor (1)), so that atoms cannot be displaced from the graphene lattice. Large amount of energy can be transferred from incident electrons to light elements such as C atoms, while energy transfer to metal elements such as Cu is small due to its high atomic number (factor (2)). The table in Figure 1-6 summarizes the maximum value of energy transfer to C and Cu for incident energies of 80 keV and 200 keV.

Graphene benefits from its high mechanical strength originating from sp^2 -hybridized bonding. The knock-on threshold energy of a C atom from perfect graphene lattice is ~ 22 eV (Fig. 1-6(a), [110], [111]), which is ~ 4 times higher than that for amorphous carbon materials. Owing to its high thermal conductivity and high electrical conductivity, graphene does not suffer from a temperature increase or electronic excitation arising from inelastic scattering of high-energy electrons, whereas amorphous carbon or biomaterials are often damaged by them. Nevertheless, high-energy incident electrons can destroy graphene via energy transfer from elastic scattering.

The maximum value of energy transfer to C at an accelerating voltage of 200 kV is ~ 44 eV. Therefore, we have to use low accelerating voltage to prevent undesired damage to the sample. To reduce the maximum energy transfer below the 22 eV threshold, the incident energy needs to be about 110 keV or lower. Owing to the development of aberration correctors, we can routinely perform atomic-resolution imaging using low accelerating voltages of 60–80 kV, and microscopes with much lower voltages (~ 15 –40 kV) are currently being developed and are available in some

laboratories [108], [109]. Our microscopes (JEM-ARM200F, JEOL) can operate at 60–200 kV. We used 80 kV for the research reported here.

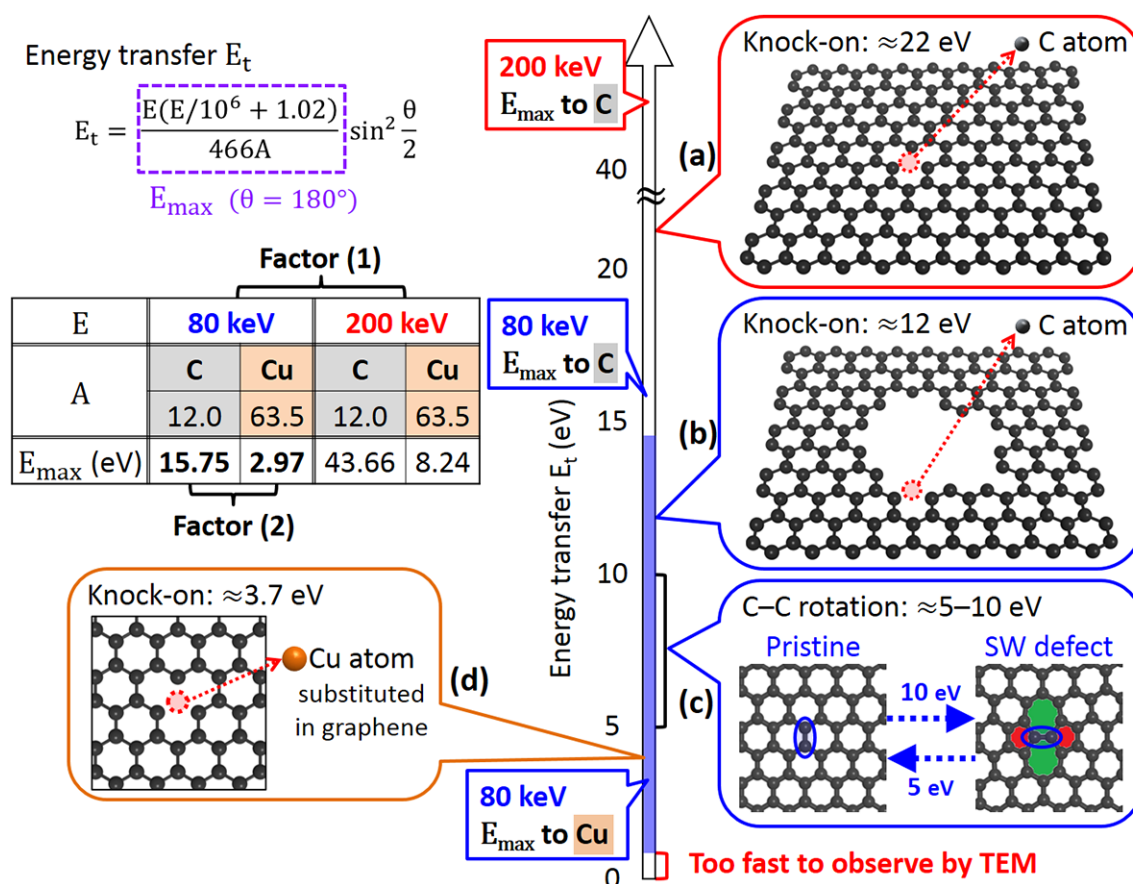


Figure 1-6 Energy-transfer and defect formations in graphene

The equation and table show the maximum value of energy transfer to C and Cu atoms for incident energies of 80 keV and 200 keV, where scattering angle $\theta = 180^\circ$. (a–d) Schematics of typical deformations in graphene: C displacement from (a) perfect graphene lattice and (b) graphene edges, (c) rotation of C–C bond, and (d) Cu displacement from graphene. Blue shaded energy area (~ 1 – 15 eV) can be observed by TEM at time resolution 1 s and incident electron beam current density $j = 10^5$ e $^-$ /s \cdot \AA^2 .

The 80 keV energy electrons can transfer up to ~ 15.7 eV to C atoms. While this value is lower than the knock-on threshold in perfect graphene, it is sufficiently high to dislocate or remove atoms at graphene edges (Fig. 1-6(b)) because of fewer bonds. A threshold energy of ~ 12 eV for the displacement at edges corresponds to ~ 62 keV incident electron energy. Furthermore, even in a perfect graphene lattice, electron irradiation can induce in-plane 90° rotation of C–C bond. Such rotation converts four hexagons into two pentagon-heptagon pairs, referred to as Stone-Wales

Chapter 1

(SW) defects. There is no loss of C atoms in this rotation, hence the energy threshold for this mechanism is low: ~ 10 eV for defect formation and ~ 5 eV for its relaxation (Fig. 1-6(c)) [112], corresponding to incident electron energy of 52 keV and 26 keV, respectively.

The stability of substitutional impurity atoms in graphene also depends on incident electron energy (factor (1)) and their atomic mass numbers (factor (2)). The 80 keV energy electrons can transfer up to ~ 2.97 eV to Cu atoms. This value is lower than the binding energy between substitutional Cu atom and graphene (~ 3.5 – 3.9 eV [113], [114]); therefore, Cu atoms cannot be displaced by 80 keV electron irradiation (Fig. 1-6(d)). However, impurity doping results in a reduction of energy requirements for C displacements. For example, C atoms next to Cu atoms have two strong C–C bonds (~ 5.2 eV/bond) and one weak C–Cu bond (~ 1.3 eV/bond); therefore, C atoms next to Cu atoms can be dislocated or removed due to elastic scattering at C atoms. That means, all of the aforementioned threshold values (Figs. 1-6(a)–(c)) reduced in the presence of impurity atoms.

To reduce radiation damage, researchers reduce electron beam current density by several orders of magnitude [115], [116]. Indeed ideal graphene would not be damaged, if we used 100 times lower electron irradiation dose. However, the resulting image would be too noisy. Furthermore, low-dose imaging cannot entirely prevent the defect formations, especially when graphene contains defects or impurities.

In this thesis, we utilized electron irradiation to induce structural changes in metal-doped graphene. The incident electron beam current density was $\sim 5 \times 10^4 - 1 \times 10^6$ e⁻/s·Å², which is higher than in most other reports. At this beam current density, various transformations could be observed at defect sites, and atomic-resolution imaging could be performed with a satisfactory signal-to-noise ratio. We observed various transformations because C atoms experienced a wide range of energy transfer (~ 1 – 15 eV) at different time intervals.

Having perfected the imaging tools for graphene characterization, we turned our attention to novel low-dimensional materials formed on graphene. The diffusion energy barriers of physisorbed metal atoms on graphene are typically below 0.5 eV, and those of the studied noble metals (Cu, Pt, Au) are far below 0.1 eV [117]. Hence it is not possible to observe physisorbed atoms on graphene surface by TEM, as they diffuse too fast under electron beam irradiation. Nevertheless, when atoms find suitable sites to chemisorb (i.e. edges, dislocations or substitutional

Introduction

metal atoms), they become sufficiently stable for TEM imaging. The chemisorbed atoms further trap other atoms, which allows direct observation of the self-assembly of novel low-dimensional structures.

1-1-3 Objective of the research

- (1) Understanding the structure of metal-doped graphene at the atomic scale
- (2) Direct observation of electron-induced transformations in graphene with different elements
- (3) Direct observation of self-assembly of novel low-dimensional structures, using graphene as a support membrane

We strived to visualize and control novel structures, such as defects, edges, and atomic- or nano-scale clusters. Interaction between metal and C atoms assisted by the electron beam irradiation presents interesting phenomena. Aberration-corrected TEM allows to induce moderate structural change in graphene, while retaining an atomic resolution.

1-2 Previous studies on graphene

In recent years, more than 70 papers about graphene have been published every day. Hence, this section introduces only selection of the most relevant studies. In particular, subsection 1-2-1 discusses defect engineering and subsection 1-2-2 reviews metal-graphene interactions. The third subsection (1-2-3) outlines the originality of this thesis compared to the previous reports.

1-2-1 Defects in graphene and their engineering

No material in nature is perfect and presence of defects needs to be considered. As is described in the first section, understanding the defect structure is extremely important, because it significantly influences mechanical, chemical, electronic and magnetic properties of a material. Typical defects of nanocarbon materials have been intensively studied. CNTs have been investigated for several decades, while graphene has investigated only for several years.

At first, we describe the difference between graphene and other nanocarbon materials. An argument about the knock-on threshold by electron irradiation attracted significant attention in the research community [80], [87], [110], [111], [118]–[122]. Recently it has been accepted that the knock-on threshold is lower for curved-shape graphene forms, such as CNTs or fullerenes, than for planar graphene. This is because the curvature significantly strains the structure and thus lowers the formation energies of defects (Fig. 1-7). Experimental studies on nanocarbon materials started from CNTs and therefore the reported experimental values (~15–20 eV) were smaller than the theoretical values for the ideal graphene (~22 eV).

A decrease in damage threshold energy also occurs at defects or at grain boundaries. Figure 1-8 shows typical point defects and their reconstruction mechanisms. SW defects shown in Fig. 1-8(a) are well known, because they are common to other carbon materials [122]. Robertson, Warner and their co-workers [118], [123] reported irradiation-induced reconstructions of vacancies, where various types of SW defects can be created. C atoms around a single vacancy (Fig. 1-8(b)) have dangling bonds, which result in a reconstruction of the vacancy via a geometric Jahn-Teller distortion, and 5- and 9-membered rings are constructed [123], [124]. The two panels shown in Fig. 1-8(c) are reconstructed structure from a double vacancy. Double vacancy and its reconstructed structure are observed more frequently rather than a single vacancy, because single

vacancy has unstable atoms with dangling bonds and one of the atoms at the edge can be easily removed by electron irradiation, due to low knock on threshold ~ 14 eV [110].

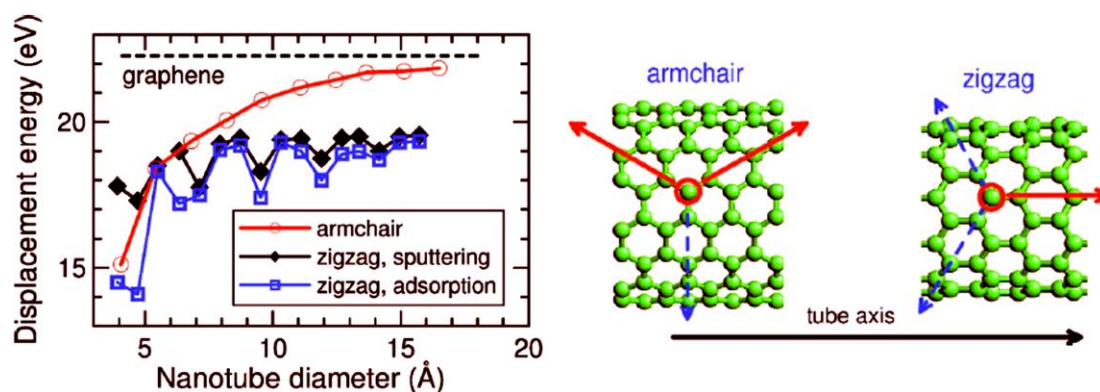


Figure 1-7 Decrease of knock-on energy threshold due to curvature in CNTs [110]

Knock-on threshold energy of a C atom from single-walled CNT and graphene calculated as a function of tube diameter. The images on the right panels show the corresponding atomic models of armchair and zigzag nanotubes.

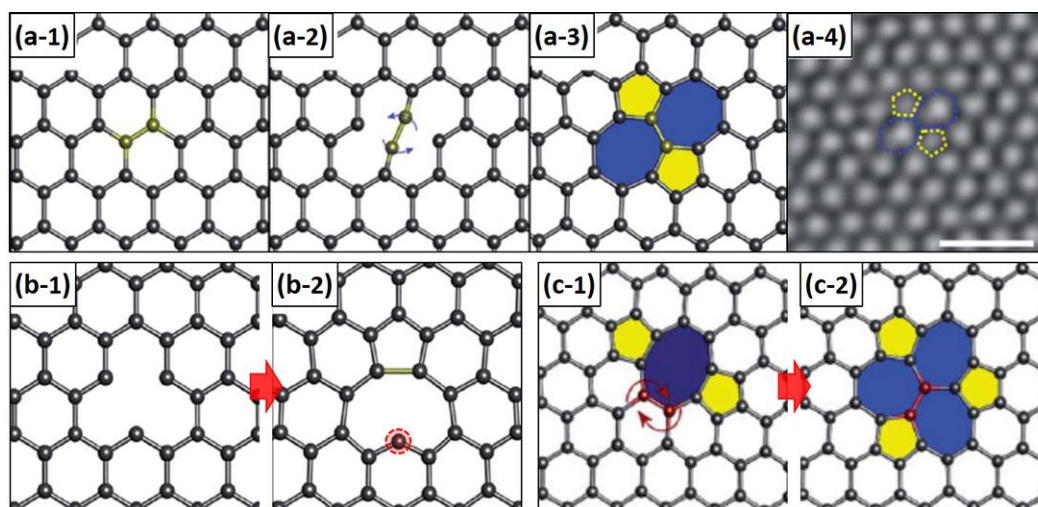


Figure 1-8 Typical point defects [123]

Atomic models of (a) pentagon and heptagon pairs (Stone-Wales defect) in a pristine graphene created by C–C bond rotation (the right panel a-4 is a TEM image), (b) single vacancy and its reconstructed structure and (c) reconstructed double vacancy structures.

The strain arising from curvature and defects lowers dislocation threshold, and thereby promote further dislocations nearby and existing defect [125]. Using accelerating voltages of 80–120 kV, which are near or just above the knock-on threshold, we can intentionally introduce defects in nanocarbon materials. Electron beam can be focused onto small areas to cut materials locally. It can also be used to irradiate large areas to induce moderate structural changes [118], and thereby create new materials. For example, fabrication of 2D amorphous carbon (Fig. 1-9(a), [126], [127]), quasi-1D graphene nanoribbons (Fig. 1-9(b), [128]) and ideally 1D carbynes (Fig. 1-9(c), [97], [129]–[132]) from graphene or carbon nanotubes. Not only carbon materials, but also other 2D materials could be thinned by electron irradiation, including transition metal dichalcogenide nanowires [133] or boron nitride (BN) chains [103].

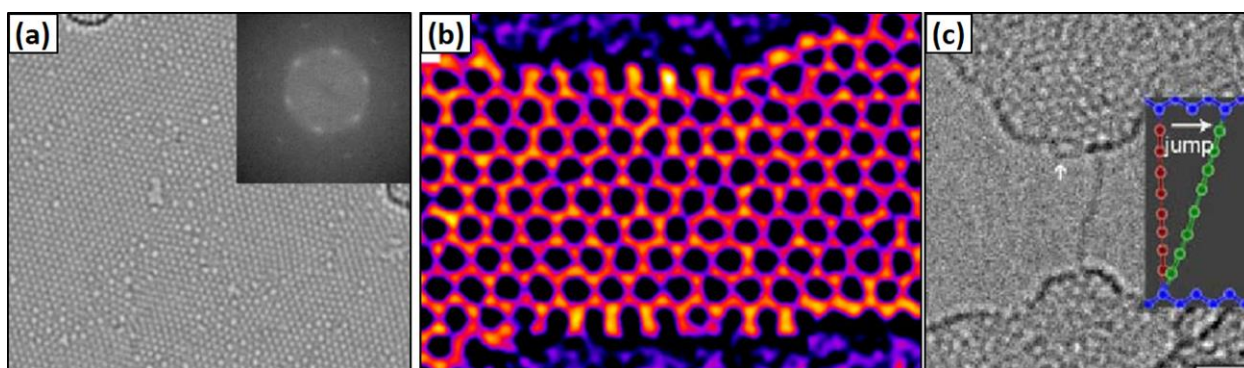


Figure 1-9 Engineering nanocarbon materials by electron irradiation

TEM images of thinned materials by electron beam (a) 2D amorphous graphene [127], (b) graphene nanoribbons (false-color image) [128] and (c) carbon chains (carbyne) [97].

Among these novel low-dimensional materials, carbyne is a fundamental and ideal chain structure that has been an interesting research subject for theoreticians [134], [135]; long before the discovery of graphene or CNT. It is a linear monoatomic chain of sp -hybridized C atoms. We found a new formation method of carbynes on graphene, where substitutional metal atoms served as nucleation sites for carbyne, while graphene acted as a support membrane. This result is described in Chapter 4.

Introduction

Now we discuss mending and growth effects promoted by electron beam irradiation or sample heating. As shown above, a high-energy electron beam can damage graphene, so that we can use it for nanofabrication by means of sample cutting at nearly atomic scale. On the other hand, there are several reports on mending of graphene pores or crystallization of adatoms under the electron beam irradiation. Zan *et al.* reported that graphene can mend small pores under electron irradiation at room temperature at 60 kV in STEM mode (Figure 1-10(a), [136]). Liu, Suenaga and coworkers observed that second-layer of graphene grew at the step-edge of double-layer graphene at 500–650 °C (773–923 K). It is possibly promoted by presence of Si atoms (Fig. 1-10(b), [105]). Westenfelder *et al.* investigated the effect of elevated sample temperature by *in situ* heating TEM experiments up to $T \sim 2000$ K, and found that amorphous hydrocarbon contaminants started crystallizing into graphene at ~ 1000 K (Fig. 1-10 (c), [137]).

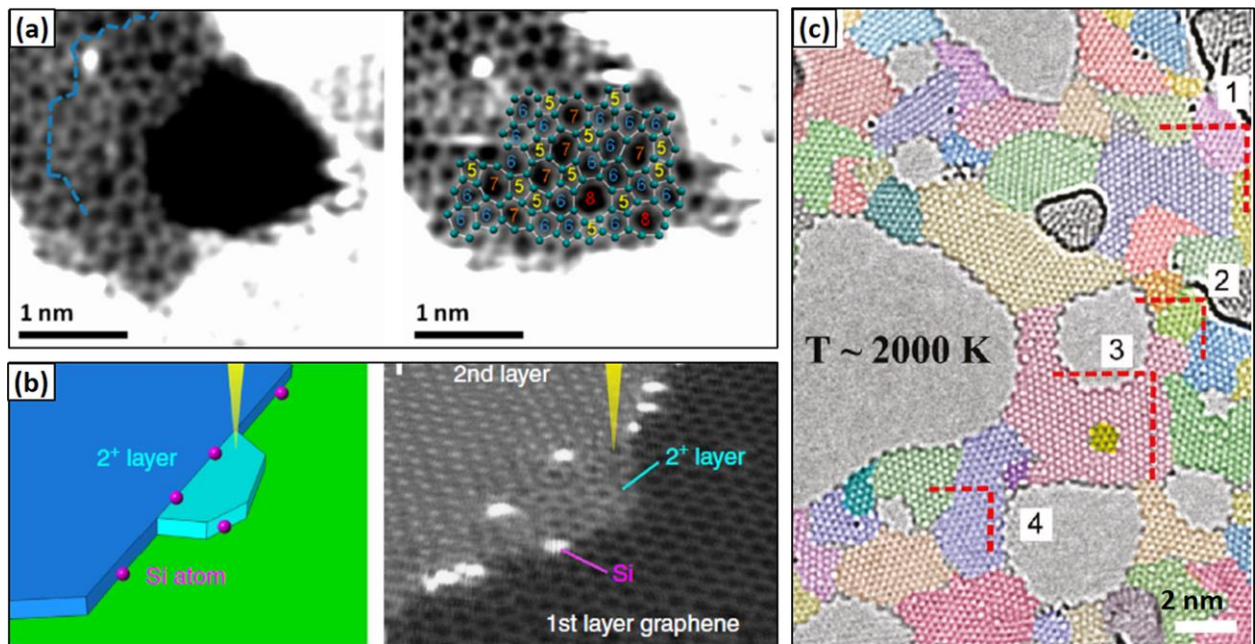


Figure 1-10 Graphene defect mending or growth under electron irradiation

(a) STEM images before and after mending of a pore in graphene [136]. (b) Schematic and STEM image of graphene growth at step-edges [105]. (c) TEM image of crystallized structure originating from hydrocarbon contamination (in this image the signal from underlying graphene was removed) [137].

Chapter 1

These previous reports suggest that the temperature is an important factor in graphene defect mending and reconstruction. However, the catalytic activity of impurity atoms is unclear. For example, reports on the role of Si atoms are inconsistent. As is mentioned above, Liu *et al.* reported that Si atoms may catalyze a growth of second-layer of graphene (Fig. 1-10(b), [105]). On the other hand, Wang *et al.* reported that Si atoms promoted etching of graphene [138], while others reported that Si atoms can stabilize edges of graphene pores [139]–[142]. This inconsistency arises presumably because of the different experimental conditions, such as electron irradiation density, residue of contamination and vacuum conditions; in particular the presence of residual water vapor in the microscope vacuum.

In summary, we described the structure of the basic defects and their reducing effect on the knock-on threshold energy. Using different accelerating voltages and *in situ* annealing, electron beam irradiation can modify graphene structure in two ways: etching or mending. To clarify the effect of impurities (especially metal atoms) on graphene etching and mending, the next subsection summarizes previous reports on metal-graphene interactions.

1-2-2 Interactions between metals and graphene

Compared with the research on graphene itself, experimental investigations of interactions between metal atoms and graphene is still in its infancy. Theoretical studies are ahead of experiment, although they can be controversial due to the lack of experimental verification of the proposed models. At first, we summarize existing studies on metal nanoparticles and graphene, which may be relevant to interaction of metal atoms with graphene.

Pt nanoparticles are known to be a very efficient catalyst in polymer electrolyte fuel cells. Because of large specific surface area and mechanical strength, graphene and CNTs were regarded as a successor of carbon black, which had been extensively utilized as a support material of Pt catalyst nanoparticles. One of the critical problems of applications in catalysis has been its durability. The catalyst efficiency typically degrades during use. Investigations aimed to elucidate the degradation mechanisms concluded that metal nanoparticles, especially Pt, etch carbon support materials at elevated temperature in oxygen or hydrogen gas atmosphere [143], [144]. This etching is one of the reasons for degradation in nanocatalysts: metal nanoparticles etch and destroy graphene resulting in aggregation of nanoparticles, and thereby decrease surface area of catalysts and consequent decrease of their efficiency.

The carbon etching, on the other hand, offers a promising method of fabricating graphene nanoribbons, as metal nanoparticles can etch graphene along a specific crystallographic direction [37], [145]–[148]. Porous graphene, prepared by metal-catalyzed etching, has attracted research interest as it may enhance the charge density in batteries [149]. Graphene perforation at nanoscale can also increase optical signals for DNA sequencing [47]. As such, metal-graphene interactions results are inextricably associated with each other. If it is beneficial for a particular application, it is likely to be detrimental for other applications. In both cases, it is important to understand which metals and under what conditions affect graphene structure in a particular way.

An interesting question is whether single metal atoms can catalyze to modify graphene. Recently, researchers observed metal atoms in graphene by aberration-corrected (S)TEM, such as Fe atoms [150], [151] and single atoms of Pt, Co and In [152] doped into graphene vacancies. Observations of Au [153] and Fe [154] atoms diffusing along graphene edge were also reported. Under electron beam irradiation, Au and Fe atoms at graphene edges were reported to remove or add a few C atoms around their location, but the edge structure did not change significantly. Ramasse *et al.*

[155] suggested that many metal atoms (Cr, Ti, Pd, Ni or Al), except for Au, promoted etching of graphene even at room temperature (Figure 1-11). In their study, neither gas environment nor high temperatures were used, although the residual oxygen and water vapor in the microscope vacuum might assist this etching under electron beam irradiation. Based on these studies, it appears that not only nanoparticles, but also individual atoms possibly etch graphene.

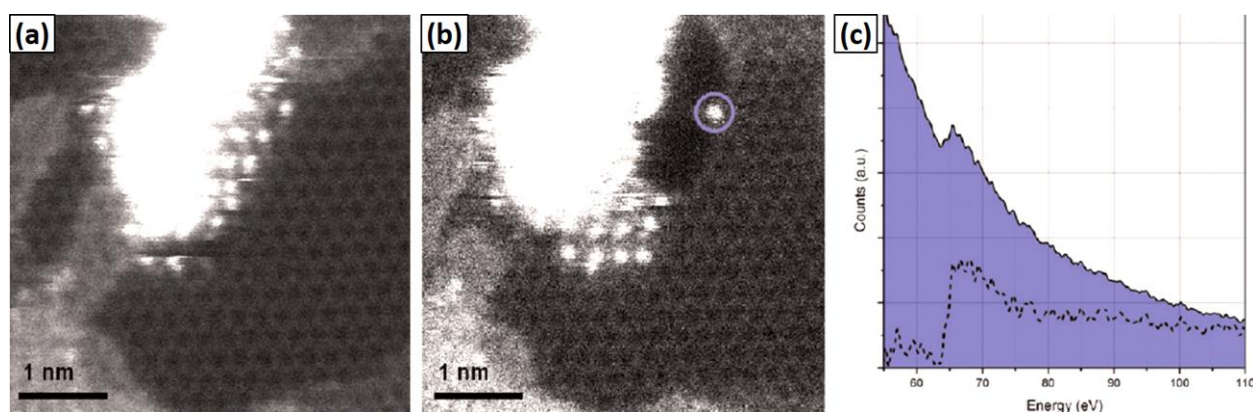


Figure 1-11 Metal mediated graphene etching [155]

ADF-STEM images of (a) Ni cluster located at the edge of the hydrocarbon contaminants and (b) generation of pores by Ni after few scans. (c) EEL spectrum from a bright atom circled in image (b).

However, the catalytic activity of single metal atoms is still unclear. Metal atoms hardly adsorb on clean graphene surface, and the etching phenomena shown in Fig. 1-11 could be caused by oxygen or hydrocarbon contamination or intense electron beam irradiation. As mentioned above, only a few experimental reports have been published so far discussing activity of metal on graphene. Therefore, it is essential to observe interaction of graphene with different chemical elements to clarify the intrinsic effects of metal atoms on graphene.

1-2-3 Originality of the thesis

Although there has been a strong interest in controlling defects in graphene, to the best of our knowledge, there are no reports on the direct observation of single-atom metal catalysis of mending or reconstruction of graphene structure. As described above, most metal atoms either etch graphene or weakly interact with it. Many factors can contribute to etching or mending of graphene. Furthermore, we suspect that surface contamination hinders the intrinsic effects of metal atoms on graphene. Many earlier studies reported unintentional impurity atoms on graphene [74], [105], [138]–[142], [150], [154], [156], [157]. In most cases, they are Si and Fe, as these are the most common impurities incorporated in graphene during the sample preparation.

We spent much effort to prepare clean graphene samples, as discussed in section 2-3. Fundamentally, it is impossible to remove all the impurities at atomic level. However, we were successful in removing metal impurities other than target atoms and minimized hydrocarbon contamination by *in situ* heating inside a TEM column at $\sim 10^{-5}$ Pa. As a result, we demonstrated that single metal atoms could catalyze modification of graphene structure under electron irradiation.

In this thesis, we investigate noble metals, Cu, Pt and Au, because they are promising elements for single-atom catalysis. Cu is known to be the best performing catalyst for graphene growth; therefore, it is expected to catalyze the growth or modification of other carbon nanostructures. Indeed, we have found that substitutional Cu atoms promote rotation of C–C bonds near Cu atoms, and thereby contribute to reconstruction of graphene grain structure. Relations between energy barrier of each transformation and electron irradiation effects are analyzed and discussed in Chapter 3. Furthermore, we found that individual Pt and Cu atoms promote opposite effects on graphene edges: etching and mending, respectively, under electron irradiation, as discussed in Chapter 4.

During the observation of reconstruction phenomena, we discovered other novel low-dimensional structures formed on graphene: “metal-terminated carbynes”, i.e., monoatomic linear carbon chains described in Chapter 5, and “one-atom-thick 2D copper oxide with square lattice” described in Chapter 6. It is difficult to produce and observe such small and thin materials by techniques other than *in situ* TEM. Furthermore, *in situ* TEM is required for understanding the structure and formation mechanisms of the novel nanomaterials.

Chapter 1

At present, our findings are not directly linked to practical applications. This is because our experimental conditions are optimized for atomic-resolution imaging, including high vacuum, *in situ* heating and electron beam irradiation; they differ from device fabrication conditions. Nevertheless, our results provide fundamental insights into the structure of metal atoms and graphene. Our results also demonstrate a promising method of controlling atomic-scale structures both for fundamental research and for commercial applications.

1-3 Thesis outline

This thesis consists of six chapters. In Chapter 1 background, important basics, objective and previous studies on metals and graphene are introduced. Chapter 2 contains the principles of technical methods: TEM imaging and analysis, electron beam irradiation effects, and sample preparation.

Chapters 3 to 6 contains results and discussions of individual experiments. In summary, we report two major interesting phenomena: graphene reconstruction promoted by metal atoms chemisorbed in the graphene lattice (Chapters 3 and 4), and self-assembly of novel structures from physisorbed and diffusing atoms on graphene surface (Chapters 5 and 6). Figure 1-12 shows schematics of these electron beam assisted phenomena.

Then Conclusions and suggestions for future research directions are described, followed by List of Figures, Tables, Abbreviations and Publications, References and Acknowledgements.

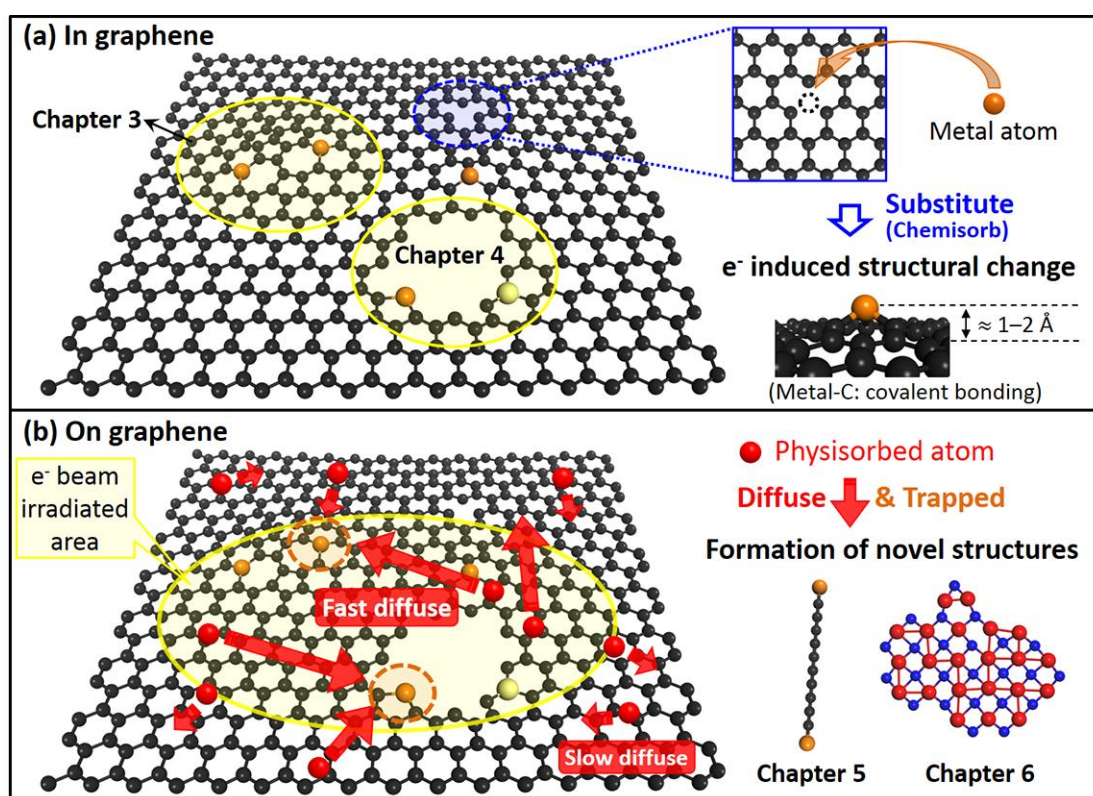


Figure 1-12 Schematics of metal atoms in/on graphene

Metal atoms (a) at graphene pores and lattice sites and (b) diffusing and forming novel structures on the graphene surface.

Chapter 2

Basic principles and experimental methods

A transmission electron microscope offers several imaging modes and chemical analysis methods. To obtain atomic-resolution images and chemical information, it is necessary to understand the basics of each mode and prepare appropriate samples. Basics and specific examples of each characterization method are provided in the first section (2-1) of this chapter. The second section (2-2) elaborates the electron beam irradiation effects, which are mostly related to the results of Chapters 3 and 4. Sample preparation methods are detailed in the third section (2-3).

2-1 Electron microscopy

The first subsection describes brief history about aberration corrector and experimental observation conditions. In the second subsection, we discuss the difference between three imaging modes used in this thesis. The last subsection explains a chemical analysis mode of EELS.

2-1-1 Aberration corrector and our equipment component

There are three steps in improving the spatial resolution. As shown in Figure 2-1(a), the long wavelength of light (a few hundred nm) has limited the resolution of optical microscopy, while the electron wavelength could be reduced by increasing the accelerating voltage, enabling nanoscale imaging of materials. Ruska constructed the first prototype electron microscope in the early 1930s and overcame the resolution of optical microscopy. He was awarded a Nobel Prize for this work in 1986. The resolution of electron microscopy had steadily increased over the next 50 years, and then saturated at $\sim 2 \text{ \AA}$ due to limits arising from lens aberrations. Researchers tried to overcome this problem by applying higher accelerating voltages and thereby shortening the wavelength, but this brute-force method had limited the range of observable materials because of damage by high-energy electrons. Since the wavelength of accelerated electron is about two orders of magnitude smaller than atoms (e.g. $\lambda=4.18, 2.51, \text{ and } 0.87 \text{ pm}$ for accelerating voltages of 80, 200, and 1000 kV, respectively), the resolution of electron microscopy was not limited by wavelength but by spherical aberrations.

Basic principles and experimental methods

Figure 2-1(b) shows a schematic of positive spherical lens aberration. In contrast to an optical lens, an electron lens always acts as a converging lens. Because of the lack of concave lens effects, aberrations of the objective lens are always positive and cannot be compensated by a combination of concave and converging lens as in light optics. The presence of lens aberrations leads to delocalized contrast, seen as blurred images. After the electron microscope was developed in 1930s, there were many attempts to correct aberrations. Haider and Rose *et al.* succeeded to develop a spherical aberration corrector for TEM in the late 1990s [78], [158]. Shortly after that, Krivanek *et al.* developed an aberration corrector for STEM [159]. These correctors are commercialized by CEOS in the US and by Nion in Germany.

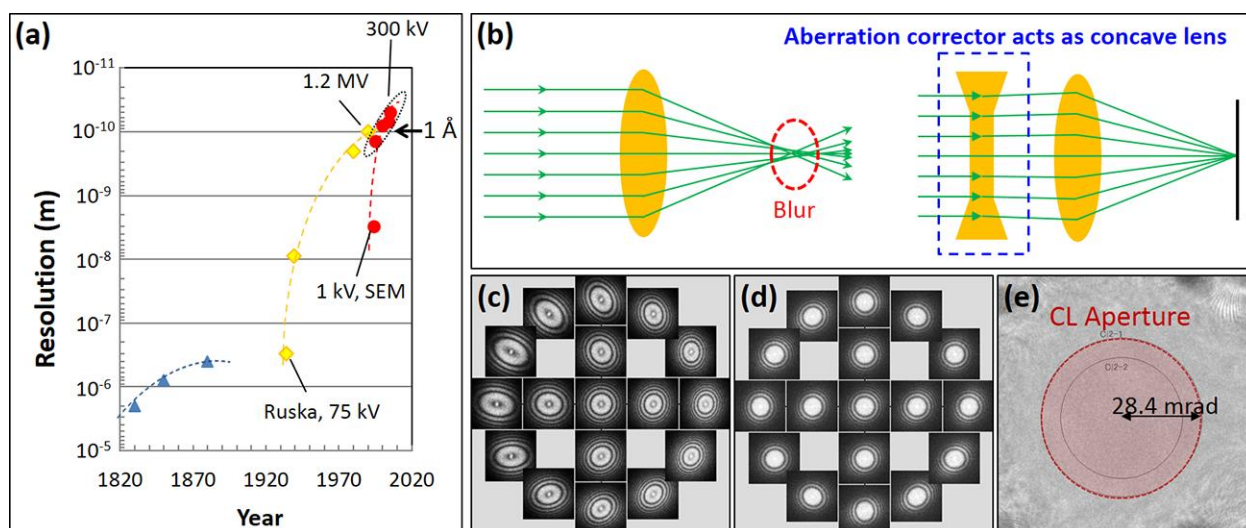


Figure 2-1 Spatial resolution and aberration corrector

(a) History of resolution improvement in microscopy. Blue triangles present optical microscopy. Yellow and red symbols correspond to the resolution of electron microscopy (including SEM, TEM and STEM) without and with aberration correctors, respectively (redrawn from [160]). (b) Schematics of spherical aberration. Panels (c) and (d) show diffractograms before and after application of a hexapole-based aberration corrector in TEM mode. (e) STEM Ronchigram of Au particles on an amorphous substrate taken after the alignment. Red circle corresponds to the beam area selected by the condenser lens aperture that we used for the reported experiments.

We used JEM-ARM 200F transmission electron microscopes from JEOL equipped with CEOS hexapole-based aberration correctors in both the image-forming lens and probe-forming lens. The

Chapter 2

microscopes were operated at an accelerating voltage of 80 kV to reduce knock-on damage to graphene samples. Figures 2-1(c) and (d) show screen images of the imaging aberration corrector. In TEM mode, we corrected aberration almost every time when we changed the sample or a beam parameter until achieving the following values: two-fold astigmatism (A1) less than 1 nm, three-fold astigmatism (A2) and coma (B2) less than 50 nm, third-order spherical aberration (C3) -1 to -5 μm , and four-fold astigmatism (A3) and star aberration (S3) less than 1 μm . We set C3 to a negative value because TEM images were taken under overfocus conditions, as described in the next subsection.

The Ronchigram in Fig. 2-1(e) shows a flat-phase region corresponding to the aberration-free beam conditions. We used the condenser aperture with a convergence semi-angle of 28.5 mrad to cut off the electrons passing outside the flat region. The angular range of electrons collected by the ADF detector was about 46–161 mrad. These values were measured using the diffraction signals of Si (standard sample) at the detector plane (see Appendix Fig. A-11).

We used two aberration-corrected microscopes with different electron guns: a Schottky gun and a cold field emission gun (FEG). The Schottky gun is a field-assisted thermal gun, resulting in a larger chromatic aberration and hence a lower resolution than the cold FEG. The cold FEG emits electrons from W tip by quantum mechanical tunneling, leading to narrow energy distribution and a small chromatic aberration. Most experiments were therefore performed with the cold FEG instrument, except for the observation of Pt-terminated carbyne described in Chapter 4. *In situ* heating holder (AduroTM, Protochips) was used for heating experiments reported in Chapters 3–5, while a conventional double-tilt holder was used for observation of 2D copper oxide at room temperature (Chapter 6).

2-1-2 Imaging mode (TEM, DF-TEM, STEM)

We used three imaging modes: conventional bright-field TEM (BF-TEM), dark-field TEM (DF-TEM) and annular dark field STEM (ADF-STEM). This subsection describes the difference between TEM and STEM modes for atomic-resolution imaging of metal-doped graphene, followed by large area characterization using DF-TEM.

Figure 2-2 shows illumination systems of TEM and STEM modes. In the conventional TEM mode, an almost parallel electron beam illuminates a sample, and images are simultaneously collected for all pixels across the entire field of view. On the other hand, STEM uses a convergent electron beam. A small probe ($\sim 0.8 \text{ \AA}$ in our microscope) is scanned across a sample and data are collected in a serial manner: pixel by pixel.

TEM provides phase-contrast imaging and is highly sensitive to the defocus condition. We usually take atomic-resolution TEM images under overfocus conditions (defocus value: approximately 3–4 nm), so that atoms appear bright for single layer graphene with substitutional metal atoms (simulated images are shown in Figs. 2-3 (b)–(d)). Meanwhile, at underfocus (Scherzer focus) the contrast is reversed (Fig. 2-3(a)). We tried both defocus conditions and selected overfocus condition, because the dynamics of metal atoms was easier to follow.

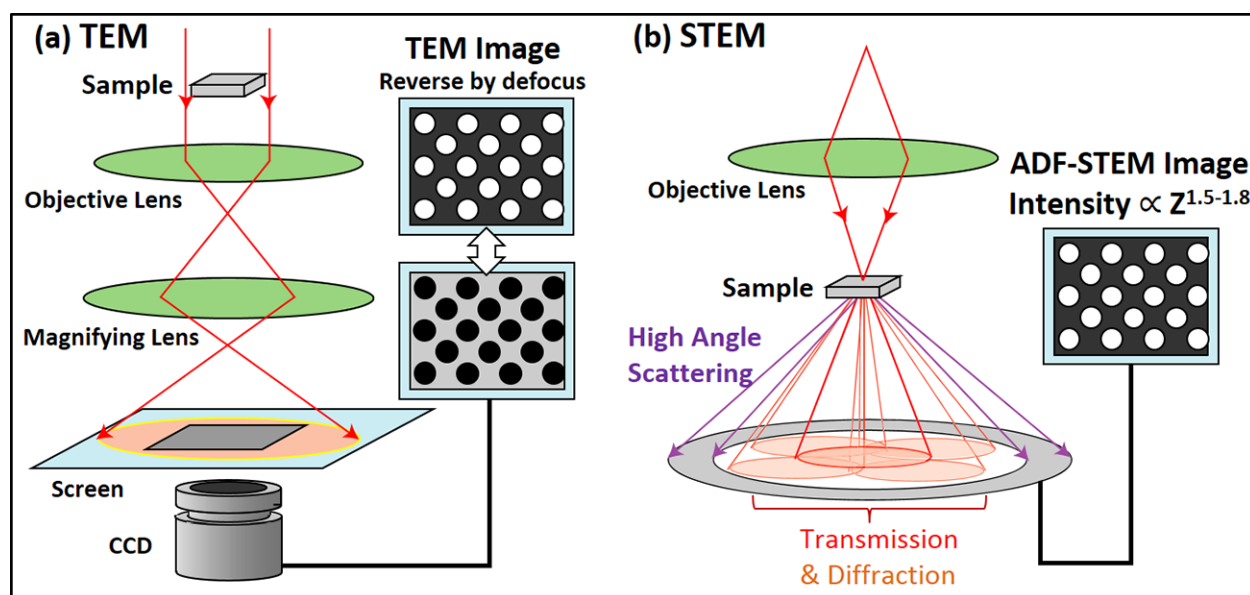


Figure 2-2 Illumination systems of TEM and STEM

Researchers often perform TEM image simulations to evaluate the experimental image contrast. We simulated TEM images by multislice method using xHREMTM software (HREM Research

Inc.) under the following conditions: defocus spread 4 nm, beam convergence 0.3 mrad, third-order spherical aberration coefficient $-1 \mu\text{m}$, fifth-order spherical aberration coefficient $1 \mu\text{m}$, and defocus value 3 nm. Figures 2-3(b)–(d) show simulated TEM images of dopant atoms substituted in graphene at overfocus and the corresponding line profiles, which are normalized by C signals. Multislice simulation for the present overfocus conditions yielded Cu/C, Si/C, and Pt/C signal ratios of 1.92, 1.62, and 3.15, respectively. In TEM images, Si should be a little darker than Cu, but the difference is hard to detect.

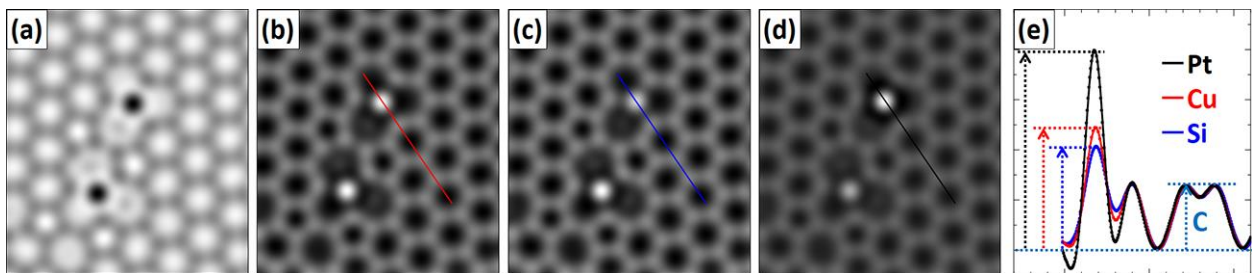


Figure 2-3 Simulated TEM images

Simulated TEM images of two Cu atoms substituted in graphene at (a) underfocus and (b) overfocus. (c), (d) Simulated TEM images of Si and Pt, respectively. The lower-left bright atoms are Cu, and only the upper-right bright atoms are changed from (b). (e) Signal intensities along lines indicated in panels (b)–(d). The line profiles are normalized by C signals.

In STEM mode, the ADF signal difference of each atom is much clearer and is suitable for the chemical identification. The intensity of ADF-STEM images increases with atomic number as Z^x , where x is expected to be in the range 1.5–1.8. Krivanek *et al.* reported that it is possible to identify the chemical type of atoms by combining atomic-resolution ADF-STEM imaging with a quantitative statistical analysis [161]. They used a sample consisting of B, C, N and O ($Z=5, 6, 7$, and 8, respectively), and every atom in the analyzed area could be assigned to a particular species with 99% confidence. Other researchers also identified nitrogen dopant atoms substituted in graphene by ADF-STEM or STEM-EELS imaging [104], [162], [163].

The exponent x depends on the signal collection geometry and studied elements. In our experimental STEM images, as shown in Figs. 2-4(a) and (b), the Cu/C signal ratio was about 10–12; therefore we assumed that the image intensity was proportional to $\sim Z^{1.5}$ (Fig. 2-4 (h)). Using the xHREMTM software mentioned above, we performed image simulation under the following conditions: the aperture radius (convergence semi-angle) 28.5 mrad, third- and fifth-order spherical aberration coefficients 5 μm , ADF detector angle 46–161 mrad, and probe size 0.8 Å. Simulations included thermal diffuse scattering absorption with the Debye-Waller factors of each element taken from the literature [164]–[166].

Figures. 2-4(d) and (e) show simulated ADF-STEM images of a 2D copper oxide cluster on graphene, where Figs. 2-4(f) and (g) are corresponding line profiles. When we put additional Cu atoms on top of Cu atoms (Fig. 2-4(e)), the intensity doubled and was clearly different from that of a Cu monolayer. However, atomic positions of light elements (e.g. C and oxygen) are unclear in the presence of heavy metal atoms. The variation of Cu intensity (shown in Figs. 2-4(c) and (f)) arises from either underlying C atoms in graphene or adatoms (C or O) on Cu monolayer. In principle, it should be possible to record both metal atoms and C atoms in graphene in one image, but this proved difficult in our experiment: metal atoms appeared more than 10 times brighter than C atoms, which hindered the imaging of C atoms located next to them.

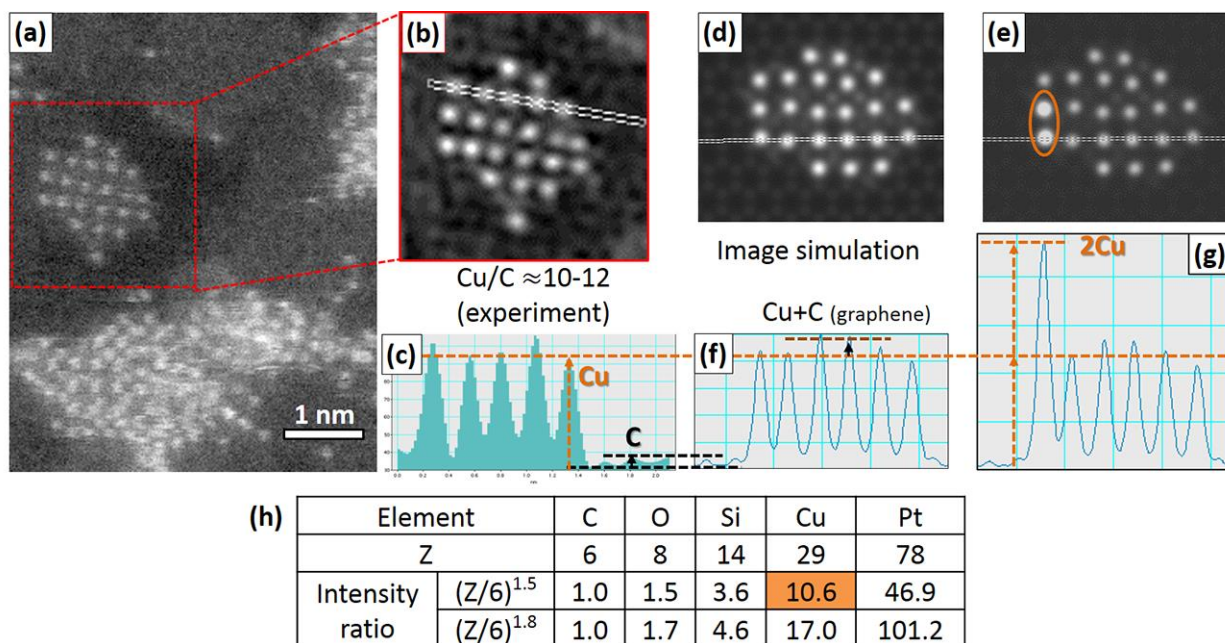


Figure 2-4 Intensity in ADF-STEM images

(a) Experimental ADF-STEM image of 2D copper oxide cluster on graphene. (b) Low-pass filtered image of (a). (c) Line profile taken through the white line marked in (b). (d), (e) Simulated ADF-STEM images of 2D copper oxide clusters. In panel (e), we added two Cu atoms, marked by orange ellipse, on the Cu atoms in the first layer. (f), (g) Line profiles taken along the white lines marked in (d) and (e), respectively. A table in (h) shows C-based intensity of each element.

In short, ADF-STEM mode is suitable for identification of impurity atoms, although it is difficult to visualize both heavy and light atoms in one image because of their large intensity difference. On the other hand, TEM mode is suitable for observing metal atoms substituted in graphene lattice, but is hard to distinguish chemical element of atoms, even those with significantly different atomic numbers like Si and Cu. We need to select appropriate imaging mode according to the chemical composition of the sample and the purpose of the experiment. We usually performed EELS analysis prior to TEM or STEM imaging to distinguish deposited target metals from unwanted impurity atoms such as Si.

Now we discuss the measurement of the number of graphene layers. Atomic-resolution imaging is a powerful technique, but it is not appropriate for large-area characterization. Meyer *et al.* reported that the intensity of diffraction spots is different for single- and double-layer graphene (Figure 2-5, [167]). Hence diffraction analysis is commonly used to check the number of graphene layers. However, graphene grown by chemical vapor deposition is a polycrystalline membrane that often contains many misoriented small grains or misoriented stacked layers. In such case, diffraction pattern combined with DF-TEM imaging is an easy way to examine grain boundaries, number of layers and stacking orientations of graphene over a large area [168]–[171].

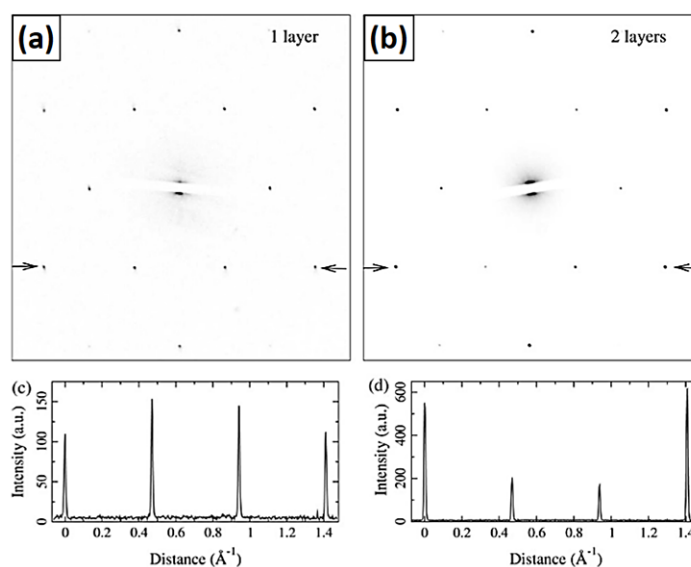


Figure 2-5 Diffraction pattern of graphene [167]

Diffraction pattern of (a) single-layer graphene and (b) double-layer graphene with AB Bernal stacking. The inner hexagon of diffraction spot corresponds to the $\{10\bar{1}0\}$ planes of graphene (lattice spacing $d = 2.13 \text{ \AA}$), while the outer hexagon corresponds to the $\{11\bar{2}0\}$ planes ($d = 1.23 \text{ \AA}$). In the case with double-layer graphene shown in (b), the intensity of the outer spots is clearly higher than that of inner spots.

DF-TEM images are taken by inserting an objective aperture at the back focal plane to collect electrons only diffracted through a small range of angles (Fig. 2-6 (a)). Electron diffraction patterns of single-crystal graphene show a six-fold symmetry, where the appearance of different families of six-fold spots indicates the presence of multiple grains with different orientations. The diffraction pattern shown in Fig. 2-6(b) has 6 families of spots, and Fig. 2-6(c) shows corresponding grain structures. In this case, the grains were very small and miss-oriented.

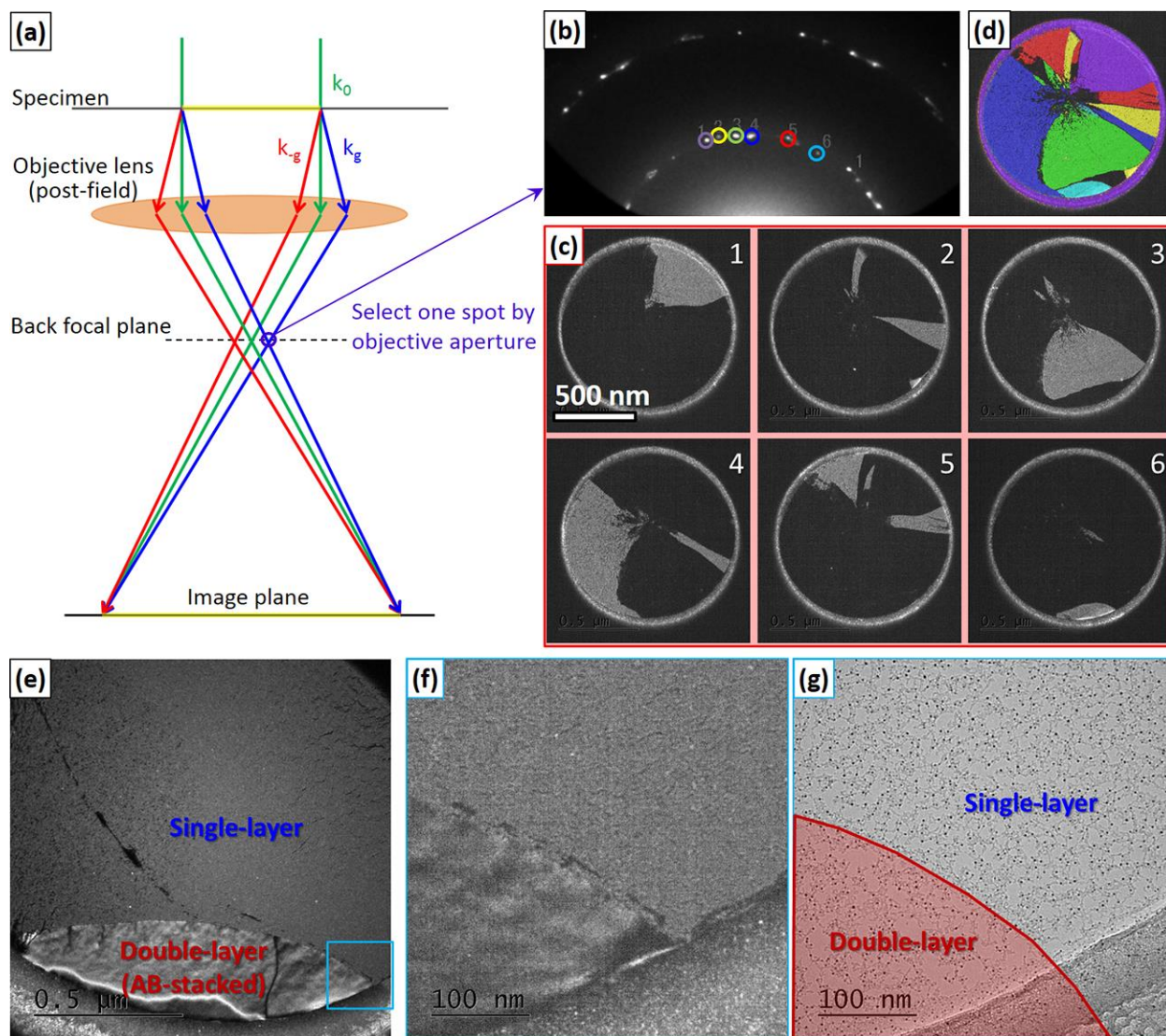


Figure 2-6 Dark-field TEM

(a) Schematic of TEM imaging optics. The projection system of the microscope is omitted for simplicity. (b) Diffraction pattern indicating polycrystalline graphene. (c) DF-TEM images taken from each spot shown in (b). (d) Colored and overlaid image of (c), where the six colors correspond to the diffraction spot in (b). (e) DF-TEM image indicating the boundary between single- and double-layer graphene regions. Panels (f) and (g) are DF- and bright-field (BF) TEM images taken from the light blue area in (e)

Figures 2-6 (e–g) show the boundary between single- and double-layer graphene regions. AB-stacked double-layer region appears bright [171] in DF-TEM image with dark lines, indicating the presence of stacking domain boundary. Lin *et al.* [170] reported that AB/AC stacking domain boundaries, mostly in the form of ripples, can be visualized by tilting the sample in DF-TEM.

Using this technique, we have evaluated the quality of graphene samples provided by our collaborators [172], [173]. We usually performed DF-TEM analysis prior to atomic-resolution imaging to select an appropriate area of the CVD graphene sample.

In summary, we explained three imaging modes that we used: conventional BF-TEM, DF-TEM and ADF-STEM. DF-TEM was utilized for a preliminary, large-area analysis of graphene samples, while BF-TEM and ADF-STEM modes were employed for local atomic-resolution imaging. Figure 2-7 shows a specific example of DF-TEM analysis and atomic-resolution TEM and ADF-STEM images of graphene. The contrast of TEM and ADF-STEM images differs when the sample contains heavy metal atoms. In general, STEM is suitable for chemical analysis; however, we strived to observe dynamics of both light C and heavy metal atoms. Although TEM imaging often requires chemical analysis prior to the atomic-resolution imaging, it is appropriate for our purpose in terms of image contrast and time resolution. Therefore, most experiments in this thesis were conducted using TEM mode, as described in Chapters 3–5. Then we turned attention to nanoscale materials on graphene, and observed 2D copper oxide by STEM-EELS, as described in Chapter 6.

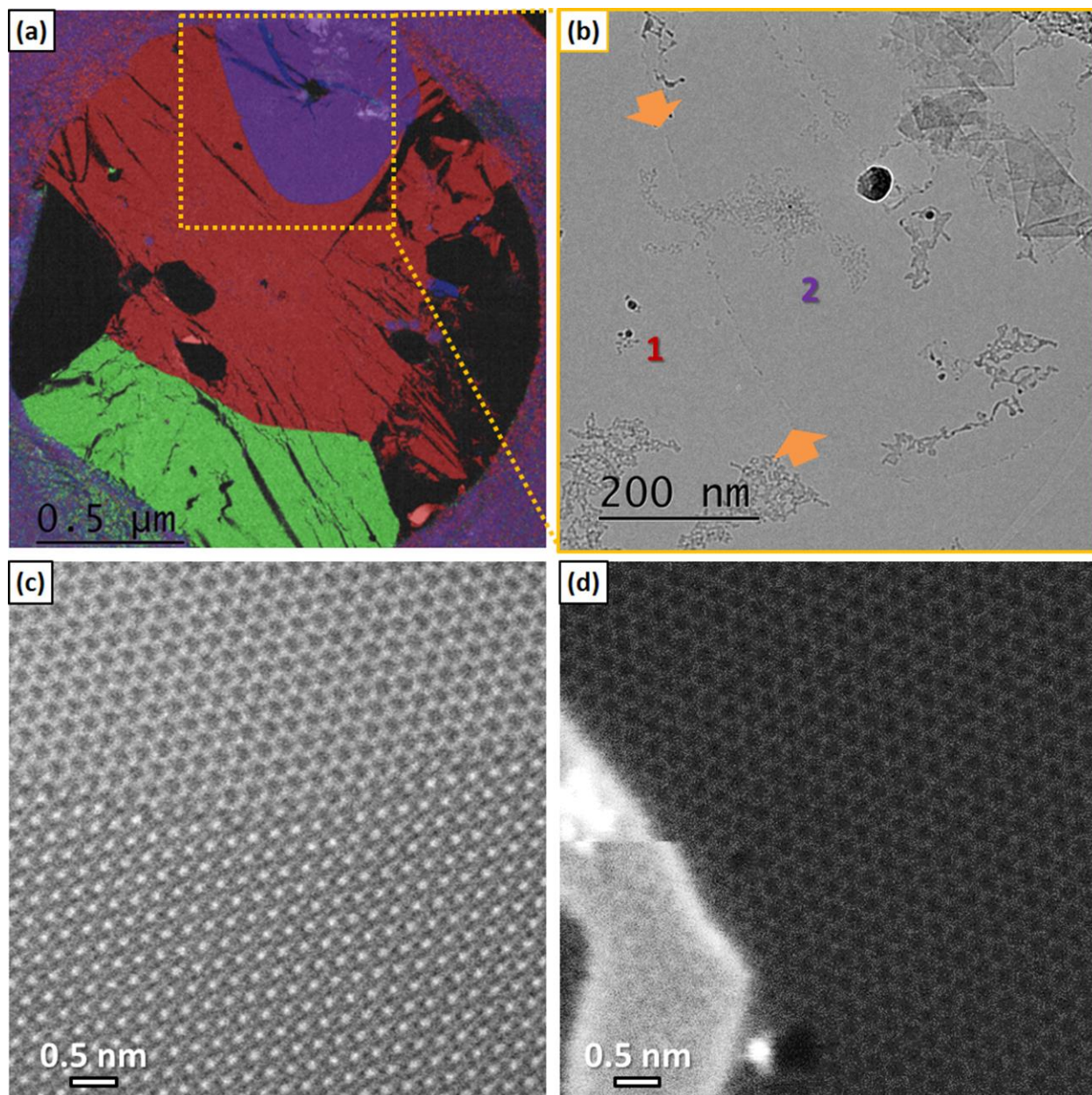


Figure 2-7 DF-TEM, TEM and ADF-STEM images of graphene

(a) False-color DF-TEM image, where the violet area corresponds to double-layer graphene with misoriented stacking, red and green areas correspond to single-layer graphene with different orientations. (b) TEM image corresponding to (a). Impurity nanoparticle in (b) was identified as SiO_2 by EELS. (c) Atomic-resolution TEM image taken at a step between a single-layer (top) and a double-layer graphene (bottom, AB-stacking area). (d) Atomic-resolution ADF-STEM image of single-layer graphene with small defects, contamination and impurity atom. It took 1 s to obtain TEM image (c), while STEM image (d) required 1min for a satisfactory signal-to-noise ratio.

2-1-3 Electron energy-loss spectroscopy (EELS)

This subsection explains principles of EELS on specific examples of carbon and copper. The explanation is based on the literature (Egerton [174]).

Incident fast electrons interact with atomic electrons and cause excitation of inner or outer-shell electrons. These interactions are referred to as inelastic scattering, as significant amount of energy is usually transferred from the incident electron to the atomic electrons. The incident electrons lose a characteristic amount of energy determined by the chemical element of atom and the energy level of atomic electrons. An electron spectrometer separates the transmitted electrons according to their kinetic energy and produces an electron energy-loss spectrum, showing scattered intensity as a function of a decrease in kinetic energy. Using a transmission electron microscope, we can simultaneously record this energy loss (over a range of ~2000 eV) and a high-resolution image.

Inelastic scattering from outer-shell electrons appears as a peak in the range of 4–40 eV, while that from inner-shell electrons appears as edges rather than peaks, because the inner-shell scattering probability rises rapidly and then falls slowly with increasing energy loss. The sharp rise occurs at the ionization threshold, and its energy-loss value corresponds to the binding energy of the atomic shell. Both the low-loss peaks and the ionization edges possess a fine structure that reflects the crystallographic or energy-band structure of the specimen. Therefore, analyzing such fine structure of energy-loss spectrum provides us information about not only chemical composition but also chemical bonding in a specimen. For example, we can distinguish the carbon allotropes (such as diamond, graphite and amorphous) from the shape and position of low-loss peak and K-ionization edges in energy-loss spectra. Furthermore, energy-loss near-edge fine structure (ELNES) of C atoms at graphene edge can be distinguished from that at bulk graphene (shown in Figure 1-5).

Figure 2-8 shows core-loss spectra of the carbon K edge and copper L edge. Carbon K edge of graphene (Fig. 2-8(b)) shows sharper π and σ peaks than that of amorphous carbon film (Fig. 2-8(b)). This graphene K-edge spectrum indicated the typical features of sp^2 -coordinated carbon. Sharp copper L threshold peaks (Fig. 2-8(d)) are so-called “white lines”, which indicate a partial emptying of the Cu 3d band caused by chemical bonding with oxygen [175], [176]. If Cu particles do not bond with O atoms, they exhibit no sharp Cu threshold peaks (Fig. 2-8(c)). Further examples are shown in Appendix Figs. A-2 to A-5.

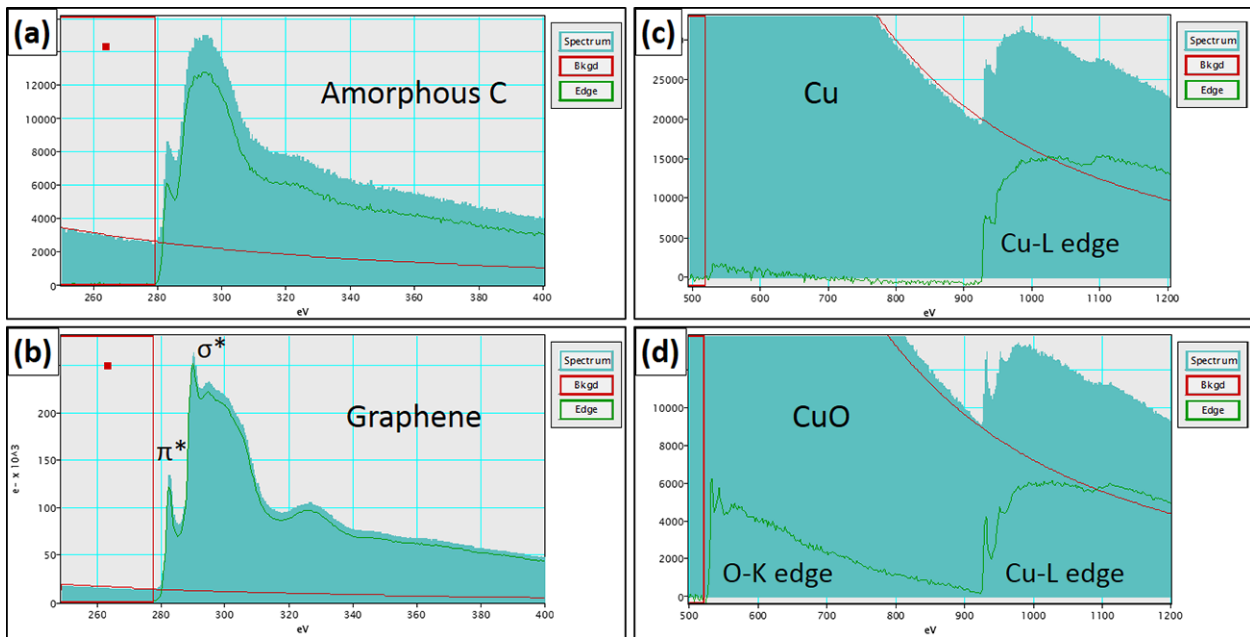


Figure 2-8 EEL spectra of C and Cu

EEL spectra of (a) amorphous carbon, (b) single-layer graphene, (c) bulk Cu and (d) bulk CuO. Green lines indicate background subtracted spectra. (a), (c) and (d) are reference spectra from EELS atlas [177], while (b) is obtained at a clean graphene area by TEM-EELS.

2-2 Principles of electron irradiation effects

Electron-induced transformations are the most important part of this thesis (presented in Chapter 3). Here we elaborate the electron irradiation effects that are relevant to this thesis. The related equations are taken from literature (Egerton [174], Reimer and Kohl [178]).

2-2-1 Elastic and inelastic scattering

When electrons enter a specimen, they interact with atoms and are scattered by Coulomb forces. The scattering is generally divided into two categories: elastic and inelastic. Elastic scattering is caused by Coulomb attraction with the atomic nuclei, while inelastic scattering results from Coulomb repulsion with the atomic electrons. As a result, elastic scattering causes energy transfer to atomic nuclei from high-energy incident electrons, while inelastic scattering induces excitation of atomic electrons as described in the previous section.

Here we mainly describe elastic scattering, as inelastic scattering cannot cause movement of C atoms in graphene due to the following reasons [179]:

- 1) Excitation or ionization of atomic electrons is quickly quenched and dissipated throughout the specimen due to the high density of delocalized electrons in metals and graphene.
- 2) Plasmon has an energy of 5–30 eV; however, it is a collective excitation phenomenon, and the excess energy is shared among many atoms.
- 3) De-excitation of electrons often results in thermal energy increase; however, graphene has a high thermal conductivity, and hence the temperature change is only ~5 K.

The word “elastic” usually implies that the energy exchange is negligible, but when a high-energy electron collides with and is scattered by an atomic nucleus of a specimen at a high angle, the scattering atom receives a few electron volts from the incident fast electron. It is a tiny fraction of energy for the incident electron, yet it is significant for the atoms, especially if their atomic mass number is small.

2-2-2 Energy transfer and binding energy of metal-carbon bond

Before and after the collision between the incident electron and atomic nucleus, the total kinetic energy and momentum of the electron and nucleus are conserved as shown in Figure 2-9.

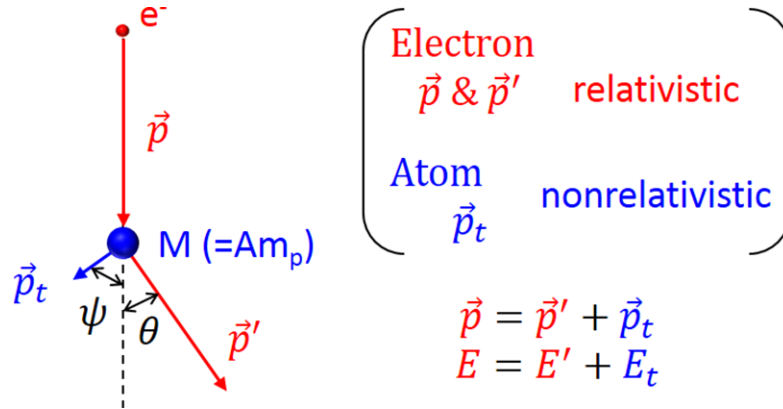


Figure 2-9 Conservation of energy and momentum during elastic scattering

The conservation of momentum gives the following equations:

$$p = p' \cos \theta + p_t \cos \psi$$

$$0 = p' \sin \theta - p_t \sin \psi$$

where suffix t means transferred energy/momentum to atomic nucleus, and θ and ψ are scattering angles of incident electron and atomic nucleus, respectively. Relativistic momentum has to be used for a fast incident electron, whereas nonrelativistic momentum can be used for a slow atomic nucleus. They are given by,

$$p = \frac{1}{c} \sqrt{2EE_0 + E^2}, \quad p' = \frac{1}{c} \sqrt{2E'E_0 + E'^2}$$

$$p_t = \sqrt{2ME_t}$$

where c is velocity of light (3.00×10^8 m/s), E is incident electron energy (in MeV), E_0 is rest energy of electron (0.511 MeV) and $M = Am_p$ is rest mass of the atomic nucleus (A is atomic mass number, m_p : atomic mass unit 1.66×10^{-24} g). We can use the approximation formula $E - E_t \approx E$, because the energy transfer E_t is sufficiently small compared with the incident electron energy E . Solving the above equations, we obtain

$$E_t = \frac{2E(E + 2E_0)}{Mc^2} \sin^2 \frac{\theta}{2} = \frac{E(E + 1.02)}{466A} \sin^2 \frac{\theta}{2}$$

with E_t , E , and E_0 expressed in MeV. As described in section 1-1-2, the energy transfer E_t is proportional to the incident electron energy E and is inversely proportional to the atomic mass number A ; therefore light elements, such as C atoms ($A=12$), are more susceptible to high-energy electron irradiation and could be knocked out from the graphene lattice. Table 2-1 shows typical values of E_t . We used $E = 80$ keV and obtained the maximum values of energy transfer E_{max} for all considered elements (a head-on collision $\theta = 180^\circ$). While the 200 keV electrons easily remove C atoms from the graphene lattice, the 80 keV electrons do not displace C or substitutional impurity atoms in graphene, because the maximum energy transfer E_{max} at 80 keV is smaller than the binding energies to C. Figure 2-10 shows binding energies between metal atoms and graphene.

Table 2-1 Energy transfer E_t

E		80 keV				200 keV			
element		C	Cu	Pt	Au	C	Cu	Pt	Au
A		12.0	63.5	195.1	197.0	12.0	63.5	195.1	197.0
θ	10°	0.12	0.02	0.01	0.01	0.33	0.06	0.02	0.02
	90°	7.87	1.49	0.48	0.48	21.83	4.12	1.34	1.33
	180°	15.75	2.97	0.97	0.96	43.66	8.24	2.69	2.66

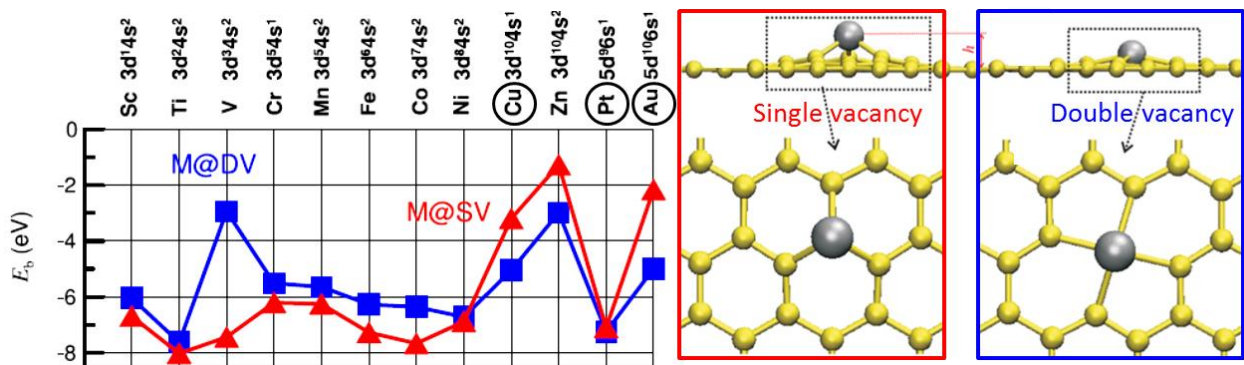


Figure 2-10 Binding energies of substitutional metal atoms in graphene [113]

Binding energies E_b of the graphene sheet with transition metal atoms adsorbed on single and double vacancies (red and blue curves, respectively).

Krashennnikov *et al.* reported that all the considered metal atoms (shown in Fig. 2-10) form covalent bonds with the neighboring C atoms in a graphene vacancy [113]. Since Cu, Zn and Au have filled d shells, their binding energies to C are smaller than those of other transition metal

atoms. Both Pt and Au atoms have a large atomic mass number A and receive a small energy E_t from electron irradiation; however, the difference in their binding energies to C may result in different behaviors in graphene. One can expect that substitutional Pt atoms are less mobile than Au atoms. A Cu atom receives larger energy from electron irradiation compared with Pt and Au atoms due to its smaller atomic mass number, while the Cu-C binding energy is intermediate between Pt-C and Au-C. Based on our results, we propose that atomic mass number and binding energy of metal-C bonds determine whether metal atoms can promote structural changes in graphene under electron irradiation. Chapter 3 discusses substitutional Cu atoms in graphene, while Chapters 4 and 5 describe different behaviors of Cu and Pt atoms interacting with graphene.

2-2-3 Scattering cross section

Since energy transfer E_t involves the factor $\sin^2(\theta/2)$, if the scattering angle θ is small enough, energy transfer to atomic nuclei is negligible (as shown in Table 2-1). On the other hand, high-angle scattering (Rutherford scattering) results in a large energy transfer to the nuclei, but the probability of such high-angle scattering events is very low.

We evaluate the probability of each scattering event using the total scattering cross section σ . Transformation occurs when the energy transfer E_t becomes greater than the energy barrier E_b . Therefore, σ for an energy transfer $E_t \geq E_b$ is given by,

$$\sigma(\theta_{min}) = 2\pi \int_{\theta_{min}}^{\pi} \frac{d\sigma_{el}}{d\Omega} \sin\theta d\theta = \frac{4Z^2 R^4 (1 + E/E_0)^2}{a_H^2} 2\pi \int_{\theta_{min}}^{\pi} \frac{\sin\theta}{[1 + (\theta + \theta_0)^2]^2} d\theta$$

with $R = a_H Z^{-1/3}$, $\theta_0 = \lambda/2\pi R$.

Here θ_{min} is the minimum scattering angle given by the equation for E_t shown above, $d\sigma_{el}/d\Omega$ is the differential elastic cross section, a_H is the Bohr radius (5.29×10^{-11} m), E is incident electron energy (0.08 MeV), E_0 is rest energy of electron (0.511 MeV), λ is wavelength of incident electrons (4.18×10^{-12} m) and Z is the atomic number.

Figures 2-11(a) and (b) show E_t and σ values, respectively, as a function of scattering angle θ , and $E_t(\sigma)$ is plotted in Fig. 2-11(c). Figure 2-11(d) shows a time interval t of each event as a function of energy transfer to C. The time t is inversely proportional to the product of σ and the electron beam current density j ($t = 1/\sigma j$). We calculated t using $j = 1 \times 10^5$ e⁻/s·Å², which was typical for our atomic-resolution imaging experiments.

Under this condition, C atoms in graphene receive 1.3 eV every ~1s and 12.3 eV every ~100 s on average. The diffusion energy barriers of physisorbed atoms on graphene are typically below 0.5 eV; therefore, it is not possible to observe atomic diffusion on graphene by TEM. On the other hand, high-angle scattering is much less probable than low-angle scattering (Fig. 2-11(b)), and is not observed even during ~1 hour of TEM observation.

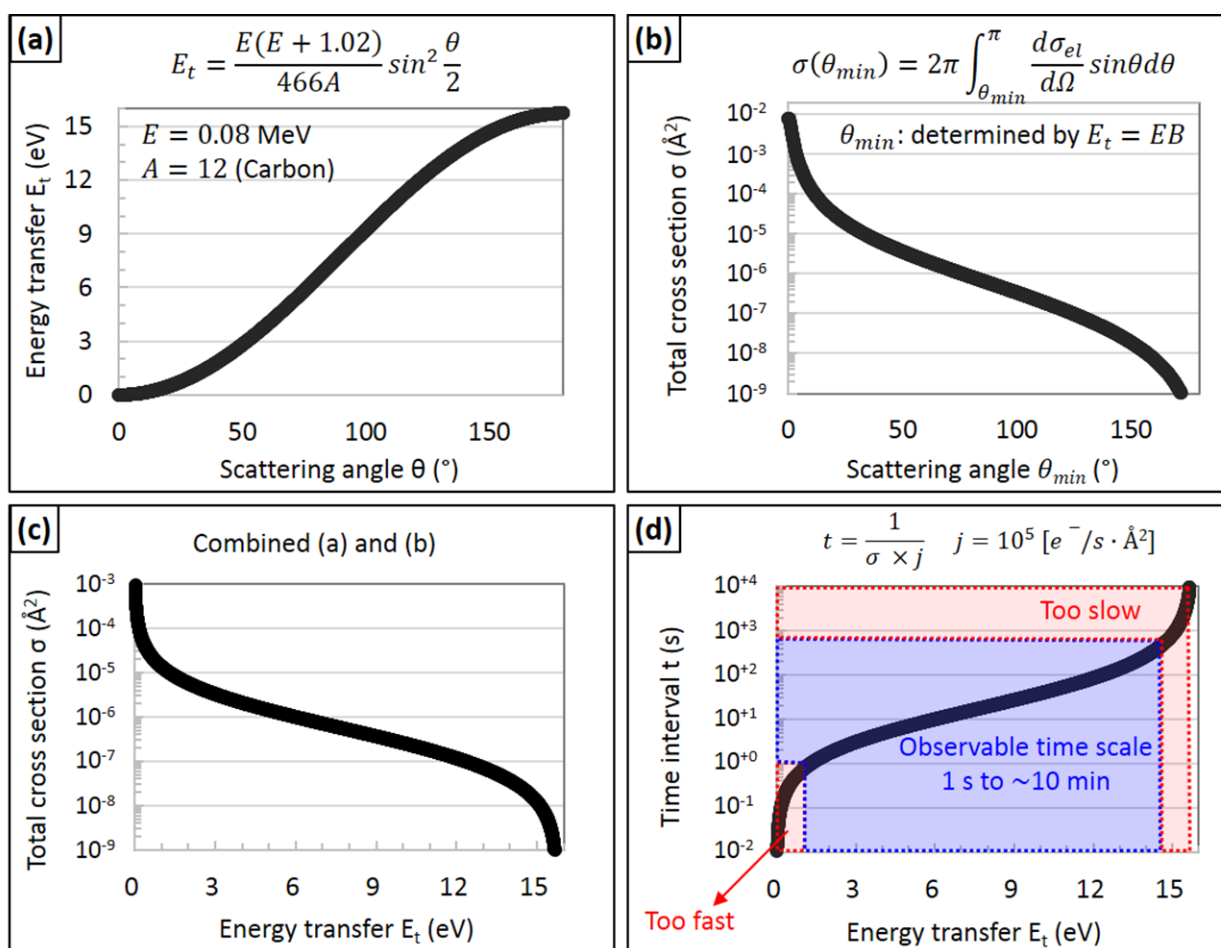


Figure 2-11 Energy transfer to C and its scattering cross section

(a) Energy transfer E_t to C from an 80 keV electron as a function of the electron scattering angle θ . (b) The scattering cross section σ as a function of θ . (c) σ as a function of E_t . (d) Time interval t as a function of E_t . Blue shaded area can be observed by TEM at time resolution 1 s.

Figure 2-12 summarizes the energy transfer to C, Cu and Pt from 80 keV incident electrons. As described above, the maximum value of energy transfer is lower for metals than C atoms due to their high atomic mass number. Meanwhile, the scattering cross section is high even at high-angles,

so that Cu or Pt atoms nearly continuously receive ~ 3 or ~ 1 eV, respectively. Pt is three times heavier than Cu, and thus the energy transfer to Pt is small. This difference might affect the stability of metal atoms observed under electron beam irradiation during TEM imaging experiments; however, the difference is much smaller than the energy transfer to C atoms.

In our TEM experiments, electron irradiation induced a variety of transformations, as C atoms received a wide range of energy (~ 1 – 15 eV) over various time intervals. We can estimate the energy barrier for each transformation by analyzing the related time intervals (Chapter 3).

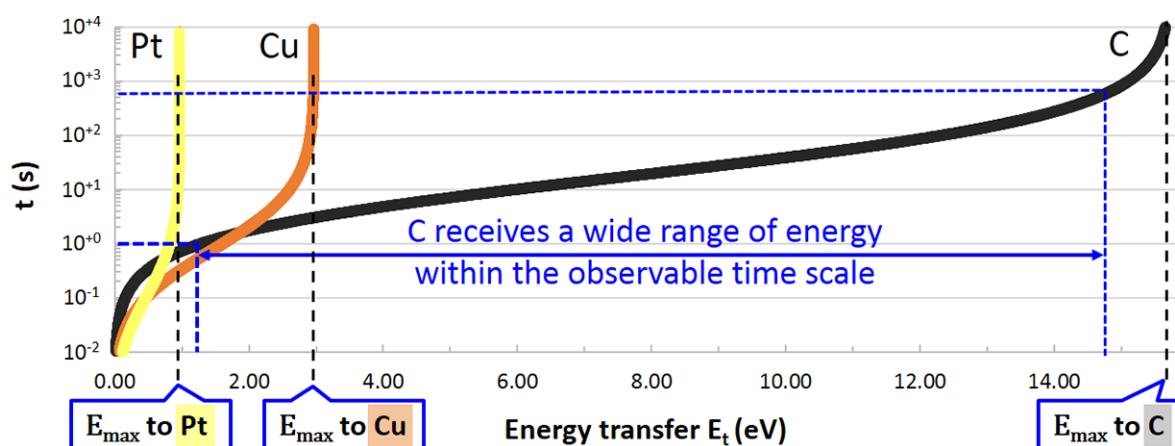


Figure 2-12 Energy transfer to C, Cu and Pt from 80 keV incident electrons

Time interval $t = 1 / \sigma j$ as a function of energy transfer E_t , using a tentative value of $j = 1 \times 10^5 \text{ e}^-/\text{s} \cdot \text{\AA}^2$.

2-3 Sample preparation

Since graphene is a one-atom-thick material, preparation of clean samples is a key factor for atomic scale observations. Here we summarize the graphene synthesis and experimental methods and conditions used in this thesis. The first section (2-3-1) outlines the graphene growth, and the following sections elaborate the transfer processes (2-3-2) and the effect of heating before and after the metal deposition (2-3-3).

2-3-1 Chemical vapor deposition (CVD)

While mechanical exfoliation of graphite [1] had triggered the graphene boom, it does not provide a sufficient graphene yield for most applications. Many other graphene synthesis methods have been explored, such as chemical exfoliation from graphite [180]–[182], chemical reduction of graphene oxide [6], [183], [184], CVD using catalytic metals [82], [185] or nonmetals [172], epitaxial growth on SiC [186], and so on. Among these techniques, CVD appears most promising and best established in industrial settings.

The quality of CVD graphene (number of layers, stacking orientations, grain sizes, amount of topological defects, etc.) strongly depends on the metal substrate. In most applications, graphene needs to be transferred to other substrates (e.g. PET film for transparent electrodes or SiO₂/Si for field effect transistors). Researchers tried to grow graphene on many metallic substrates (Pd, Ru, Ir, Pt, etc.); however, such metals are expensive and hinder the graphene transfer. Then Ni and Cu became the most suitable candidates because they are inexpensive and can be easily etched away by chemical solutions, so that graphene grown on Ni or Cu can be transferred onto an arbitrary substrate. Ni was the popular catalyst in early studies; however, the resulting graphene had unsuitable uniformity and thickness (see Appendix Fig. A-6).

Researchers investigated the growth mechanisms and found that the carbon solubility of the metal catalyst is a key factor. Li *et al.* [185] experimentally revealed the different graphene growth mechanisms on Ni and Cu. In the Ni case, first, Ni catalytically decomposes the feedstock (e.g. methane gas). Second, C and Ni form a solid solution at high temperatures (above 800 °C), due to the large carbon solubility of Ni in C (0.6 wt% at 1326 °C) [187]. Third, C diffuses out of Ni when cooled. This “carbon segregation” is heterogeneous at Ni grain boundaries, which results in a formation of non-uniform graphene with small grains. In contrast, Cu has a low carbon solubility

Chapter 2

at high temperatures (0.008 wt% at 1084 °C) [187]; therefore, graphene formation on Cu occurs as a “surface process”. After the first layer of graphene forms on a Cu foil, Cu cannot decompose further feedstock, and therefore, we can obtain single-layer graphene over large areas.

We examined several CVD graphene samples which were purchased from a company or were provided by our collaborators: single-layer graphene (Graphene Platform Corporation), AB-stacked double-layer graphene (collaborated with Dr. Sakai and his coworkers, National Institutes for Quantum and Radiological Science and Technology), nitrogen-doped multi-layer graphene [173] (collaborated with Dr. Kalita, Prof. Tanemura and their students, Nagoya Institute of Technology). These three samples were grown on a Cu foil under different conditions.

We also examined graphene grown on Ni (Ni-deposited membrane on SiO₂/Si substrate, Graphene Supermarket[®]) or on nonmetal substrates using a Ga vapor catalyst [172] (collaborated with Dr. Murakami, Prof. Fujita and their students, University of Tsukuba). However, the former sample was a non-uniform multi-layer graphene with small random grains because of the reason described above. The latter material was almost single-layer graphene, but consisted of small grains (50–200nm in lateral size) and contained residual Ga catalyst.

The features of CVD graphene samples varied according to their growth conditions, and we finally chose the purchased graphene grown on a Cu foil (Graphene Platform) for this thesis, because we needed single-layer graphene without metal or SiO₂-based impurities. Although the graphene membrane was polycrystalline (grain sizes: ~1–3 μm in lateral size, shown in Fig. 2-6, 2-7 and A-6), it contained less impurities, and mostly consisted of single-layer graphene.

The photograph in Figure 2-13 shows CVD equipment (Graphene Platform Corporation) just after the graphene growth. We do not know the exact growth conditions (e.g. gas parameters), as they are industrial secrets. A general description is as follows: insert a Cu foil into an electric furnace and evacuate it, raise the temperature up to 1000 °C (over a period of ~1 hour) in a hydrogen gas atmosphere, flow carbon source (methane gas) at 1000 °C for ~30 min and naturally cool the sample inside the quartz-tube. Hydrogen gas should flow until graphene/Cu is cooled to the room temperature.

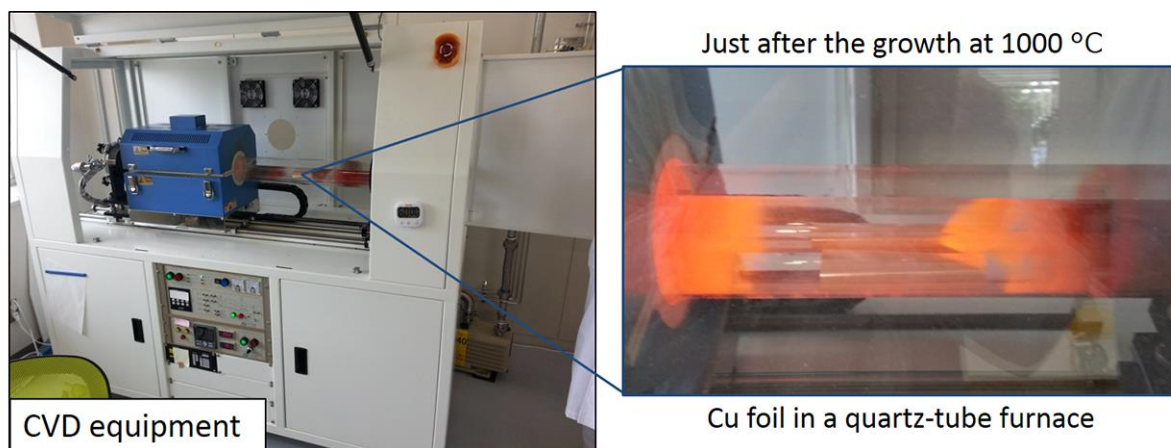


Figure 2-13 Photographs of CVD equipment for graphene growth

As a result, a uniform single-layer membrane of polycrystalline graphene grew on the entire Cu surface (both sides of the foil). The next subsection elaborates the transfer process used to prepare TEM samples.

2-3-2 Transfer process

CVD graphene was transferred onto TEM grids or *in situ* heating chips using the poly(methyl methacrylate) (PMMA) support method. Because of surface contamination by polymer residues, other methods without using PMMA have been proposed, for example, utilizing surface tension of IPA (isopropanol) drop as an adhesion bond with carbon support film on a TEM grid [83]. This method proved to be difficult to reproduce in our laboratory. PMMA is a popular material in device processing [13], [85], [188], and its handling is well explained in the literature. Hence, we used PMMA and paid meticulous attention to minimize impurities, hydrocarbon contaminants, wrinkles and cracks, all of which hinder atomic-resolution imaging and degrade graphene properties. Preparing a clean sample is crucial for observing graphene by TEM, and the technique improved here might also be useful for device processing.

The important point in our method is removal of metallic impurities. FeCl_3 solutions are the most widely used Cu etchants [13], [14], [150], [151], [154], [156], [168], [169], [171], [187]–[189], yet they leave some Fe-based contamination on graphene. Although some researchers observed residual Fe atoms in FeCl_3 -treated graphene by TEM [150], [154], [156], this method is not appropriate for studying other metal atoms. Furthermore, residual metal impurities often attracted hydrocarbon contaminants under electron irradiation [190] and/or damaged graphene

during high-temperature annealing [118]. To avoid those unwanted effects, we used a metal-free aqueous solution of $(\text{NH}_4)_2\text{S}_2\text{O}_8$ (ammonium persulfate) followed by a rinse in HCl to remove both Cu and CuO. Even when we aimed to observe Cu, we minimized the residual Cu first, and then intentionally deposited Cu by sputtering a Cu target onto clean graphene.

Figure 2-14 briefly summarizes the transfer process. First, a thin PMMA film was spin-coated and cured on graphene/Cu. Second, Cu was etched away using a metal-free aqueous solution of $(\text{NH}_4)_2\text{S}_2\text{O}_8$ (Sigma Aldrich). Third, the PMMA/graphene film was rinsed in deionized (DI) water and transferred to a concentrated HCl solution to remove residual contaminants. A thorough rinse in DI water followed. Fourth, the PMMA/graphene film was transferred to a TEM grid or a heating chip and dried naturally overnight. Finally, PMMA was dissolved in acetone for ~2 hours.

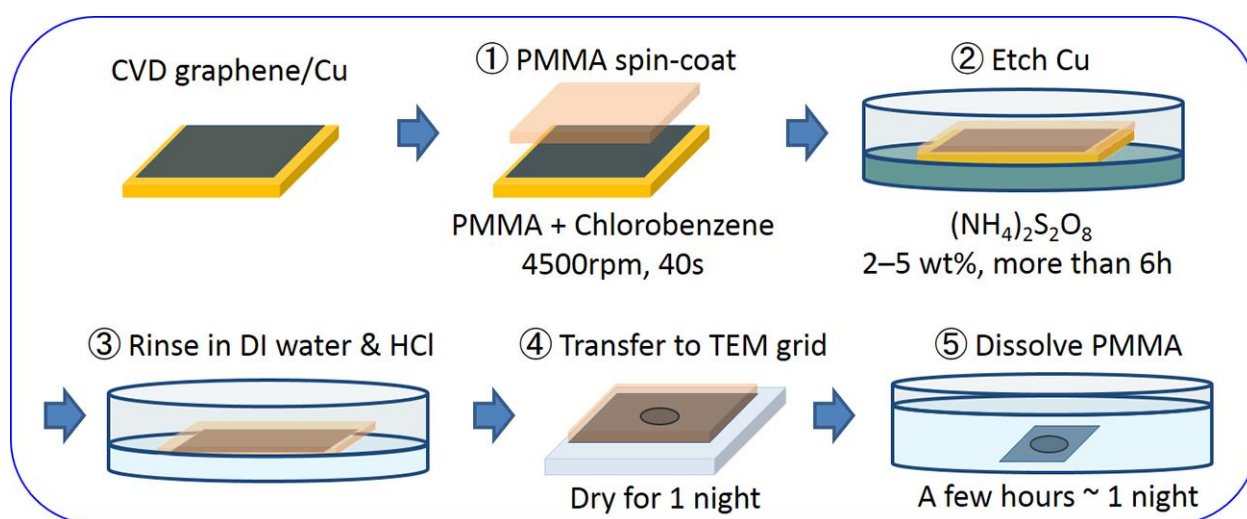


Figure 2-14 Schematic of graphene transfer processes

Now we explain each step using photographs. In the first step of PMMA coating, the PMMA film should be thin enough not to strain graphene, while keeping a suitable thickness for handling the film on the solutions surface. We dissolved PMMA powder (996 molecular weight, Sigma Aldrich) by chlorobenzene (0.46 g / 10 ml). It is not necessary to create PMMA solution every time, but the concentration should be controlled, as chlorobenzene is highly volatile. We always checked the amount of solution before and after we used it (Fig. 2-15(a)). Before spin-coating PMMA, a thermal release tape was attached to the back of the Cu foil to keep the Cu foil flat and prevent it from PMMA coating; the PMMA-coated areas are hardly etched away by the following acid treatment. After the PMMA was spin-coated onto the top side of graphene at 4500 rpm for 40

s, the tape was released during the curing of PMMA at 180 °C for 5 min (Fig. 2-15(b)). CVD graphene grew on both sides of the Cu foil. We removed graphene from one side of the foil to avoid stacking and formation of misoriented double-layer graphene. The extra graphene layer was etched by 10 wt% $(\text{NH}_4)_2\text{S}_2\text{O}_8$ solution for 10 min (Fig. 2-15(c)). The foil was then gently rubbed with Bemcot wipers in water. During this removal process, the PMMA-coated side was covered by a PET film to prevent PMMA/graphene from breaking (Fig. 2-15(d)).

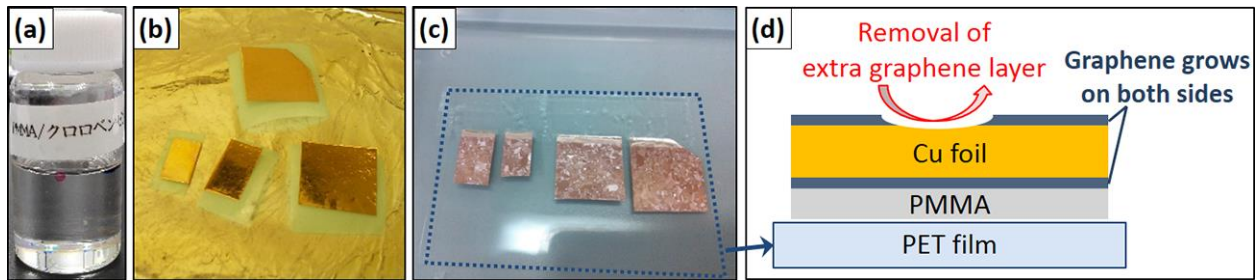


Figure 2-15 PMMA coating and removal of extra graphene

Photographs of (a) chlorobenzene solution of PMMA, (b) curing of PMMA and (c) removal of extra graphene. (d) Schematic of CVD graphene sample during the removal of extra graphene shown in (c). As shown in (b), the light green tape released shortly after set it on a hot plate at 180 °C. The photograph (c) shows partial etching of Cu back side as well as graphene in a 10 wt% $(\text{NH}_4)_2\text{S}_2\text{O}_8$ solution.

In the second process (etching of Cu shown in Fig. 2-14), we used low concentrations of 2–5 wt% $(\text{NH}_4)_2\text{S}_2\text{O}_8$ solution for ~6–20 hours. Although the etching rates by $(\text{NH}_4)_2\text{S}_2\text{O}_8$ solutions are lower than other metal-free etchants (e.g. HCl, HNO_3 and H_2O_2), the acid treatment could damage graphene as well as Cu. We examined the damage threshold, and confirmed that the condition described above induced no detectable damage to graphene, while etching Cu almost completely. Figure 2-16 shows photographs taken during Cu etching. The PMMA/graphene film was transferred to a new acid solution after the visible Cu film was etched away (within ~1 hour), followed by further removal of microscopic Cu for more than 6 hours.

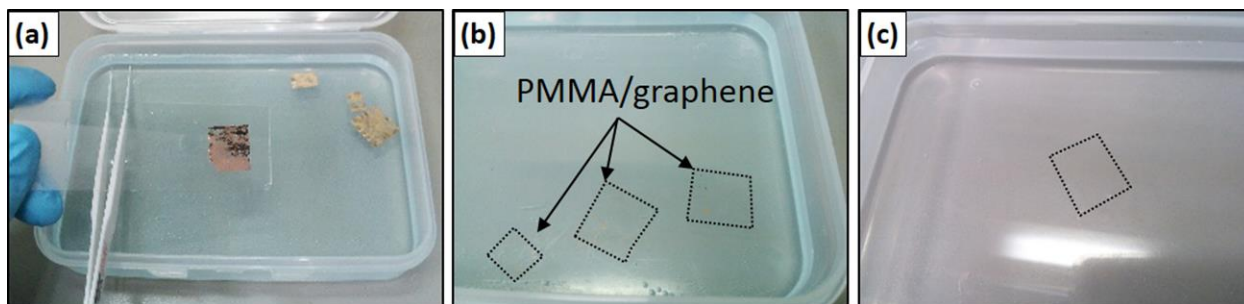
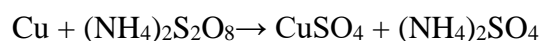


Figure 2-16 Etching of Cu by $(\text{NH}_4)_2\text{S}_2\text{O}_8$ solution

Photographs of (a) handling the film with a glass slide and ceramics tweezers, (b) PMMA/graphene film floating on the surface of $(\text{NH}_4)_2\text{S}_2\text{O}_8$ solution and (c) PMMA/graphene film on a new colorless $(\text{NH}_4)_2\text{S}_2\text{O}_8$ solution. The solution shown in (a) and (b) turned blue due to dissolved Cu^{2+} ions.

In the third process (cleaning shown in Fig. 2-14), a rinse in HCl solution is a key factor. We found that hydrocarbon contaminants on graphene surface became mobile, and could be easily removed by electron irradiation during TEM observation. We attributed this mobility to the reduction of copper oxide and/or activation of hydrocarbon contaminants. Cu etching by $(\text{NH}_4)_2\text{S}_2\text{O}_8$ solution is an oxidation reaction, and some Cu^{2+} ions attach to the graphene surface forming CuO or Cu_2O , which are insoluble in water but dissolve in HCl. The chemical reactions are as follows:



We presumed that an alternative rinse in HCl and $(\text{NH}_4)_2\text{S}_2\text{O}_8$ solution may remove both Cu and CuO. Hence, samples were rinsed in HCl for ~10 min twice, and were moved back to $(\text{NH}_4)_2\text{S}_2\text{O}_8$ for 30 min. This acid treatment caused no detectable damage to graphene, and Cu was almost completely removed. The PMMA/graphene film was then rinsed in DI water for more than 6 hours (while exchanging water several times) to remove HCl and $(\text{NH}_4)_2\text{S}_2\text{O}_8$.

We slightly changed the fourth and fifth processes (transfer and dissolution of PMMA shown in Fig. 2-14) to fit the transfer targets: TEM grids (Quantifoil[®], Quantifoil Micro Tools GmbH) and *in situ* heating chips (E-chips for Aduro[™], Protochips). We describe them separately.

The Quantifoil TEM grids were made of Au (3 mm in diameter) covered with an amorphous carbon support film with 2 μm diameter holes. They are robust, but flexible enough to make a

good contact with a PMMA/graphene film. We placed TEM grids on a glass plate, and pulled the PMMA/graphene film out of DI water, using glass plate as a tool to keep the film and grids flat. Figures 2-17(a) and (b) show the grids before and after this pulling-out process. After draining off water drops between the film and the glass plate by gentle air blow, the plate was dried naturally for more than 6 hours or overnight. Finally, PMMA was dissolved in acetone for ~2 hours, while exchanging acetone by pipette (Fig. 2-17(c)). Although careful control is necessary when picking up grids from acetone, we have successfully transferred graphene onto TEM grids (Figs. 2-17(d) and (e)).

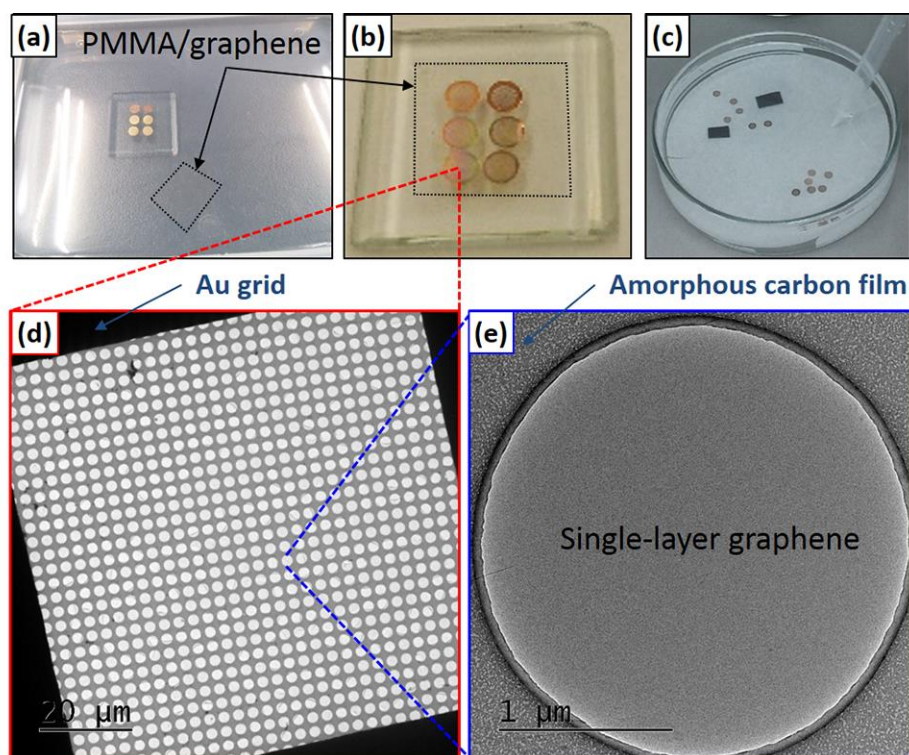


Figure 2-17 Transfer onto TEM grids

Photographs of (a) PMMA/graphene film floating on water surface and TEM grids dipped in water on glass plate, (b) PMMA/graphene/TEM grids/glass plate and (c) dissolving PMMA in acetone. (d), (e) Low-magnification TEM images of graphene transferred onto Quantifoil grid.

In contrast to conventional TEM grids, the graphene transfer onto *in situ* heating chips was difficult and required extra care. Figure 2-18 shows the structure of an *in situ* heating chip, where a Si substrate (~3 × 5 mm in lateral size) was covered with a SiN film and an amorphous carbon support film having ~5 and 2 μm diameter holes, respectively. Each chip had a small window (0.5

$\times 0.5 \text{ mm}^2$ in size) and Au electrodes on both sides. When we transferred graphene onto the chips using the methods described above, the chip resistance considerably decreased. Au electrodes should be covered by an insulator, but the reduction of the resistance indicates that graphene directly attached to the electrodes. This reduction made the heating temperature inaccurate, because the heating chips do not record the actual temperature and resistance during heating, but rely on the pre-measured resistance of original chips. Hence, we tried to avoid the resistance change by thinning down the PMMA/graphene film as shown in Fig. 2-18 (a). The film width must be less than 0.5 mm; therefore, a more careful control is required.

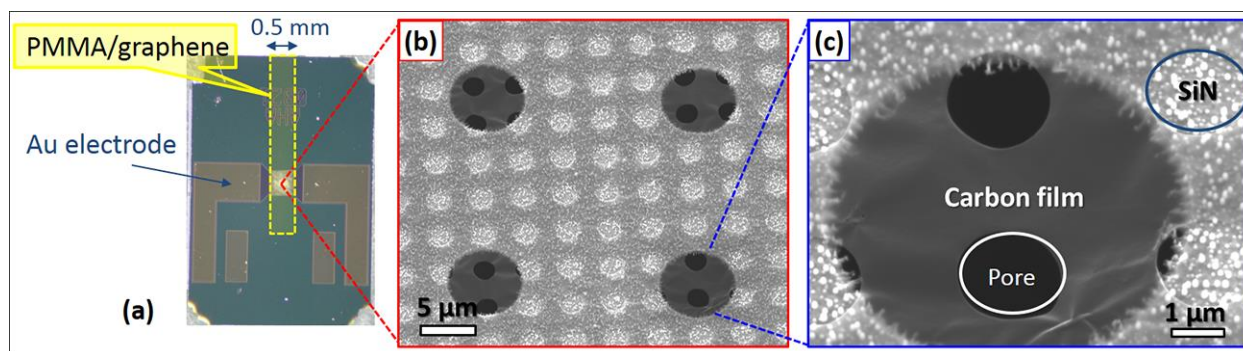


Figure 2-18 Transfer onto *in situ* heating chips

(a) Photograph of *in situ* heating chip (E-chips for Aduro™, Protochips) with annotations. PMMA/graphene film transferred onto yellow box region without connect with Au electrodes. (b), (c) SEM images of C/SiN films.

Mechanical forces generated at the interface between the hard Si substrate and PMMA often broke graphene. We tried to improve the graphene coverage by introducing two extra measures. First, Suk *et al.* reported that the PMMA film softened by heating above its glass transition temperature at 150 °C, and the coverage of suspended graphene was improved [191]. Thus, we heated the sample at 180 °C for 30 min, according to the reported conditions. Second, fast evaporation of acetone often damaged graphene and the thin carbon support film. Therefore, after PMMA was dissolved, acetone was exchanged for ethanol, so that the slow evaporation of ethanol would not damage graphene.

In summary, we strived to minimize metal impurities during the transfer of CVD graphene by means of PMMA support methods with metal-free etchant $(\text{NH}_4)_2\text{S}_2\text{O}_8$ and HCl. The handling

difficulty and quality of transferred graphene depended on the target substrates: Quantifoil TEM grids or *in situ* heating chips. We obtained acceptably clean graphene samples suspended on Quantifoil TEM grids. On the other hand, heating chips needed a further improvement to minimize the hydrocarbon contamination. The contamination increased during the PMMA/graphene heating and dipping in ethanol. As mentioned above, these processes improved graphene coverage, but also increased hydrocarbon residues originated from melted PMMA and ethanol.

Annealing inside TEM column can reduce the hydrocarbon contamination. The next subsection elaborates the heating effects before and after the metal deposition.

2-3-3 *In situ* heating effects

We have annealed the transferred CVD graphene, mainly aiming to reduce chemical etching effects of water vapors or oxygen residues and to enlarge clean graphene patches free from hydrocarbon contaminants. Note that we heated the samples for the experiments presented in Chapters 3–5, but not for the experiment in Chapter 6. In Chapter 6, the presence of oxygen was critical for the formation of 2D copper oxide, but heating resulted in the removal of oxygen residues incorporated from air or PMMA.

Lin *et al.* [85], Algara-Siller *et al.* [192] and Longchamp *et al.* [193] reported that *ex situ* annealing in specific conditions (in hydrogen gas atmosphere, in activated carbon, and on platinum deposited film, respectively) would reduce hydrocarbon contaminants. We confirmed that such annealing reduces initial PMMA residues; however, once the sample was heated and exposed to the air, it attracted more contamination under irradiation by a focused electron beam. In some cases, beam-induced contamination hindered room-temperature TEM observations, presumably because annealing made the sample surface highly reactive.

Hence, we heated the sample inside the TEM column ($\sim 10^{-5}$ Pa) before the metal deposition. We used two commercial *in situ* heating holders, which were made by Protochips and Gatan Inc. The Protochips holder has excellent mechanical stability at high temperatures (up to 1200 °C), which is suitable for the atomic-resolution imaging. The stability of Gatan holder is worse, but it can be utilized with conventional TEM grids, and allows direct temperature measurements using a thermocouple. *In situ* heating in atomic-resolution imaging (Chapters 3–5) was realized with the Protochips heating holder.

Figures 2-19(a)–(c) show TEM images of transferred graphene at room temperature. At first, the clean graphene patches had a typical size of $20 \times 20 \text{ nm}^2$. Figures 2-19(d) and (e) show TEM images of graphene heated at $\sim 1000 \text{ }^\circ\text{C}$ in a TEM column. Heating resulted in clean graphene patches of $\sim 1000 \times 1000 \text{ nm}^2$ in size: most hydrocarbon contaminants remained at the step edges or grain boundaries, while the other areas were clean.

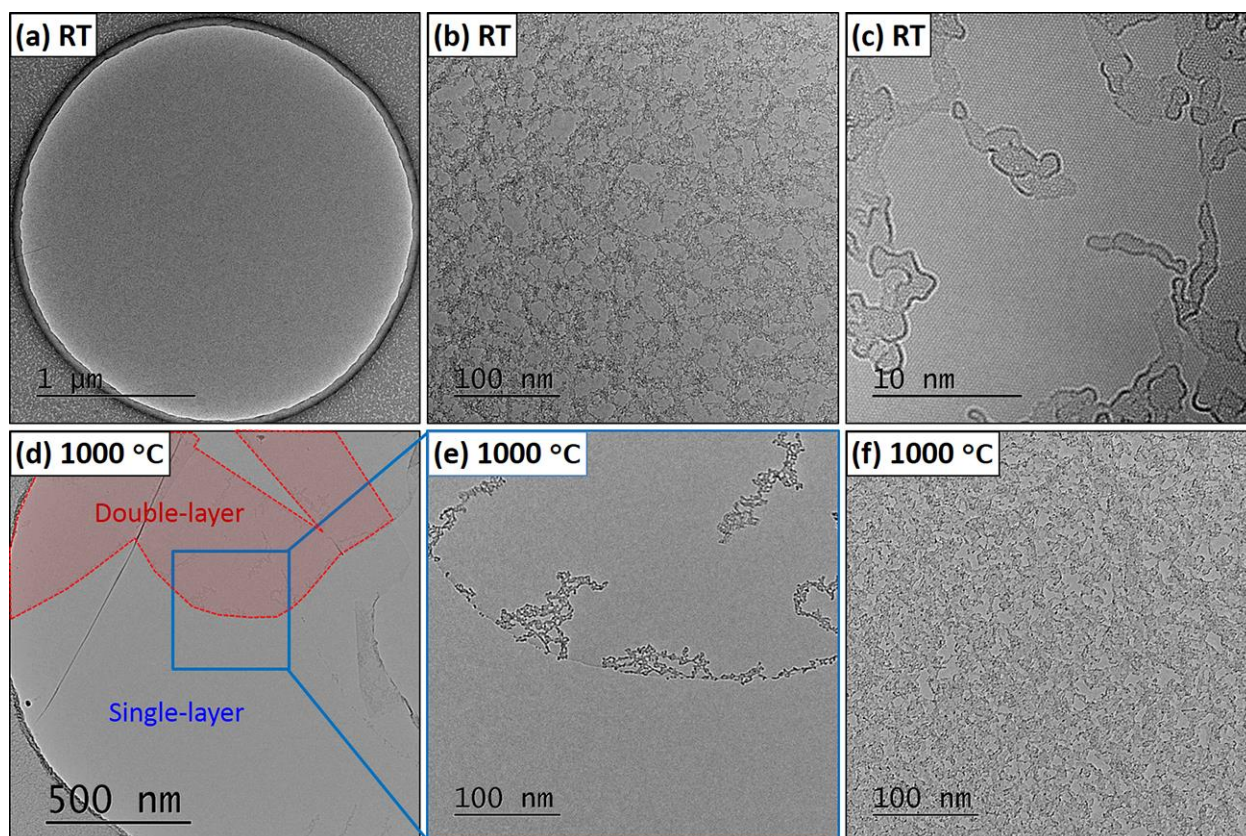


Figure 2-19 Graphene before and after heating

(a)–(c) TEM images taken at room temperature (RT) without annealing. (d) and (e) TEM images taken at $1000 \text{ }^\circ\text{C}$. After heating, the single-layer graphene regions shown in the lower parts of images (d) and (e) are almost perfectly clean. (f) TEM image of the graphene region irradiated by electron beam prior to annealing at $1000 \text{ }^\circ\text{C}$.

The TEM image in Figure 2-19(f) at $1000 \text{ }^\circ\text{C}$ shows no effect of annealing. As shown in Fig. 2-19(c), strong electron beam irradiation at high magnification has partly graphitized amorphous hydrocarbon contaminants and fixed them on graphene. This observation taught us to avoid

electron irradiation at room temperature, because it fixed contaminants that could not be removed by either heating or electron-induced sputtering.

Now we describe heating effect on metal-deposited graphene. Metals were deposited on graphene using an ion beam etching system (PECS, Gatan) for Cu, DC plasma sputtering system (JFC-1600, JEOL) for Pt and electron beam deposition system (RDEB-1206K, R-DEC) for Au. The samples were exposed to the air before TEM experiments, which led to incorporations of oxygen, hydrocarbons and water. Yuzvinsky *et al.* [194] reported that if samples contained oxygen or water, electron beam had significantly increased the cutting speed of carbon nanotubes, because electron irradiation created highly reactive radicals, which reacted with carbon materials. Therefore, we heated the sample at 150 °C or higher to remove them.

Metal nanoparticles started to evaporate at much lower temperatures than the bulk melting point. For example, the melting point of bulk Cu is 1085 °C, while Cu nanoparticles evaporated at ~300 °C. Electron beam irradiation also promoted the aggregation and evaporation of Cu, therefore we took a low-magnification TEM image and then turned off the beam. About half of the nanoparticles disappeared after 11 h of heating at 300 °C. At ~ 500 °C, Cu has rapidly disappeared. To avoid rapid evaporation, we observed all the metals at 150–300 °C.

Interestingly, when graphene was cleaned up by heating prior to Cu deposition (Fig. 2-20(a)), particle sizes varied depending on the number of underlying graphene layers (Figs. 2-20(b)–(d)). Figures 2-20(c) and (d) show TEM images of single- and double-layer graphene, respectively, after the Cu deposition. Their difference indicates that stacking of graphene layers significantly weakened their interaction with metals. This difference appeared only when graphene was heated before and after the deposition, so that metal atoms and nanoparticles could freely migrate on the clean graphene surface.

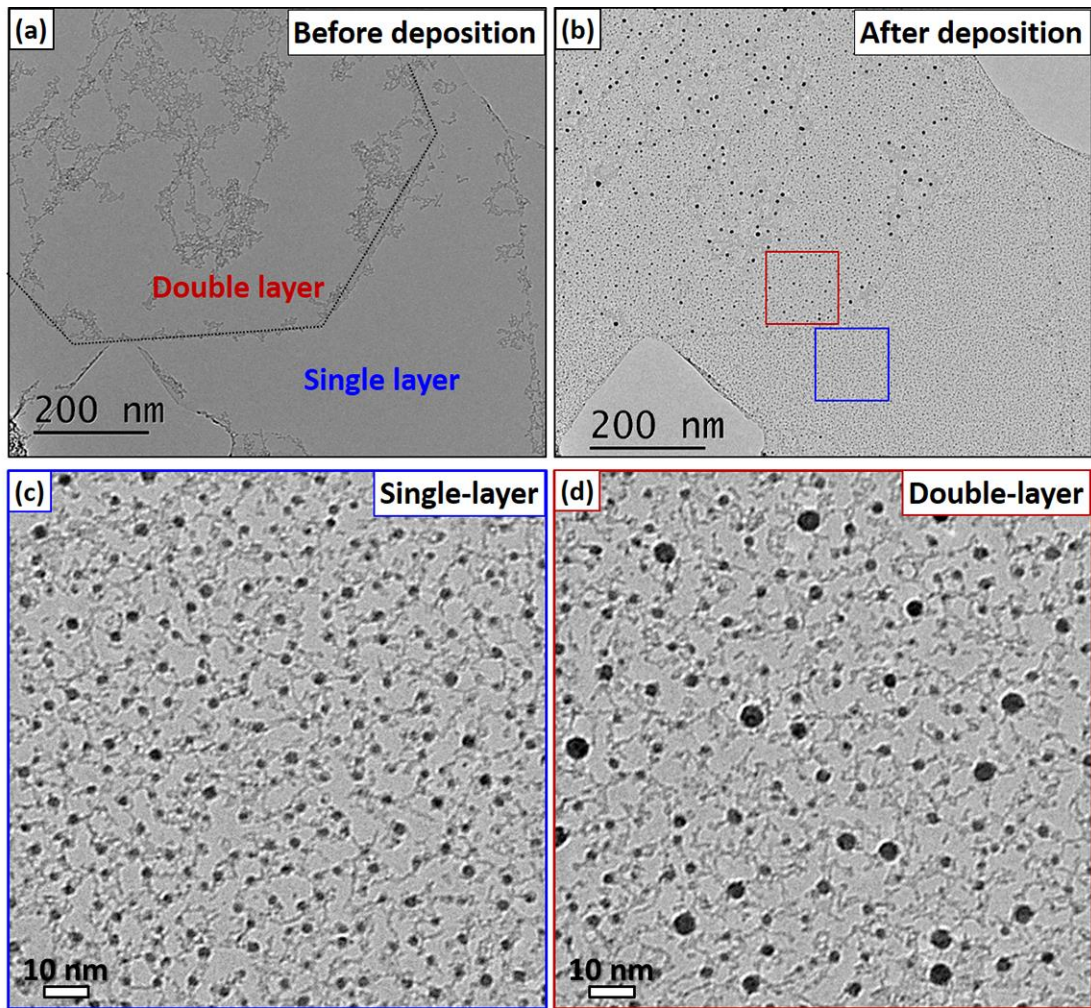


Figure 2-20 Particle size difference on single- and double-layer graphene

TEM images of graphene (a) before and (b)–(d) after Cu deposition. TEM image (a) was observed at 1000 °C, while the others were observed at 300 °C. Panels (c) and (d) are magnified images of the boxed regions in (b); they show single- and double-layer graphene, respectively. Cu particles are clearly larger on double-layer graphene than on single-layer graphene.

Chapter 3

Cu atoms reknit graphene structure

Metal doping into the graphene lattice has been studied recently to develop novel nanoelectronic devices and to gain understanding of the catalytic activity of metals in nanocarbon structures. In this chapter, we report direct observation of interactions between substitutional Cu atoms and C atoms in graphene. We document stable configurations of Cu atoms in the graphene sheet and unique transformations of graphene promoted by Cu atoms. First-principles calculations reveal a reduction of energy barrier that caused rotation of C–C bonds near Cu atoms. We discuss two driving forces, electron irradiation and *in situ* heating, and conclude that the observed transformations were mainly promoted by electron irradiation. Our results suggest that individual Cu atoms can promote reconstruction of single-layer graphene. We focus on interactions between Cu atoms and graphene in this chapter, while the next chapter discusses the different behaviors of Cu, Pt and Au atoms at graphene edges.

3-1 Introduction

Interactions between metals and graphene have been extensively studied aiming to control the local properties of graphene for applications in electrocatalysts and nanoelectronic devices [15], [151], [195] and to create novel carbon nanostructures [185], [196]–[198]. Theoreticians predicted that transition metal atoms in graphene vacancies have unique electronic and magnetic properties [113], [114], [199]. However, there are only a few experimental reports on such metal–graphene systems, due to the difficulty of their direct observation. Recently, researchers applied aberration-corrected (S)TEM to observe metal atoms in a graphene sheet, such as Fe dimers [151] and single atoms of Pt, Co and In [152] substituted in carbon vacancies in graphene, as well as etching of graphene mediated by metal atoms (Cr, Ti, Pd, Ni or Al)[155]. These studies suggest that most metal atoms, except for Au, promote etching of graphene. The etching can be destructive and may hinder practical applications.

Here we report the structure and dynamics of Cu atoms embedded in a single-layer graphene observed by aberration-corrected TEM. We selected Cu because it has a similar electronic

configuration to Au, and is known to be the best catalyst for graphene growth [82], [187], [200]. Hence, Cu will not etch graphene and is expected to catalyze the growth or modification of graphene structures. We directly observed unique morphological changes in Cu-doped graphene that have not been observed with other metals: reconstruction of graphene grains, various transformations promoted near Cu atoms, and formation and mending of graphene nanopores. We performed first-principles calculations based on density functional theory (DFT) to explain the observed stability and dynamics, as well as Cu-assisted transformations of graphene.

3-2 Methods

This section provides specific experimental methods for this chapter, and all the details are described above in section 2-3. Note that Dr. Kaneko (NIMS) performed first-principles calculations according to the experiment within a collaborative research.

3-2-1 Sample preparations

Single-layer graphene on a Cu foil (Graphene Platform Corporation) was transferred onto an *in situ* heating chip (E-chips for Aduro™, Protochips). Figure 3-1(a) is a STEM image taken before the Cu deposition; heating in a TEM column ($0.6\text{--}1\times 10^{-5}$ Pa) at temperatures above 400 °C created clean graphene patches about 200×200 nm² in size. A small amount of Cu was then deposited onto graphene using an ion beam etching system (PECS, Gatan).

When observed at room temperature just after deposition, Cu had not formed crystals; it was dispersed with oxygen and hydrocarbons. Oxidized Cu nanoparticles under electron beam irradiation promoted etching of graphene, whereas pure Cu nanoparticles did not. Therefore, we heated the sample to remove oxygen. The annealing temperature was set at 300 °C or lower because Cu atoms and nanoparticles gradually evaporated at 300 °C and rapidly disappeared at ~500 °C. Although most Cu formed nanoparticles when heated (the size distributions are shown in Figs. 3-1 (b) and (c)), we could also observe individual Cu atoms that were trapped by small contamination patches on graphene or by vacancies in graphene.

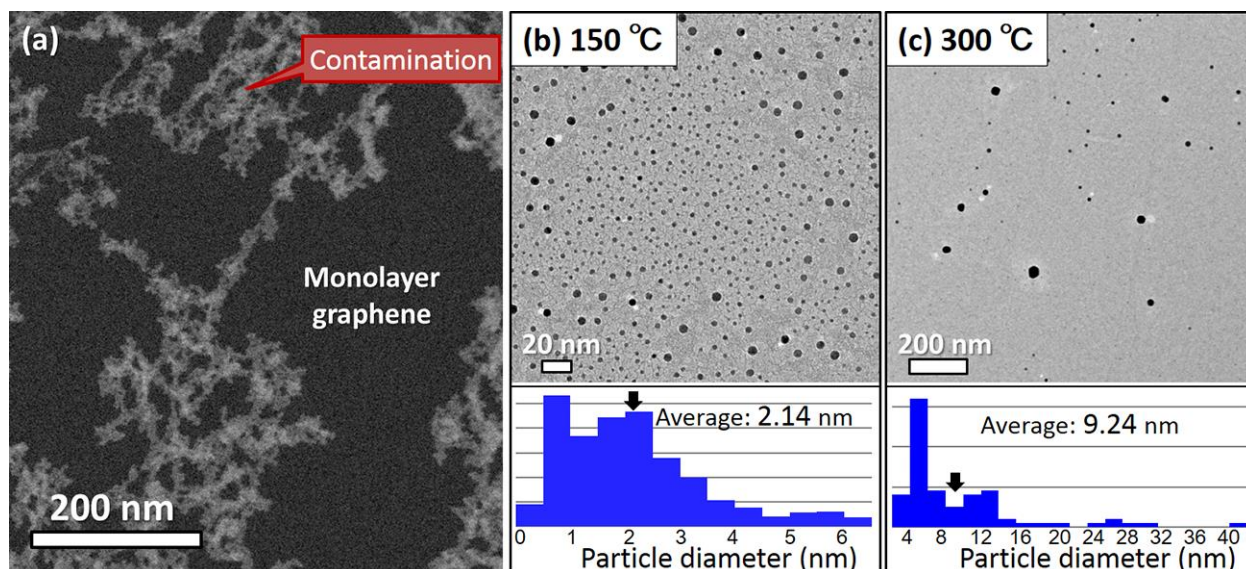


Figure 3-1 Selecting observation areas

(a) Low-magnification STEM image taken before the Cu deposition above 400 °C. (b) and (c) TEM images of Cu deposited graphene heated at 150 °C and 300 °C, respectively. Corresponding particle size distributions are shown below the images.

Si contamination was possible because we used quartz-tube furnaces and SiN *in situ* heating chips, yet we believe that Si was a minor impurity and most of observed atoms were Cu due to the following reasons. First, we can exclude heavily Si-contaminated areas judging by Cu-nanoparticle sizes. As described in Chapter 2, nanoparticle size varies with the number of underlying graphene layers. Si impurity aggregated with hydrocarbon contaminants when the sample was heated before the Cu deposition, and Cu nanoparticles were clearly larger on the contaminated areas (as seen in the peripheral image areas in Fig. 3-1(b)) than on clean single-layer graphene. Therefore, further observations were carried out near the centers of the clean patches. Second, we performed STEM-EELS analysis before and after Cu deposition (Fig. 3-2). All nanoparticles around the observation areas (yellow frame in Fig. 3-2(b)) and a few dispersed atoms (Fig. 3-2(c)) were identified as Cu.

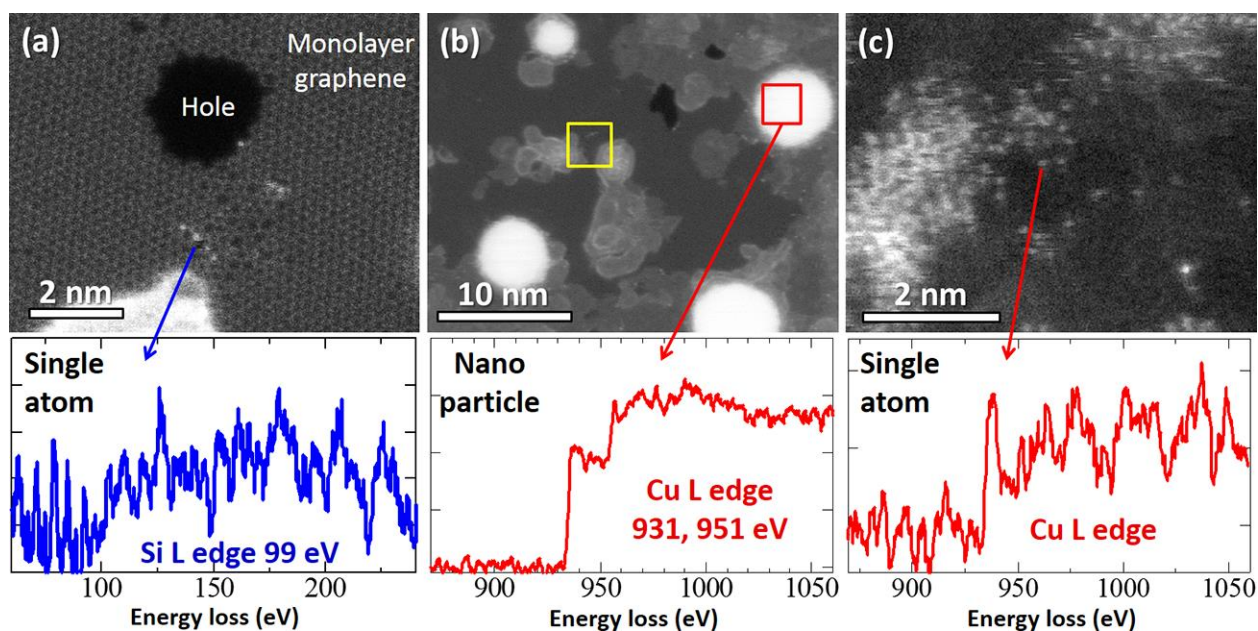


Figure 3-2 STEM-EELS data for Si and Cu

(a) Single Si atoms detected before the Cu deposition. After the Cu deposition, Cu was detected in (b) all the nanoparticles around the observed area (highlighted by the yellow frame) and (c) single atoms dispersed in/on the graphene.

3-2-2 TEM imaging experiments

We used aberration-corrected TEM (JEM-ARM200F, JEOL) operated at a low voltage of 80 kV to reduce knock-on damage to the graphene sheets. The sample temperature during observation was kept at 150 or 300 °C by an *in situ* heating holder (AduroTM, Protochips). Unless stated otherwise, most results are reported for 150 °C, but the frequency of each transformation type and lifetime for each structure were measured at both 150 and 300 °C. TEM movies were acquired at 0.5–2 frames/s. Snapshots from the TEM movies were processed as follows: frames were shifted to compensate for thermal drift, and then averaged and low-pass filtered to improve the signal-to-noise ratio.

3-2-3 First-principles calculations

We performed first-principles DFT calculations using the PHASE/0 code [201]. The generalized gradient approximation [202] and ultrasoft pseudopotential [203] were employed. Spin polarization was considered. The cut-off energies of the plane-wave basis set and charge density were taken at 25 and 255 Ry, respectively. Each defect was introduced in a graphene supercell of $6 \times 4\sqrt{3}$ periodicity (96 atoms). The lateral size of the unit cell was measured using the optimized lattice constant of graphene, 2.476 Å, which is 0.6% larger than the experimental value. The graphene sheet was isolated by a vacuum layer 10 Å thick (we used 12-Å-thick cells with ~2 Å distortion height). A Monkhorst and Pack mesh of $3 \times 3 \times 1$ size was used for k-sampling [204]. The atomic positions were optimized until the residual force became smaller than 5.0×10^{-4} hartree/bohr. To evaluate energy barriers, a climbing image nudged elastic band method with eight images was employed [205].

The geometrically optimized atomic models were redrawn using Materials Studio (BIOVIA).

3-3 Results and discussion

This section is divided in five subsections: stable configurations of Cu atoms in the graphene sheet (3-3-1), graphene reconstruction promoted by Cu atoms shown in large and small areas (3-2-2 and 3-3-3), discussion on driving forces (3-3-4), and discussion on reasons for different behavior of Cu from other metals (3-3-5). Most discussions are based on experimental facts, but the subsections 3-3-3 and 3-3-5 include first-principles calculations, which reveal a reduction of energy barriers for rotation of C–C bonds near Cu atoms. The repeated C–C bond rotations caused graphene reconstruction.

3-3-1 Cu sites in single-layer graphene

In the areas irradiated by focused electron beam, some Cu atoms replaced C atoms in the graphene lattice (Figure 3-3). This Cu substitution was frequently observed in areas containing residual oxygen and hydrocarbon contamination, while the substitution without any contaminants was rare, presumably because the contaminants reduced the energy required for Cu substitution.

The TEM image of Fig. 3-3(b) shows more than 10 Cu atoms embedded in a $\sim 4 \times 4 \text{ nm}^2$ area of graphene. We took TEM images at overfocus conditions to highlight Cu atoms, and Cu atoms appeared 1.8 ± 0.2 times brighter than C atoms. Multislice simulation for the present overfocus conditions yielded a Cu/C intensity ratio of 1.92 (further details on TEM image contrast are given in section 2-1).

Most of previous studies [113], [114], [151], [152], [199], [206] focused on metal atoms in single or double vacancies (Figs. 3-4 (a) and (b)), i.e., the cases when metal atoms substituted for one or two C atoms in a pristine graphene lattice. In contrast, the Cu atoms in our experiments exhibited a more complex behavior and were frequently observed at Stone–Wales (SW) defects in graphene (shown in Figs. 3-4 (c–e)). We name the corresponding structures according to the number of atoms making up the carbon rings, including the central Cu atom. For example, the Cu atom shown in Fig. 3-4(c) makes two 6-membered rings and one 7-membered ring with neighboring C atoms, so we call this structure 667.

Cu atoms reknit graphene structure

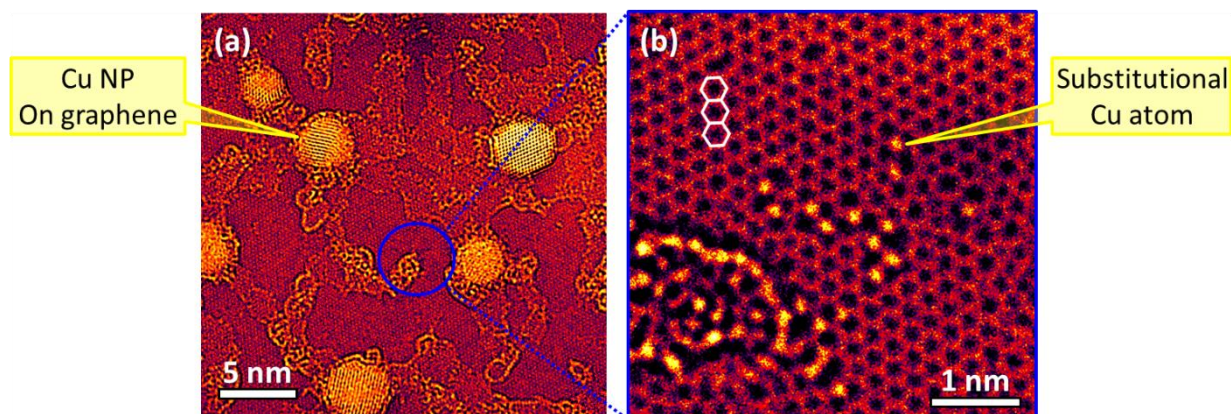


Figure 3-3 Cu atoms embedded in graphene

TEM images taken at (a) low- and (b) high-magnification. Image (b) shows Cu atoms (brighter spots) embedded in graphene. Images were colored to highlight the Cu atoms. White hexagonal lines in (b) indicate the graphene honeycomb lattice.

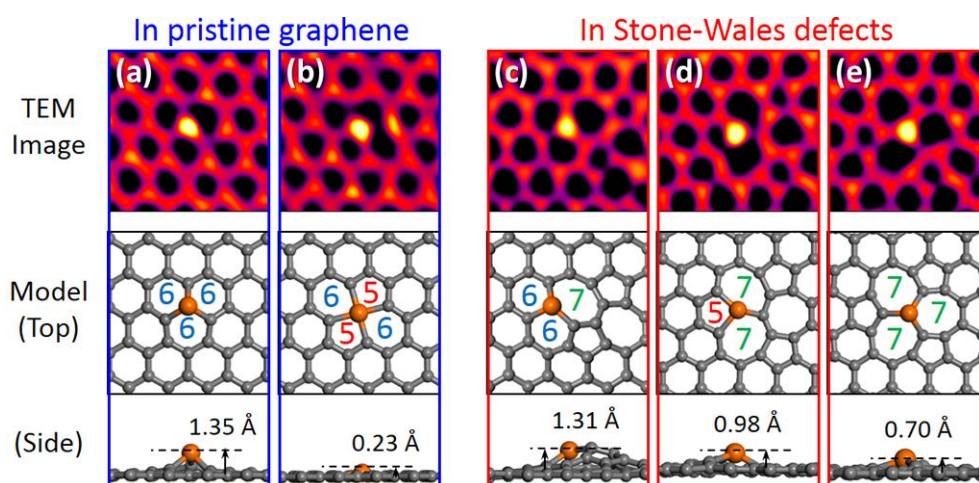


Figure 3-4 Cu sites in graphene

(a–e) Averaged and low-pass filtered TEM images (top row) and corresponding DFT models of Cu sites (top and side views, second and third rows, respectively).

DFT calculations suggest that most Cu-related defects are not planar, except for those containing four-coordinated Cu (Fig. 3-4(b)). Three-coordinated Cu atoms (Figs. 3-4(a) and (c–e)) protrude from the graphene surface because single vacancies are too small to accommodate them. The 577 configuration (Fig. 3-4(d)) has smaller height than the 667 configuration where several C atoms

are displaced out of graphene plane along with Cu. Malola *et al.* [206] claimed that Au preferentially occupies double or larger vacancies to reduce the height; however, we observe no clear correlation between the height and stability (lifetime) of the observed structures. For example, the highly distorted 667 was more frequently observed and had a longer lifetime than the almost planar 577 structure. Krasheninnikov *et al.*[113] found that metal atoms, including Cu and Au, form covalent bonds with the C atoms at the vacancies. The stability primarily depends on the strain around the Cu atoms and the bonding strength between Cu and C; hence, the height of a defect is not a decisive factor.

In addition, Cu atoms physically adsorbed on a pristine graphene surface were rarely observed, because their diffusion barrier is more than 10 times lower than that of substitutional Cu atoms [117]. As already mentioned in Chapters 1 and 2, the energy provided by heating and electron beam irradiation was sufficient to transform Cu atoms embedded in graphene and was too large to observe atoms adsorbed on its surface.

3-3-2 Reconstruction of graphene

Cu substitution resulted in a gradual reconstruction of graphene during the TEM observations. Figures 3-5(a) and (b) show TEM images before and after the reconstruction. It took ~13 min in this case (electron beam current density $j = 1.56 \times 10^7 \text{ e}^-/\text{s} \cdot \text{\AA}^2 = 125 \text{ A/cm}^2$, and temperature $T = 150 \text{ }^\circ\text{C}$). A small misoriented region was created near Cu atoms. It contains pairs of SW defects at a 30° grain boundary (yellow in Fig. 3-5(c)).

Figures 3-6(a) and (b) show TEM images taken before and after the reconstruction taken from another area. Note the broadening of the corresponding spots in the fast Fourier transform (FFT) pattern (cf. insets in Fig. 3-6(b)), which reveals that the reconstruction resulted in an angular disorder due to the formation of 1–3 nm sized grains. We numbered the four grains shown in Fig. 3-6(b) as follows: grain #1 kept its original orientation, but became slightly distorted; #2 and #4 reconstructed and rotated by 18° and 23° from the original, respectively; and #3 rotated while preserving its original honeycomb structure.

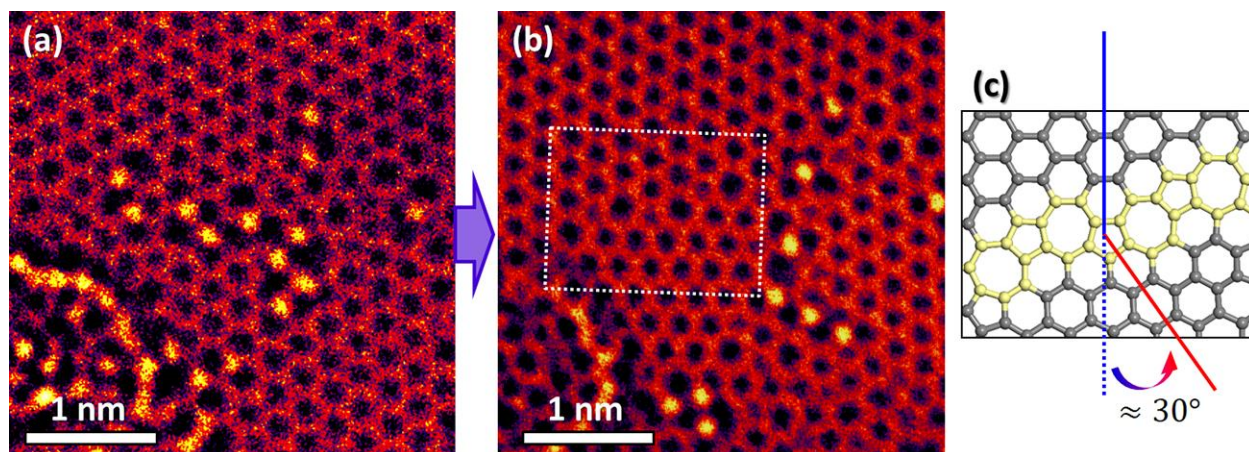


Figure 3-5 Reconstruction of graphene

False-color TEM images taken (a) before and (b) after the reconstruction of graphene. Image (a) is the center area of Fig. 3-3, and image (b) was taken after ~13 min from (a). (c) Model of grain boundary marked by the white box in (b). Stone-Wales defects highlighted in yellow.

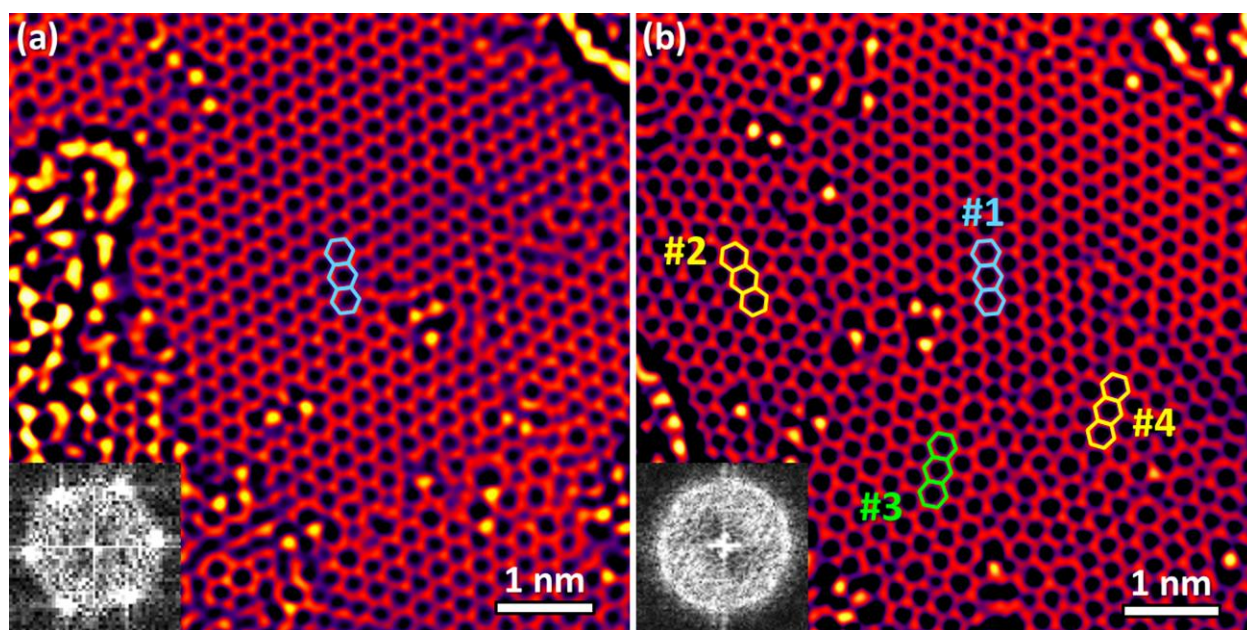


Figure 3-6 Reconstruction of graphene

False-color low-pass filtered TEM images taken (a) before and (b) after the reconstruction. Image (b) was taken ~20 min after (a). Insets in (c) and (d) are FFT patterns.

Chapter 3

Most grains were disrupted by the local strain induced by the contaminants, and reconstructed via repeated rotation of C–C bonds near Cu atoms to minimize the overall strain. In Fig. 3-5(a), hydrocarbon contaminants on the left side of the image were partially graphitized by electron beam irradiation, distorting the underlying graphene lattice. Grain #2 was also covered by hydrocarbons (Fig. 3-6(a)); it reconstructed after their removal by electron irradiation, albeit with a different orientation.

The TEM images shown in Figure 3-7 are selected snapshots between Figs. 3-6(a) and (b), which shows a different type of reconstruction, namely a grain rotation. In contrast to the former reconstruction, the grains kept the original graphene structure during the reconstruction. Grain #3 retained its orientation until a small pore was mended by Cu atoms, and gradually rotated by about 17° owing to the strain from contaminants on the left and defects on the right side. During this process, many SW defects moved via C–C bond rotation and helped fit grain #3 to its neighbors.

Lehtinen *et al.* [207] found that aggregated interstitials in graphene, which leads to a strong local curvature in graphene, are energetically more favorable than isolated ones. The same was true of Cu atoms and SW defects: SW defects were reported to distort graphene [125], [208], and Cu atoms in our experiment tended to combine with them rather than remain isolated. Cu atoms can also distort graphene, thereby promoting both generation of defects and their healing via C–C bond rotation. Such repeated distortion and reconstruction, promoted by Cu atoms and electron irradiation, gradually changed the graphene structure in large area.

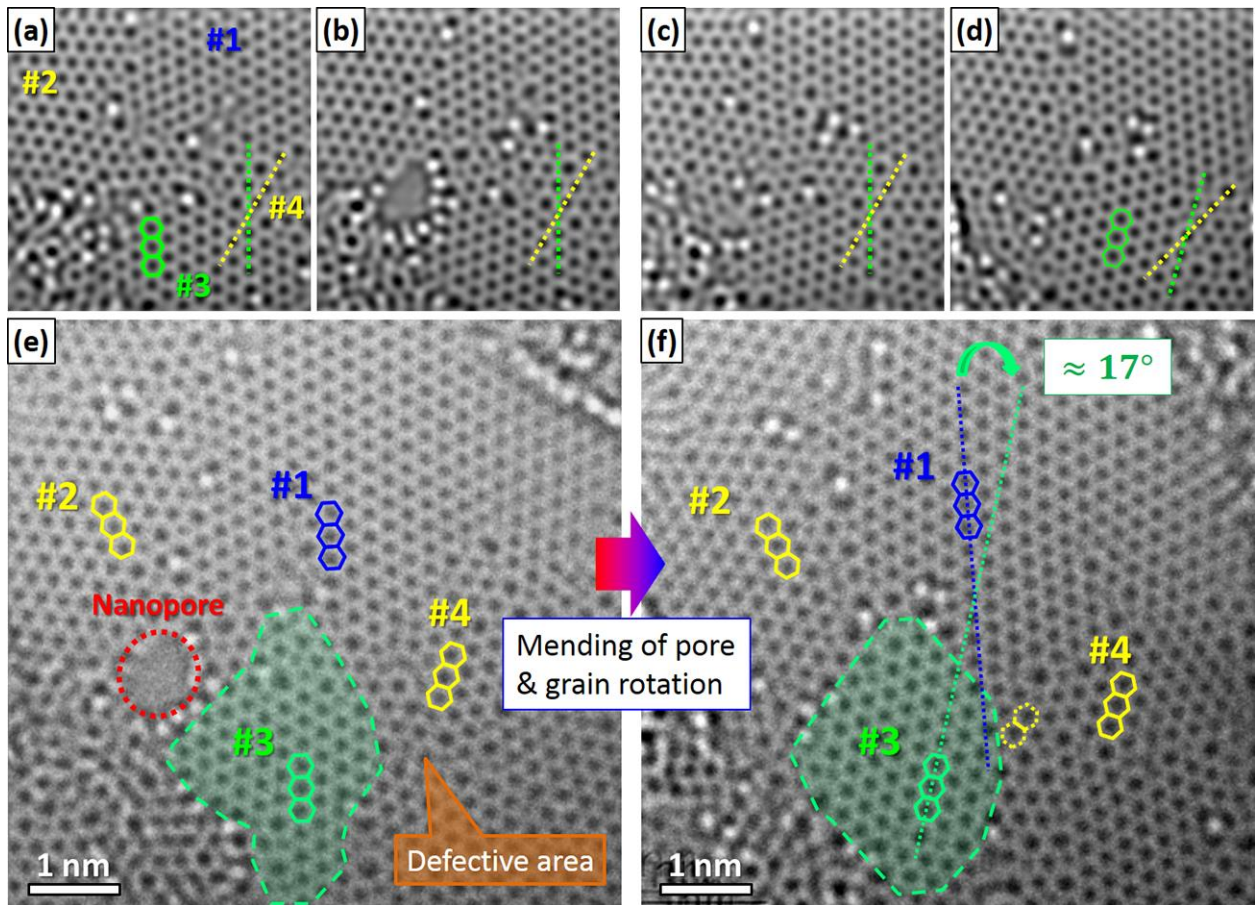


Figure 3-7 Selected snapshots of grain rotation

(a–d) Low-pass filtered TEM images indicate the rotation of grain #3. Images (a–c) show the formation and mending of a nanopore in graphene. (e, f) Unprocessed TEM images corresponding to (b) and (d) with annotations. Green and yellow dotted lines in (a–d) indicate the orientations of grains #3 and #4, respectively. A part of grain #4 had an orientation differing by 30° from that of grain #3, and grain #3 gradually rotated with that part of grain #4.

3-3-3 Transformations promoted by Cu atoms

We analyzed the dynamics and stability of 56 single Cu atoms to elaborate on the graphene transformations mentioned above. Figure 3-8 shows the four typical transformation types: (a–b) and (c–d) are C–C bond rotations #1 and #2. They differ by that in #1 one of the rotating C atoms is attached to a Cu atom, while in #2 the rotating pair is separated from Cu. The third transformation is rotation of a C–Cu bond (e–g), and the fourth is ejection of one C atom (h–i).

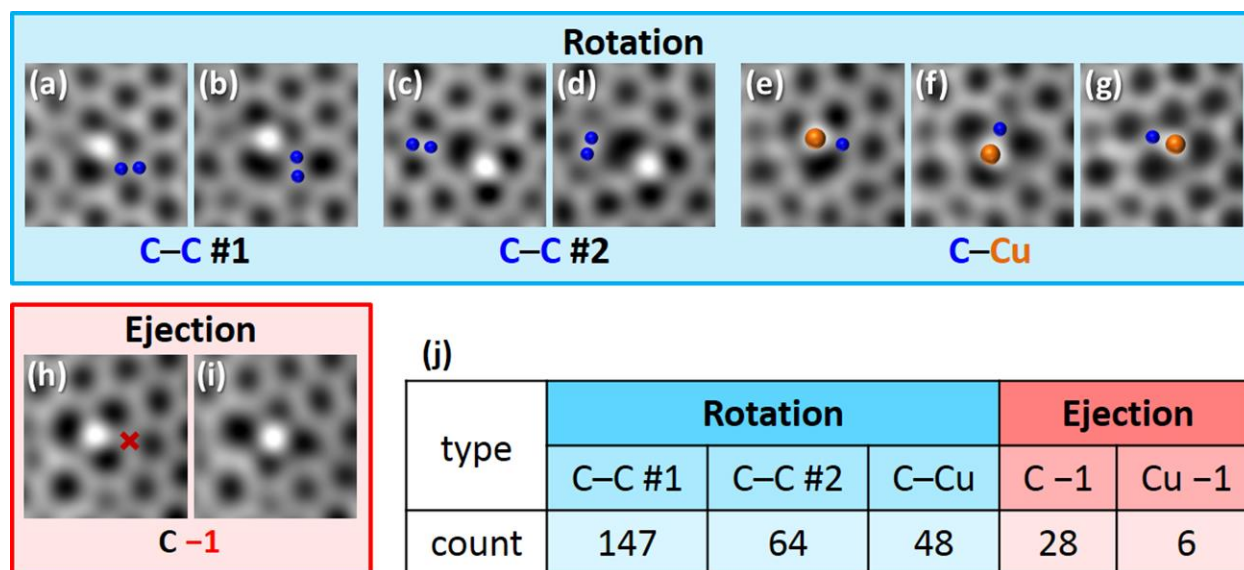


Figure 3-8 TEM images of the typical transformations

(a, b) rotation of C–C bond attached to a Cu atom, (c, d) rotation of C–C bond near a Cu atom, (e–g) rotation of C–Cu bond, and (h, i) ejection of C atom next to Cu. Rotated C and Cu atoms are highlighted as blue and orange balls, respectively. (j) Observation frequency for each transformation (arb. unit).

Figure 3-8(j) summarized the observed frequency of each transformation. The majority of the observed transformations were C–C rotations near the Cu atoms. C–C rotation #1 was most common and occurred reversibly, while C–C rotation #2 was less frequent. We can explain this preference by the number of bonds that break and recombine during each transformation (see Fig. 3-9). Two strong C–C bonds break in process #2 (Fig. 3-9(a)), whereas #1 involves one C–C bond and one weak C–Cu bond (Fig. 3-9(b)). The binding energies of substitutional C and Cu atoms in graphene were calculated as 15.7 and 3.9 eV, respectively. Because each C and Cu atom is bonded with three neighboring C atoms, the energy difference between one C–C bond and one C–Cu bond,

or between rotations #2 and #1, is estimated to be ~ 3.9 eV. This scenario can explain the difference in the relative frequencies of C–C rotations #1 and #2, but does not explain why C–Cu rotation was less frequent. It predicts that C–C #1 and C–Cu rotation should be equally frequent, as they both involve one C–C and one C–Cu bond (Fig. 3-9(a) and (c)). Meanwhile the C–C #1 process was 3 times more common in our observations. Furthermore, C ejections were rather common, despite their expected high energy-barrier, whereas very few Cu ejections were observed. This inconsistency can be explained by electron beam irradiation (discussed in section 3-3-4).

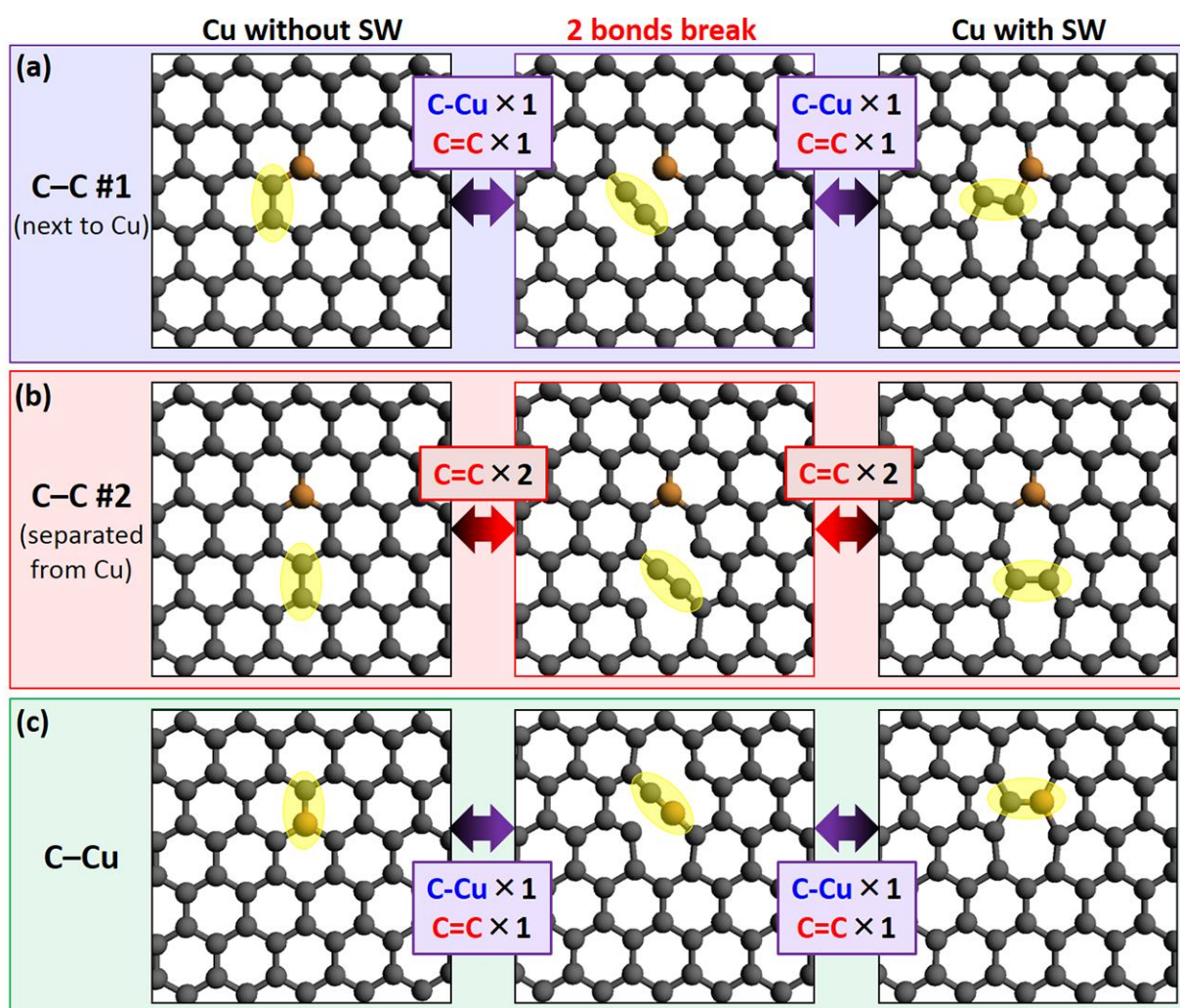


Figure 3-9 Comparison between three types of bond rotations

Schematic atomic model images presenting rotation processes of (a) C–C bond next to Cu (C–C #1), (b) C–C bond separated from Cu (C–C #2), and (c) C–Cu bond. Yellow ellipses highlight the rotating bonds. Two bonds break and recombine during each bond rotation. The binding energy of one C–C bond in graphene is ~ 5.2 eV, while that of one C–Cu bond is ~ 1.3 eV.

According to the experimental results shown above, we performed first-principles DFT calculations to evaluate the activation energy barrier and the total energy change for each transformation. In short, our DFT calculations of the energy barrier do explain why the C–C rotations are promoted by Cu atoms. They agree with the analyzed observation frequency (Fig. 3-8(j)) and stability of each structure and the binding energy estimates mentioned above, although the used models are simple and do not take in account the defect-related lattice distortions over a large area. First, Figures 3-10(a) and (b) show the C–C rotation that converts four 6-membered rings into two SW defects. Fig. 3-10(c) shows the energy diagram of C–C bond rotation *without* Cu atom. The total energy increased by 5.06 eV when a SW defect was created. The top of the barrier corresponds to the transition state with two broken C–C bonds; it is 9.36 eV above the pristine graphene (Fig. 3-10(a)) and 4.30 eV above the SW defect level (Fig. 3-10(b)). These values are consistent with a previous report [112]. The 9.36 eV energy can be easily supplied by an electron beam in a typical TEM operated at 200-300 kV, but not at 80 kV.

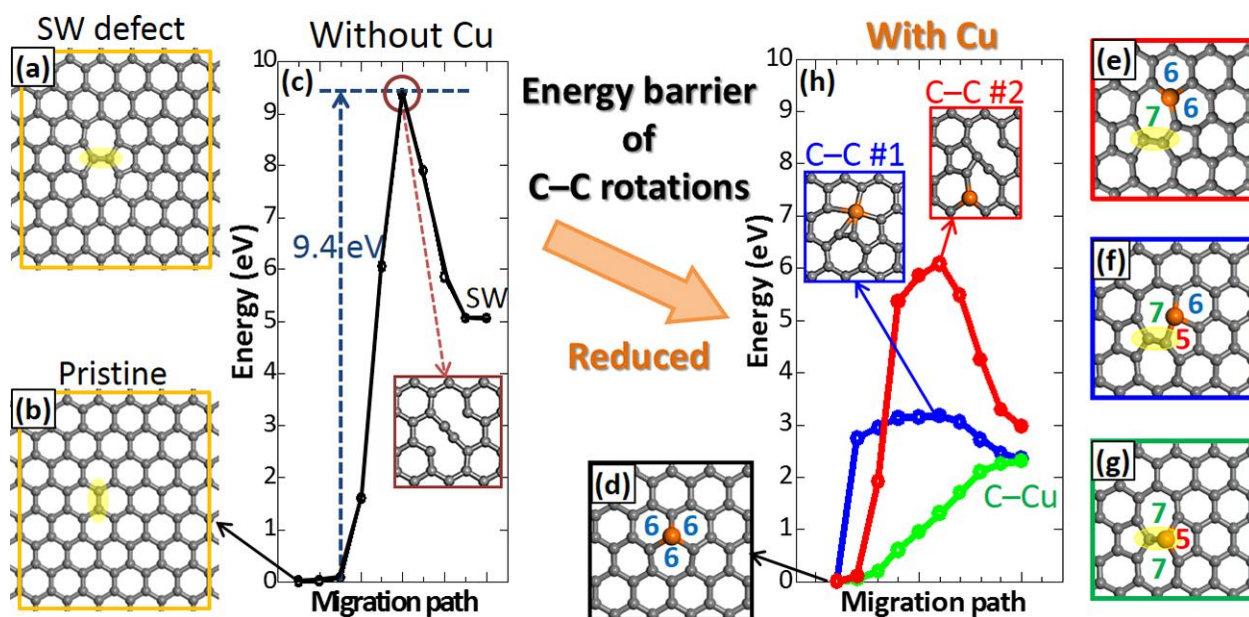


Figure 3-10 Energy required for the bond rotations

(a, b) Atomic models of C–C bond rotation without Cu atoms. Orange frames outline the cells used in DFT calculation, which contain 96 atoms. (c) Energy diagram of transformation between (a) and (b). (d–g) Atomic models of Cu sites in graphene. If the two C atoms highlighted by yellow ellipses are rotated, the model of Cu atoms embedded in SW defects (e–g) will become pristine structure (d). (h) Energy diagrams of transformations between (d) and (e), (f) or (g). Insets show models of transition states.

Cu atoms reknit graphene structure

Then we calculated C–C bond rotation *with* Cu atoms (Figure 3-10(d–h)). Replacing one C atom with a Cu atom in these figures results in the 666, 667, 567 and 577 defects as shown in Figs. 3-10(d–g), respectively. We found that the energy barrier of C–C rotations with Cu atom (Fig. 3-10(h)) was significantly reduced from that in pristine graphene (Fig. 3-10(c)). The C–C rotation #1 was most frequently observed, because the energy barrier was reduced to 3.18 eV, and the energy required to return to the 666 structure (Fig. 3-10(d)) was only 0.84 eV. This reduction came from the low C–Cu binding energy and from the partial passivation of dangling C atoms by Cu atom (see inset in Fig. 3-10(h)).

The stability of each structure depends on the energy barrier height rather than the total energy difference. For example, although the SW defect is 5.06 eV less stable than pristine graphene, once it is created, the energy barrier of 4.30 eV prevents its relaxation from SW defect to pristine graphene. The 577 structure (Fig. 3-10(g)) has a lower total energy than the 667 structure (Fig. 3-10(e)); however, there is no energy barrier between the 577 and 666 structures (Fig. 3-10(d)), as shown in Fig. 3-10(h); therefore, it will soon transform into 666 (the pristine structure without SW defects). The 577 structure can also be regarded as a transition state of diffusion of Cu atoms. The Cu atom in the 666 structure will exchange positions with the neighboring C atom by the 180° C–Cu rotation. The corresponding energy barrier is 2.32 eV (energy difference between the 577 and 666 states), which is similar to the value of 2.2 eV for Au atom diffusion in graphene [209].

In short, DFT calculations reveal that the energy barrier of C–C bond rotation was significantly reduced by the presence of Cu atoms. The relevant experimental results are discussed above (Figs. 3-8 and 3-9). Furthermore, a Cu atom at a vertex of the pentagon induces a large stress in graphene and therefore is less stable than in the other configurations, despite the low total energy of its optimized structure.

The latter factor appeared in our experimental observations as the defect lifetime; that is, the time interval between two arbitrary transformations. Figure 3-11 shows a characteristic example of the analysis procedure. At high beam current densities (Figs. 3-11(i) and (ii)), the lifetime of all structures were almost the same (a few seconds). However, a difference appeared at lower beam current densities (see Fig. 3-11(iii)). Defects involving pentagon, such as 577 and 568, had approximately half the lifetime of the 667 or 677 structures.

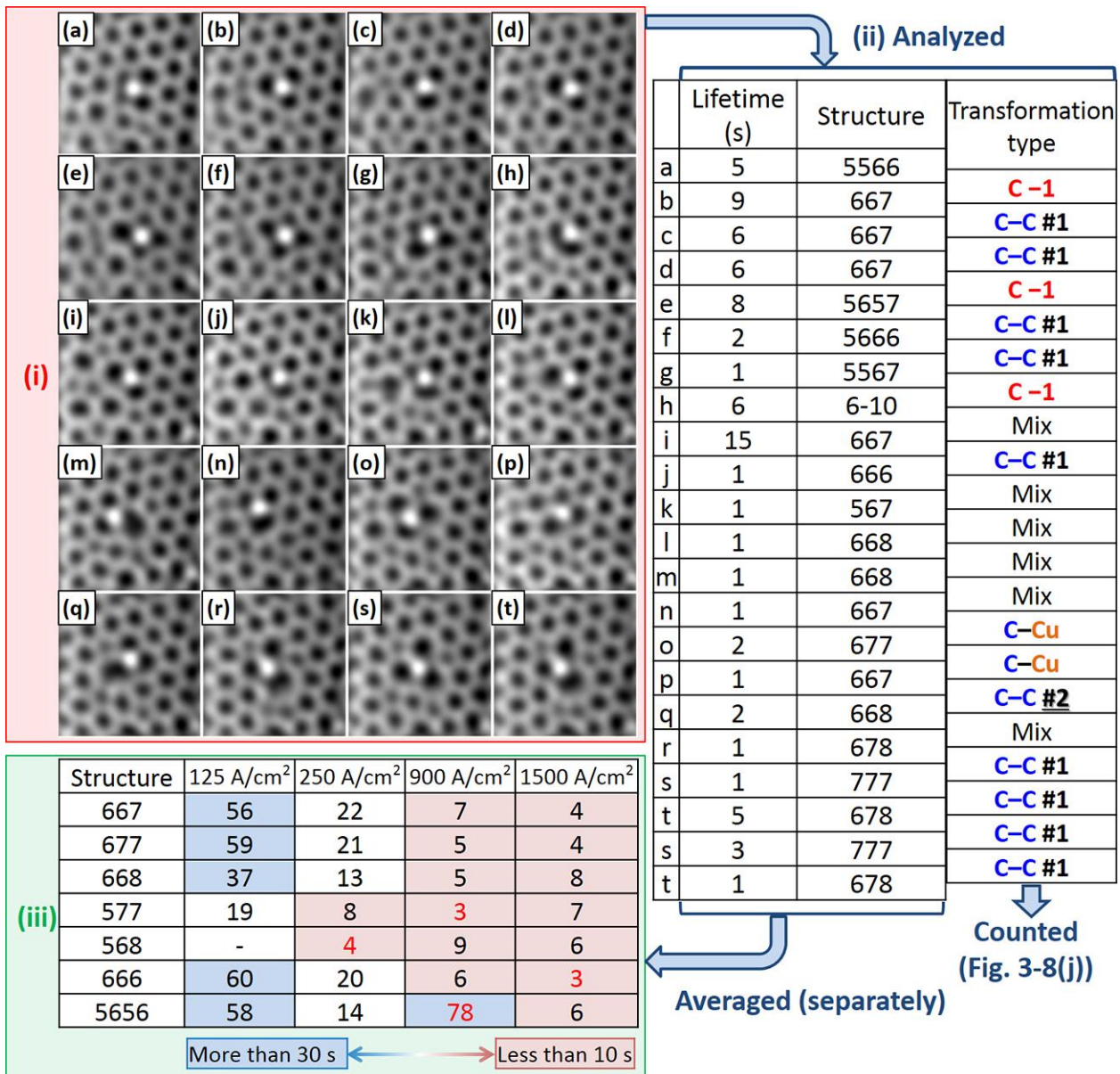


Figure 3-11 Analysis and averaged lifetimes of typical structures

(i), (ii) Specific example of the analysis at 150 °C and electron beam current density $j = 900 \text{ A/cm}^2$. (i, a–t) Low-pass filtered TEM images. The table in (ii) shows actual lifetimes and transformation types corresponding to the images (i). “Mix” in the right column means that several transformations occurred within 1 s. (iii) Averaged lifetimes of typical structures at 150 °C with a variety of current density j : focusing the electron beam reduced the lifetime. At low beam current densities, 577 and 568 disappeared twice faster than other structures due to the large stress from the pentagon they contained. Red numbers correspond to observations that were seen only once in our experiments.

3-3-4 Driving force of the transformations

In this section, we discuss two driving forces: *in situ* heating and electron irradiation. C–C bond rotations occurred within 5 min in our experiment, which had a temporal resolution of 1s. We estimated the energy required to rotate the C–C bond at 3.2 eV, which is sufficient to cause SW defect formation by C–C rotation #1 and relaxation by C–C rotation #2, as shown in Fig. 3-10(h). We then calculated the time required for the next rotation via thermal activation [139]: the C–C bond rotation takes $\sim 10^{15}$ s at 300 °C, with an attempt frequency of 5×10^{12} s⁻¹ given by the G-mode vibration of graphene [210]. This calculation suggests that most transformations could not be induced by thermal activation (except for the relaxation of SW defects via C–C rotation #1), and were likely promoted by electron irradiation. This conclusion is supported by our observations that graphene structure remained unchanged in weakly irradiated sample areas.

As discussed in sections 1-1-2 and 2-2, a large amount of energy can be transferred from incident electrons to C atoms, while the energy transfer to Cu atoms is small: E_{\max} is 15.75 eV for C and 2.97 eV for Cu at 80 keV incident electron beam energy. The energy transfer model can explain why C–C bond rotation and C atom ejection were more frequently observed than C–Cu bond rotation and Cu ejection. The energy transferred to Cu atoms cannot exceed 2.97 eV; hence, the observed transformations arose mainly via excitation of C atoms. Electron irradiation has less effect on Cu; thus, Cu atoms moved less frequently than C atoms. Therefore, we rarely observed Cu atom ejections from the graphene lattice, although the binding energy of a Cu atom in a single vacancy is 4–5 times smaller than that of a C atom. The ejected C and Cu atoms likely moved too fast to be observed by TEM and were trapped by other vacancies or contaminants in graphene.

Figure 3-12 shows the averaged lifetimes, for all types of structures and transformations, at several electron beam current densities (respective lifetime values of typical structures are shown in Fig. 3-11(iii)). The green symbols correspond to the experimental values measured at 150 °C, while the blue and red squares represent the calculated values, assuming the energy transferred to C is in the range of 3–10 eV. The experimental values are in between the calculated values, and both lifetimes are inversely proportional to electron beam current density j . For $j = 125$ A/cm², transformations occurred within a few seconds in defective areas, whereas stable structures such as 667, 666, 677 and 5656 in a relatively clean graphene often survived for more than 2 min under electron beam irradiation.

In addition, the temperature effect on the lifetime t became significant at lower current density j , although it was smaller than the electron irradiation effect. In contrast to the energy transferred from electron beam, the thermal activation energy affects C and Cu equally; hence, increasing the temperature reduced the lifetime of every Cu-graphene configuration.

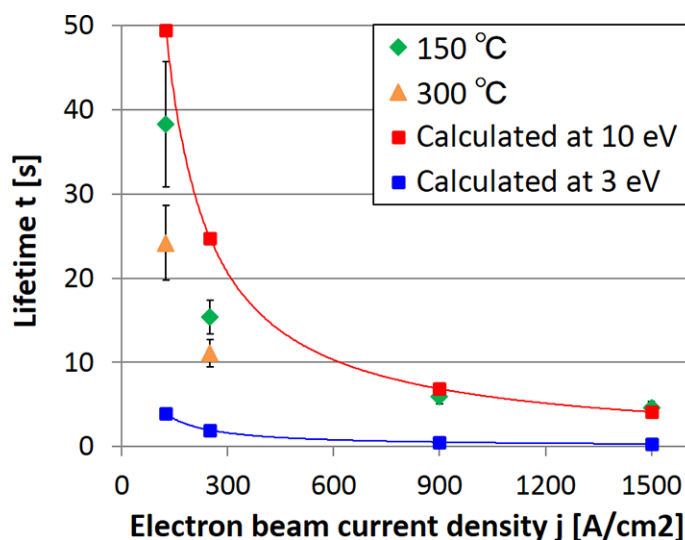


Figure 3-12 Lifetime under electron irradiation

The observed lifetimes at 150 °C (green) and 300 °C (orange) were averaged and plotted as a function of the electron beam current density j . The red and blue symbols show the values calculated from the scattering cross section σ at $E_{\text{t}} > E_{\text{B}} = 10$ or 3 eV, as discussed in section 2-2. The defect lifetime t is inversely proportional to the product of scattering cross section σ and current density j ($t = 1/\sigma j$).

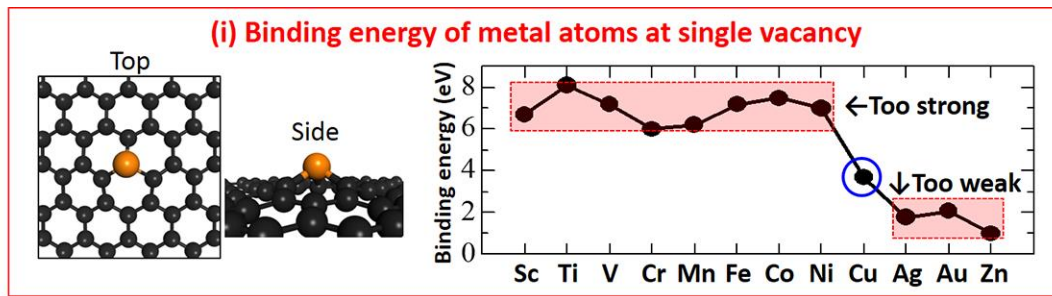
In summary, we discuss two driving forces, and conclude that the energy transferred to C atoms from high-energy incident electrons promotes all the transformations described in the previous sections. The occurrence frequency of the transformation differed according to (1) their energy barriers and (2) chemical elements. Regarding (2), the observed transformations arose mainly via excitation of C atoms; therefore the transformations only involving C atoms (such as C–C bond rotations) were more frequently observed than the transformations involving Cu atoms (such as C–Cu bond rotations). Transformations occurred within a few seconds in defective areas, whereas stable structures in clean graphene survived for a longer time under the same irradiation conditions. Therefore, we conclude that Cu atoms promote C–C rotation when they are surrounded by defects, but not when reconstruction of the graphene is complete.

3-3-5 Uniqueness of Cu compared with other transition metals

Many metals, including Cr, Ti, Pd, Ni and Al, were experimentally reported to etch graphene [155], and a similar activity was theoretically predicted for Fe and Co [211]. Cu atoms, however, promoted graphene reconstruction rather than etching in our experiment. Even when small pores were created by irradiation, Cu atoms attached their edges to prevent expansion of the pores and mended them by trapping C atoms diffusing around (e.g. Fig. 3-7). We have not observed such effects for Pt under similar experimental conditions, instead, Pt atoms etched graphene edges to widen the pores (see Chapter 4). As described in section 1-2-1, electron beam irradiation can induce structural transformations at single or double vacancies in graphene without Cu atoms; however, these transformations occur within atomically small regions.

We believe this unique ability of Cu originates from its moderate binding energy with C atoms in graphene. The graph in Figure 3-13(i) shows the values of binding energy taken from literature [114] (almost the same values were reported in [113], as shown in Fig. 2-10). The binding energy of Cu at the single vacancy is 3.7 eV (our calculated value was 3.9 eV), whereas its values for other transition metals are 6–8 eV. These metal atoms strongly bind with C atoms and strain the graphene lattice, which may reduce the displacement threshold energy by electron beam irradiation. This effect should be much smaller for Cu, Ag, Au and Zn atoms (binding energy 1–3 eV). However, these metal atoms, except for Cu, may move away rather than reconstruct graphene, because their binding energy is too small to keep them in graphene. To confirm this prediction, we observed graphene with Pt, Cu, and Au atoms (see Chapter 4).

Furthermore, we compared the energy difference ΔE between the structures with and without SW defects. Tables in Figures 3-13(ii) and (iii) show ΔE for Cu and other metals (Fe, Cr, Ni, and Co). We found that their ΔE are ~ 1 eV higher than for the Cu atoms in the same models. This result suggest that, compared to Fe, Cr, and Ni, Cu atoms are more stable near SW defects, and thereby promote C–C bond rotations and unique reconstructions.



(ii) Cu atom at single vacancy with and without SW defect

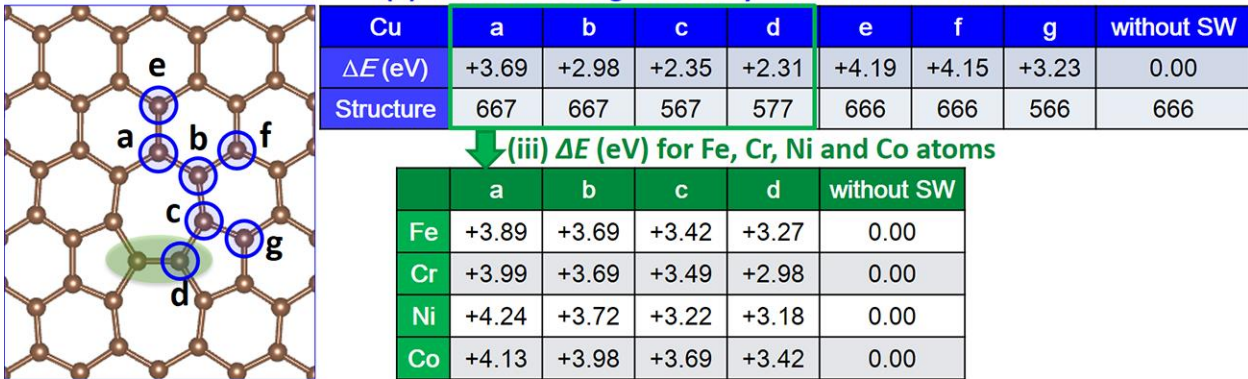


Figure 3-13 Binding energy between metal and C atoms

(i) Binding energy of metal atoms at a single vacancy. The graph was redrawn from Ref. [114]. (ii) The energy difference ΔE between the substitutional Cu structures with and without SW defects. (iii) ΔE data for Fe, Cr, Ni and Co, which are ~ 1 eV higher than for Cu shown in (ii).

3-4 Summary

We directly observed atomic-scale transformations of Cu-doped graphene by an aberration-corrected TEM. Our observations suggest that Cu atoms tend to combine with SW defects and preferentially replace C atoms in defective graphene areas. They also modify graphene by promoting C–C bond rotation, formation and mending of nanopores, and rotation of grains mediated by contaminants and lattice defects. Cu atoms and SW defects form grain boundaries between the reconstructed and original grains. All these transformations were assisted by electron irradiation, which affected C atoms much more than Cu atoms because of the higher energy transferred to them from the incident electron beam. Thermal effects need a further study, and our results reveal that Cu atoms are stable in graphene sheets up to 300 °C. We combined experiment with DFT calculations to investigate the stability of Cu atoms embedded in graphene and the activation energy barriers for the experimentally observed transformations. Our results reveal that individual Cu atoms can catalyze reconstruction of carbon nanostructures and suggest that Cu-doped graphene may find applications in nanoelectronic devices.

Chapter 4

Metal-mediated mending and etching of graphene edges

Metal atoms at graphene edges are important because they can modify the structure and properties of graphene; however, there are very few reports on their direct observation. As described in Chapter 3, substitutional Cu atoms can promote unique reconstruction of single-layer graphene. Here we present different behaviors of Cu, Pt and Au atoms at graphene edges. We have found opposite effects of Cu and Pt atoms on graphene edges: Cu atoms mend graphene edges, but Pt atoms etch them. Au atoms promoted neither etching nor mending because of the weak binding energy to C atoms in graphene. These transformations were assisted by electron irradiation.

4-1 Introduction

Functionalization by metal atoms has been predicted to improve the electronic, magnetic, and catalytic properties of graphene [27], [29], [151], [152], [212], [213]; however, it can also result in etching. Ramasse *et al.* reported that Cr, Ti, Pd, Ni and Al atoms etched graphene in vacuum, even at room temperature [155]. While this phenomena may be detrimental for the fabrication of large-area graphene devices, it offers a promising method for producing graphene nanoribbons, as metal nanoparticles can etch graphene along a specific crystallographic direction [37], [145]–[148]. It is therefore essential to visualize the interaction of graphene with different chemical elements.

Aberration-corrected TEM enables imaging the structures and dynamics at the atomic scale in real time. As described in Chapters 1–3, a relatively low accelerating voltage of 80 kV induces little knock-on damage in graphene; however, it is sufficiently high to modify graphene edge structures (the knock-on threshold at graphene edge is ~50 kV [214]). There are many electron microscopy reports on the reconstruction of pure graphene edges (without metal atoms) [106], [179], but very few reports on the reconstruction with metal atoms. Although Au [153] and Fe [154] atoms were observed at graphene edges and electron irradiation resulted in the removal or addition of a few C atoms around the impurity atoms, the edge structure did not change significantly.

Since we found that substitutional Cu atoms promoted large-area reconstruction of bulk graphene via repeated C–C bond rotations (described in Chapter 3), we further studied on Cu atoms at graphene edges, and compared their behavior with Pt and Au. Our results reveal that Cu atoms mend graphene edges, Pt atoms etch them, while Au atoms move away rather than reconstruct graphene lattice.

4-2 Methods

Experimental details are described in Chapters 2 and 3. Single-layer graphene was transferred onto an *in situ* heating chip (E-chips for AduroTM, Protochips). Metals were then deposited on graphene using an ion beam etching system (PECS, Gatan) for Cu, DC plasma sputtering system (JFC-1600, JEOL) for Pt and electron beam deposition system (RDEB-1206K, R-DEC) for Au. We annealed the samples in the TEM column ($\sim 10^{-5}$ Pa) to remove the contamination. The annealing temperature was set at 300 °C or lower.

The microscope (JEM-ARM200F, JEOL) was operated at 80 kV. First, we applied a relatively high electron beam current density j to create small pores in graphene. Then we observed Cu atoms at the pore edges at 150 or 300 °C and $j = 63\text{--}1000$ A/cm². The electron density strongly affected the dynamics of C atoms at graphene edges, while the effect of temperature was less pronounced. Pt atoms were observed at 300 °C and $j = 250$ A/cm². Under these conditions, the C configuration around Pt changed every few seconds. All the reported TEM images were taken from movies and were processed as follows: frames were aligned to compensate for sample drift, and then averaged and low-pass filtered to improve the signal-to-noise ratio.

4-3 Results

Figures 4-1(a) and (b) show TEM images and models indicating the typical sites for Cu and Pt atoms at graphene edges. These images were taken under overfocus conditions to highlight the metal atoms. The Cu/C and Pt/C signal ratios were calculated as 1.92 and 3.15, respectively (see section 2-1-3 in Chapter 2). Our observations revealed that Cu atoms adsorbed on the edge surface, while Pt atoms replaced C atoms inside the edges. As shown in Fig. 4-1(c), we classify the sites according to the number of bonds with graphene edge: “surface” has two metal-C bonds, while “inside” corresponds to three bonds. Approximately 89% of Cu atoms were observed at the surface, while ~ 55% of Pt atoms remained inside graphene.

Figure 4-1(c) shows four configurations of an impurity atom at the surface: pentagon and hexagon structures at an armchair edge, and tetragon and hexagon structures at a zigzag edge. The migration barriers of metal atoms at zigzag edges were smaller than those at armchair edges (0.14 and 1.28 eV, respectively, for Au [153]); hence the tetragon structure at the zigzag edge was less stable and changed within a few seconds. When there was a vacancy at the edge, metal atoms adsorbed there and formed hexagon structures. In our observations, metal atoms migrated to intersections or steps of the edges, but not to flat edges. Cu atoms were frequently observed in pentagon structures at the edge intersections, and were stable for ~1–2 min under electron irradiation.

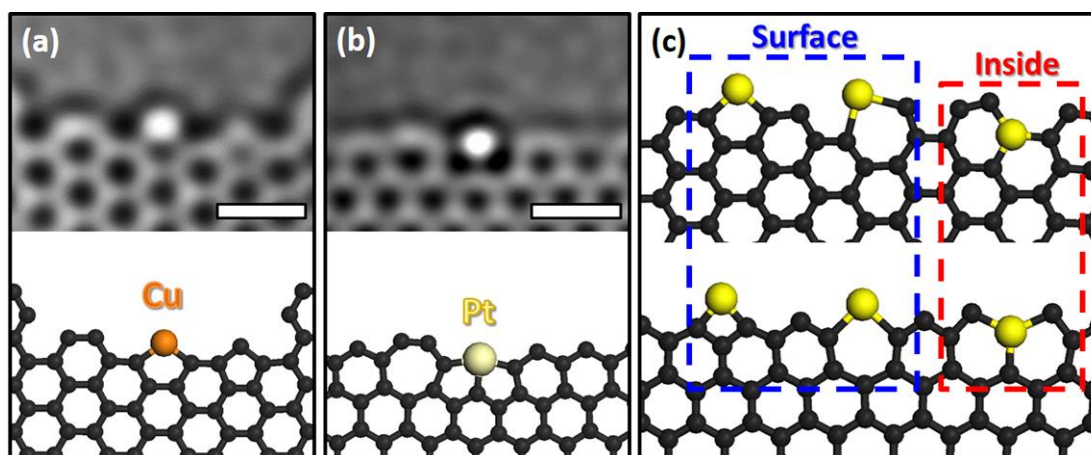


Figure 4-1 Different configurations of Cu and Pt atoms

TEM images and schematic atomic models of (a) Cu and (b) Pt. Scale bars: 0.5 nm. (c) Schematic atomic models of metal atoms at graphene edges (armchair and zigzag, the top and bottom rows, respectively).

Figure 4-2 consists of images that elaborate two different phenomena: (i) mending and (ii) etching. Cu atoms mediated the former, while Pt atoms mediated the latter. For each case, all the TEM images were taken from a same movie. Figures 4-2(a) and (b) (for both (i) and (ii)) are TEM images taken before and after the reactions, respectively, and TEM images and models of (c–g) elaborate each process.

At first, we describe Cu-mediated mending of graphene edge under electron irradiation (Fig. 4-2(i)). As discussed in Chapter 3, substitutional Cu atoms can promote rotations of C–C bonds in graphene, which convert pentagon-heptagon pairs (SW defects) into hexagons. Such rotations also occurred around Cu atoms at the edge (Figs. 4-2(i, c–d)), and triggered further rotations (Fig. 4-2(i, e)). This behavior was also documented for pure graphene edges, where one C–C bond rotation strongly correlated with nearby edge structure [179]. Stable Cu atoms then trapped additional C atoms (Fig. 4-2(i, f)), which were presumably etched by electron beam from the nearby edges or amorphous carbon contamination and diffused along the edge. Cu atoms weakly bonded with C atoms could easily reknit the additional C atoms into graphene (Fig. 4-2(i, g)). The C–C bond rotations (Figs. 4-2(i, c–e)) occurred before and after the trapping of additional C atoms (Fig. 4-2(i, f)). Cu-mediated mending occurred at both 150 and 300 °C. Cu mediated mending occurred at both 150 and 300 °C, and we chose the 150 °C data for Fig. 4-2 because the 300 °C migration was too fast (further details are given in Appendix Figs. A-11 to A-13).

Second, we describe Pt-mediated etching of graphene edge under electron irradiation. Figure 4-2(ii) was recorded at 300 °C for ~6 min. Pt atoms moved into a vacancy (Figs. 4-2(ii, c–d)), which was too small for accommodating a Pt atom, and hence the nearby C atoms were pushed aside. Compared with Cu atoms, Pt atoms were less mobile (heavy Pt atoms less affected by electron irradiation, as described in Chapter 2), and kept the configuration shown in Figs. 4-2(ii, f–g) for more than 20 s. However, they strained the edge, and C atoms that were not directly bonded with Pt were etched away by electron irradiation. Sputtered C atoms diffused along the edge, but continuous electron irradiation moved them outside the view soon. After that the Pt atom moved into the created vacancies, repeating the etching process in a new location.

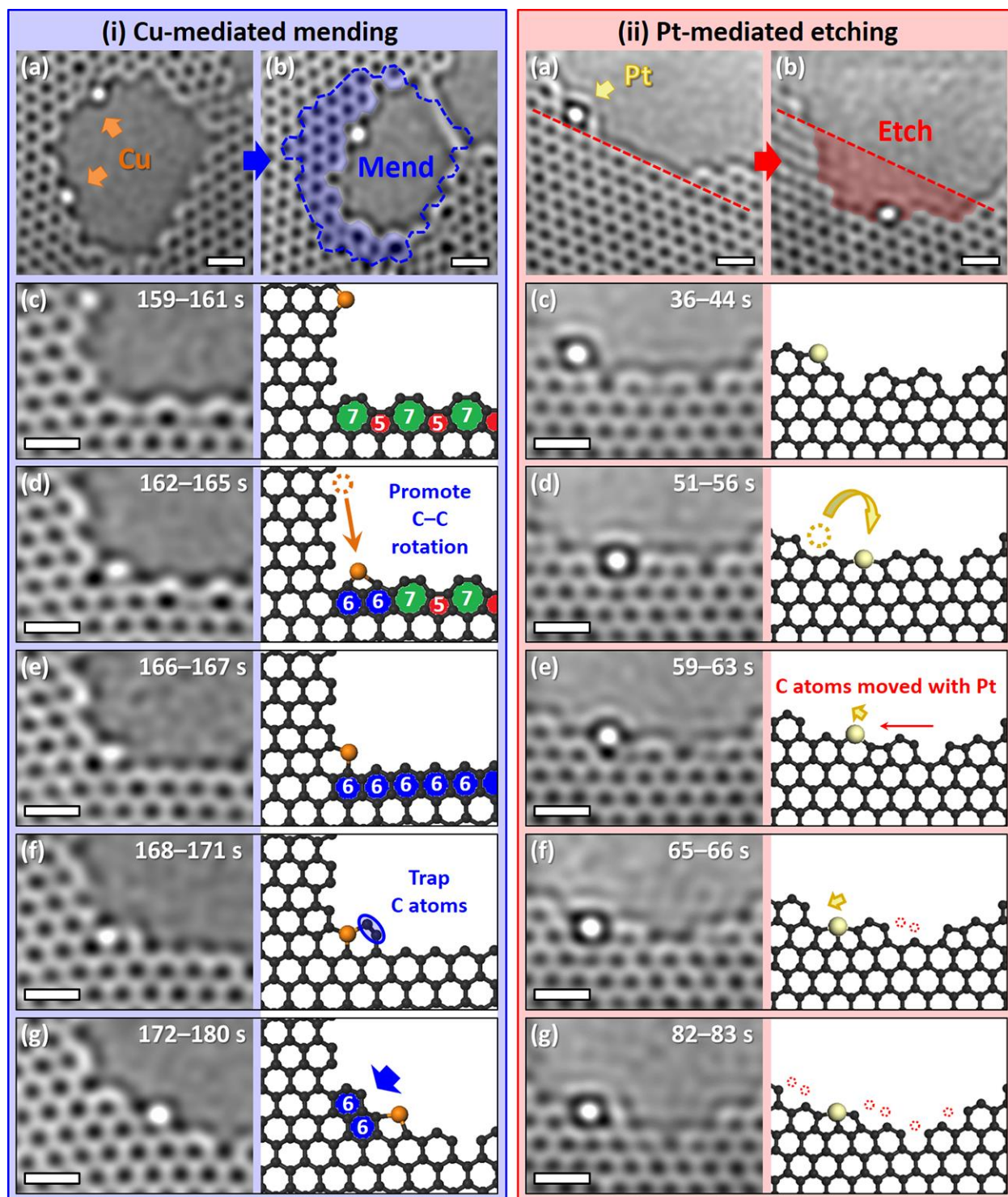


Figure 4-2 (i) Cu-mediated mending and (ii) Pt-mediated etching

TEM images taken (a) before and (b) after each reaction (it took ~3 min for (i) and ~6 min for (ii)). Image (a) corresponds to $t = 0$ s for each case. (c–g) TEM images and schematic atomic models showing (i) mending or (ii) etching of graphene edge. Scale bars: 0.5 nm.

Au atoms could be observed only at room temperature, and they promoted neither etching nor mending. When heated at 150 or 300 °C, Au aggregated to form nanoparticles and individual atoms could not be imaged in our experiments. Wang *et al.* also reported diffusion of individual Au atoms along graphene edges and found that it did not significantly affect the edge structure [153].

4-4 Discussions

4-4-1 Binding energy of metal-carbon bond

The different behaviors of Cu, Pt and Au atoms at graphene edges can be explained by the binding energies to C. Substitutional metal impurities in graphene form covalent bonds with C atoms, and the binding energy of single Pt–C, Cu–C and Au–C bonds is approximately 2.6, 1.2 and 0.7 eV, respectively [113], [114], [215]–[217]. Because of their large atomic radii, the substituted atoms strain the graphene edge and shift out of the graphene plane. This strain or defect reduces the knock-on threshold [110] and thereby promotes etching in the case of Pt. It was reported that the strain caused by dislocations extends [125], hence we suppose that the strain caused by substitutional metal atoms also extends far enough to affect distant C atoms (Fig. 4-2(ii, g)). In the case of Cu, the binding energy to C is smaller, and the strain can be reduced via C–C rotations or Cu–C displacements. These mechanisms do not work for Au because the Au–C bonds are too weak to keep Au at graphene edges.

4-4-2 Effects of heating and irradiation

Heating to 150 or 300 °C had a minor effect on graphene edges – their transformations require a few eV, while thermal energy is only 0.036 eV and 0.049 eV, respectively. However, the energy requirements for migration of etched atoms are much lower, which is why C movements at 300 °C were relatively fast in this study. We did not observe structural changes in weakly irradiated areas; therefore, we conclude that the reported etching and mending phenomena are promoted by electron irradiation. The applied accelerating voltage of 80 kV transfers up to 15.75, 2.97, 0.97 and 0.96 eV to C, Cu, Pt and Au atoms, respectively, that is, electron irradiation affects mostly the light C atoms.

4-5 Summary

As described in Chapter 3, we found that substitutional Cu atoms can promote unique reconstruction of graphene, and expected different tendency for other metals. In this chapter, we report a direct visualization of dynamics of Cu and Pt atoms at graphene edges by TEM. Cu and Pt atoms formed different configurations in graphene and induced opposite effects: mending and etching, respectively. These transformations were promoted by electron irradiation, while the effect of heating between 150 and 300 °C was less pronounced. Our results suggest that deposition of different metals on graphene edges, combined with electron irradiation, allows us to control the edge structure.

Chapter 5

Metal-terminated carbynes on graphene

In this chapter, we report a direct observation of carbynes (monoatomic linear carbon chains) by *in situ* TEM. Cu or Pt atoms in graphene (described in Chapters 3 and 4) served as nucleation sites for carbyne formation. Migration of C adatoms on graphene was promoted by electron irradiation, and the carbon atoms were trapped by metal atoms. Carbynes were formed both at Cu and Pt atoms, albeit with different observed frequency and stability. Here we focus on the difference between Cu- and Pt-terminated carbynes.

Note that a part of the experiment on Pt-terminated carbyne was performed when I was a master's degree student. As a monoatomic carbyne chains are an attractive material, we continued to study carbynes; TEM experiments and image simulations were further performed after the completion of master's course, and revealed that carbynes can also grow on substitutional Cu atoms in graphene.

5-1 Introduction

Carbyne is one of the many allotropes of carbon. It is a one-dimensional (1D) structure, composed of a linear chain of *sp*-hybridized C atoms. There are two possible structures of the linear carbon chain: cumulene ($=C=C=$)_n and polyynes ($-C\equiv C-$)_n, while alkane (C_nH_{2n+2}) and polyacetylene (CH)_n are zigzag chains with bonding angles of 120° and 109.5°, respectively. In our experiment, no zigzag chains were observed, and thus the observed structures should be either cumulene or polyynes. They may co-exist, as they have similar dissociation energies. Theoretical studies predict that carbynes have unique properties that rival those of graphene and carbon nanotube (CNT): twice the tensile stiffness of graphene and CNT, a tension-induced increase in the electronic band gap, high stability at room temperature, and so on [218]. However, these properties have not yet been proven experimentally because of the difficulties encountered in production and observation of carbyne. Mass production is a key factor in expanding carbyne research. CNTs, for example, have become widely used since their mass production was made possible by chemical vapor deposition [88], [219], [220].

Many carbyne synthesis methods have been reported. For example, finite-length carbon chains have been chemically synthesized in solution [221], [222], but it is difficult to determine their exact structures and properties only by spectroscopic analysis. Some researchers synthesized carbynes and observed their atomic structure by *in situ* TEM [97], [129]–[131]. They etched the graphene sheets or CNTs by the electron beam inside a TEM setup. This top-down approach is available for fundamental studies of the atomic structure of carbyne, but it is not suitable for applications.

We have demonstrated a new approach to produce carbynes using Cu or Pt atoms as nucleation sites. Aberration-corrected TEM enabled us to both produce carbynes and observe their atomic structures. In this study, graphene acted as a support membrane, an ultimate thin film for the detection of carbynes by TEM. We observed carbynes only on clean graphene surface, as it contributed the lowest background required to detect weak carbyne signals; we could not unambiguously detect carbyne on defective or on contaminated graphene.

5-2 Methods

All the details about sample preparation method are described in Chapters 2 and 3. Single-layer graphene was transferred onto an *in situ* heating chip (E-chips for AduroTM, Protochips). Metals were then deposited on graphene using an ion beam etching system (PECS, Gatan) for Cu and DC plasma sputtering system (JFC-1600, JEOL) for Pt. The samples were annealed in the TEM column ($\sim 10^{-5}$ Pa) to reduce the contamination.

An aberration-corrected TEM (JEM-ARM200F, JEOL) was operated at 80 kV. TEM movies were acquired at a speed of 1 frame/s. The annealing temperature was set at 150 °C for Cu because Cu atoms and nanoparticles started to evaporate at ~ 300 °C. Pt was stable at higher temperatures (~ 800 °C), and therefore we examined the temperature effect on carbyne formation using Pt atoms.

5-3 Results and discussion

5-3-1 Formation and dynamics of carbyne

Figure 5-1 shows the formation of a carbyne chain with Pt atoms observed at 400 °C. Carbon chains were observed even at room temperature, but they immediately collapsed when magnified (that is, irradiated by a focused electron beam). This presumably occurred due to the chemical etching by residual oxygen or hydrocarbon contamination under electron beam irradiation. As the temperature was raised towards 400 °C, carbynes survived for a longer time (a few minutes). Above 600 °C, Pt and C atoms moved rapidly and carbyne formation was not observed. Therefore, all experimental results described here were obtained at 400 °C for Pt.

In Figure 5-1 three Pt atoms captured some C atoms, resulting in the formation of a C-shaped chain (Fig. 5-1(i, b)). The chain bent significantly (both ends are in contact) and fluctuated a little, but remained stable for about 1.5 min. Pt atoms could move around freely until carbyne suddenly turned into a linear chain (Figs. 5-1(i, c–e)). Both ends of the chain were terminated by Pt atoms, and the chain remained motionless for more than 20 s. The atomic structures described above are shown in Fig. 5-1(i, f).

Figure 5-1(ii, a) shows a TEM image of a straight carbyne after averaging 5 snapshots of the movie. To separate the signals of chain structures and graphene sheet, we applied a Fourier filter to remove the graphene lattice signal (Fig. 5-1(ii, b)). From these experimental images, the distance between the Pt atoms at both ends was measured as 1.5 nm. Each C–C bond length is 1.2–1.3 Å, which falls between the bond lengths of cumulene and polyene. Given the C–C bond length, 1.5 nm carbyne corresponds to a structure comprising 11 C atoms and 2 Pt atoms (Fig. 5-1(ii, c)). Fig. 5-1(ii, d) shows a simulated TEM image obtained using this atomic model. For comparison, we also modeled and simulated a TEM image of alkane, a zigzag hydrocarbon chain (Figs. 5-1(ii, f and g)). In Figs. 5-1(ii, b, e, and h), the chain structures are clearly seen after Fourier filtering the original images (Figs. 5-1(ii, a, d, and g)). No zigzag structure was observed in Fig. 5-1(ii, b), and the simulated straight structures of carbynes agreed well with the observation.

After the above observation, the Pt atoms suddenly moved 3 nm away from the observed area. There was no pore where the Pt atoms had been before, suggesting that the source of the carbyne growth was the C adatoms on the graphene surface. When there were not enough C atoms, the Pt

atoms pulled C atoms from the graphene lattice and created small pores in the structure, as described in Chapter 4. Under such conditions, we observed no carbynes.

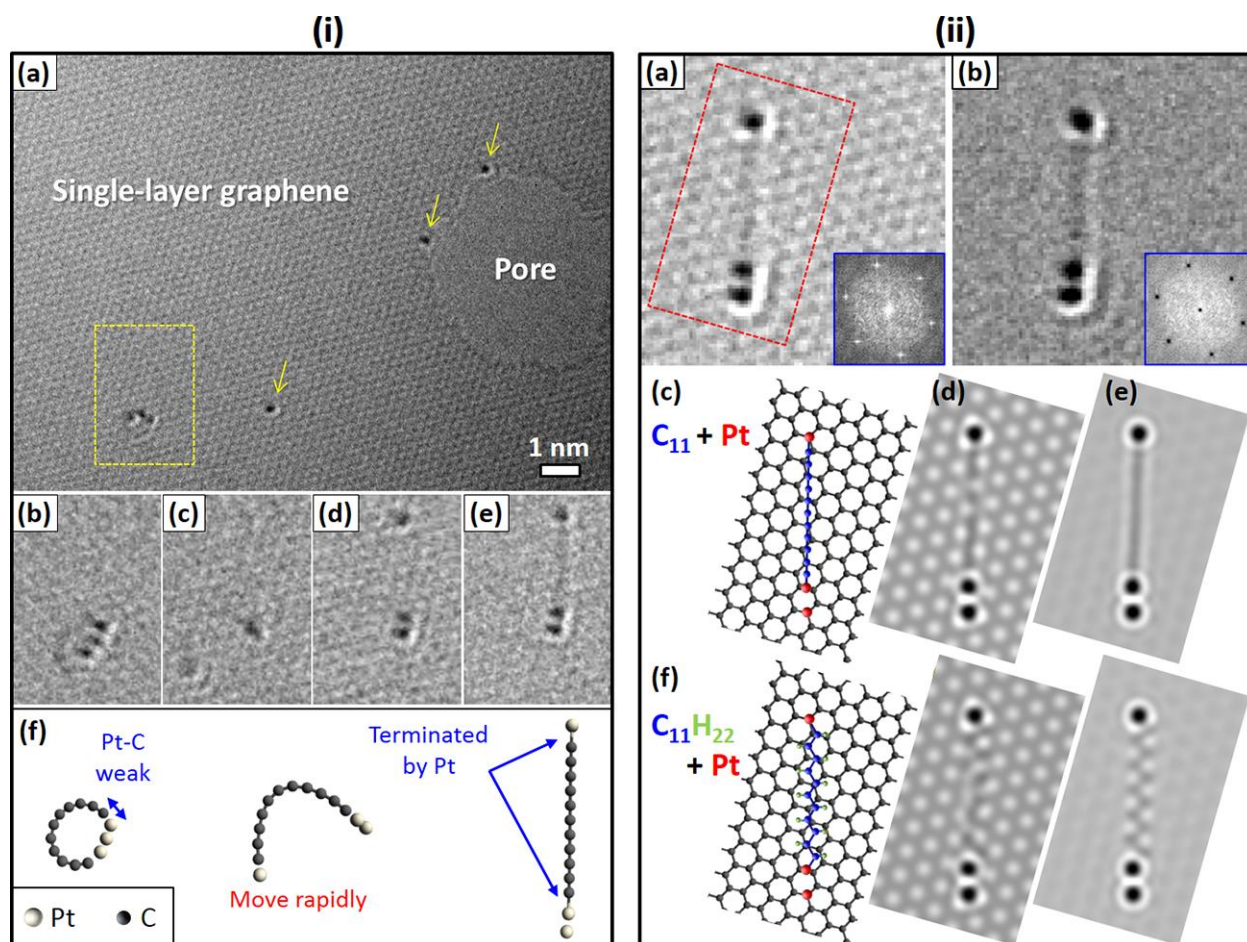


Figure 5-1 Observation of carbyne with Pt atoms.

(i) (a) TEM image of three Pt atoms on graphene taken at underfocus. The yellow arrows indicate single Pt atoms (atoms appear black). (b–e) Selected snapshots within the yellow frame in (a). (b) C-shaped carbyne. (c–d) Consecutive images indicating the change from a C-shape to a straight structure. (e) Straight carbyne terminated by Pt atoms at both ends. (f) Schematic of the carbyne structures corresponding to (b), (c), and (e). (ii) (a) Averaged TEM image of straight carbyne. One of the raw images is (i, e). The red framed area was modeled and simulated as shown in (c–h). (b) Fourier filtered image of (a), with the graphene signals removed as shown in the inset FFT. (c–e) Modeled, simulated, and filtered images of straight carbyne C_{11} , terminated by Pt atoms. (f–h) Modeled, simulated, and filtered images of zigzag alkane $C_{11}H_{22}$, terminated by Pt atoms. Simulated images (d) and (g) were obtained at -4 nm defocus.

Metal-terminated carbynes on graphene

Figure 5-2 shows another carbyne chain that formed on three Cu atoms, where the Cu atoms substituted carbons in the graphene lattice and remained motionless. Fig. 5-2(i) shows the Fourier filtering process used to highlight carbyne and Cu atoms by removing the underlying graphene lattice in the left part. The misoriented grain to the right remained after the process. Contrary to Pt-terminated carbyne, carbyne on Cu was formed within 1 s, exhibited no C-shaped structure, and was observed relatively often. However, it was unstable, presumably because of the weak bonds between the Cu atoms and the ends of the chain. The two carbyne chains formed on 3 Cu atoms fluctuated a little for ~ 18 s (shown in the 11-28 s frames in Fig. 5-2(ii)). Then one end suddenly departed from Cu; unfolded, forming a single chain (29-32 s in Fig. 5-2(ii)), and got trapped by defects located at a grain boundary. Both ends hopped around by a few atomic steps and then stabilized (44-55 s in Fig. 5-2(ii)).

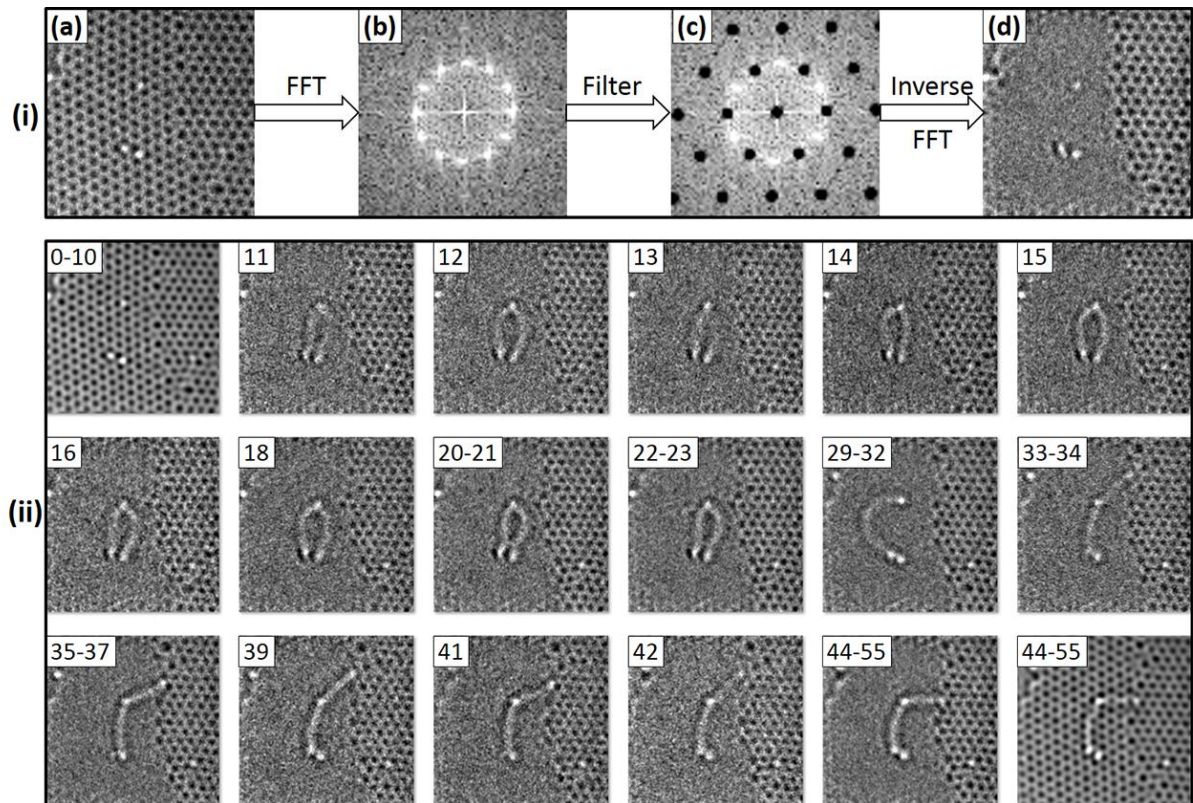


Figure 5-2 Cu-terminated carbyne

(i) Graphene signal was removed by Fourier filtering as follows: (a) a raw TEM image, (b) corresponding FFT image, (c) FFT mask and (d) filtered TEM image. (ii) Fourier-filtered consecutive images indicating the movement of carbyne. Substituted Cu atoms were quite stable and motionless. The inset numbers indicate frame time, where image (i, a) correspond to $t=0$ s.

5-3-2 Bending strength of carbyne

Theoretically, a straight carbyne chain should be stable. The persistence length l_p is often used to quantify the bending stiffness of a polymer. It is defined as $l_p = B_s / k_B T$, where B_s is the bending stiffness, k_B is the Boltzmann constant, and T is the temperature. The persistence length of carbyne was estimated at 14 nm at 300 K [218], which corresponds to 6.24 nm at 400 °C (673 K). This means a carbyne chain longer than 6.24 nm may bend thermally at 673 K.

However, in the present *in situ* observations, bending chains were also observed at an early stage of carbyne formation. Hu calculated the structures and properties of the bending chains using density functional theory [223]. He argued that because the strain energy of bending is much smaller than the energy required to break the chain, carbyne is a special soft material that is difficult to break by bending. The strain energy of bending E_{strain} is determined by the bending angles (θ_i) at all C atoms using the following equation:

$$E_{strain} = 2.54 \sum_{i=2}^{n-1} (1 - \cos(\theta_i)) \quad (5-1)$$

To simplify the tortuosity measurement of a curved line, Hu used the arc–chord ratio, which is the ratio of the length of a chain divided by the distance between its two ends. A larger arc–chord ratio means that the line is more curved. The arc–chord ratio that we observed was greater than the largest ratio in the model. For example, with Pt atoms, the carbyne ends merged and formed a ring. Its length was approximately 1.8 nm, corresponding to a chain of 14 C atoms with 1 Pt atom at one end. Assuming that all of the bending angles at the C atoms were the same, the bending strain energy was calculated as 2.6 eV from equation (5-1).

Belenkov *et al.* calculated the energy difference between a closed ring and C-shaped chain (ring with one broken bond) [224]. The energy falls in the range 122.04–149.80 kcal/mol (5.29–6.50 eV), which is close to the C=C binding energy. The strain energy 2.6 eV, due to the large bending, is two times smaller than the energy required to break the chain. Because the strain energy of bending increases with a decrease in the number of atoms, straight chains should preferentially form in case of a small carbon cluster. In our experiment, however, C-shaped chains were also observed in the early formation stage, possibly because both ends tended to be near the metal atoms. Carbynes are strong enough to maintain the curved structure without breaking, but the strain energy of bending rendered them unstable; for example, they fluctuated after strong bending and

assumed a linear shape. These changes were rapid for both Pt-terminated carbyne (Fig. 5-1) and Cu-terminated carbyne (Fig. 5-2).

5-3-3 Role of Pt and Cu atoms

We now discuss the role of terminated metal atoms. Both Pt and Cu served as nucleation sites for carbyne formation. If graphene has an ideal structure without any defects, all the atoms only weakly adsorb on graphene. The diffusion of such weakly adsorbed atoms is too fast for TEM imaging. Metal dopants in the graphene lattice play an important role in immobilizing atoms on graphene and in forming nucleation sites for new materials.

As mentioned above, the carbyne formation was faster and more frequent for Cu than Pt termination. We explain this observation by different binding energies between C and metal atoms, as discussed in Chapters 3 and 4: Cu atoms can promote nearby C–C rotations due to weak binding energy to C, while Pt atoms strongly bind nearby C atoms. On the other hand, once carbyne had formed, the strong bonding with Pt resulted in a more stable structure compared to Cu-terminated carbyne.

5-4 Summary

We have demonstrated a novel carbyne synthesis method using metal atoms on a clean graphene surface. Pt and Cu atoms act as nucleation sites and terminate the carbyne ends. Graphene allows both the movement and TEM observation of a carbyne chain. The chain bends significantly because the bending strain is small enough for the structure to remain intact; it can even form a ring that finally straightens into a linear shape when terminated by Pt atoms at both ends. Our observations prove the stability and bending strength of carbynes. In contrast to other top-down approaches (using carefully controlled tools to cut large materials), the observed carbyne chains were built up from single molecules: such a bottom-up approach can produce devices in parallel and is much cheaper than top-down approaches.

Chapter 6

2D copper oxide on graphene

We have discussed formation of monoatomic linear chain of carbyne in Chapter 4. The successful isolation and remarkable properties of graphene have recently triggered investigation of low-dimensional materials. However, one-atom-thick 2D materials without bulk-layered counterparts are scarcely reported. In this chapter, we report the structure and properties of novel 2D copper oxide cluster on graphene. STEM-EELS observations reveal that copper oxide can form monoatomic layers with an unusual square lattice on graphene.

6-1 Introduction

2D and quasi-2D materials have attracted increasing attention since the discovery of graphene, a one-atom-thick carbon sheet with honeycomb structure, obtained by exfoliation of bulk graphite [1], [2]. Single-layer graphene can maintain its structure because of strong covalent bonding within a layer, whereas the weak van der Waals forces acting between the layers allow its isolation. In the same way, 2D hexagonal boron nitride (*h*-BN) [225], [226] and quasi-2D sheets of transition metal dichalcogenides [227] and metal oxides, including perovskite-based oxides [228], [229], have been found so far, and reported to exhibit unique and attractive properties. These materials have their bulk counterparts with layered structures.

In contrast to the above reports, non-layered materials with wurtzite [230] and cubic [231] crystal structures were theoretically predicted to form 2D layers, and this possibility is important as it significantly widens the range of potential 2D materials. Very recently, graphene-like 2D zinc oxide clusters [232] and 2D iron clusters with a square lattice [156] have been observed by aberration-corrected TEM. In both cases the 2D layers were in the small pores in graphene, and their edges can be stabilized by bonding with carbon, whereas such geometry limits the size and properties of 2D materials [156], [233]. On the other hand, 2D zinc oxide sheets were also observed on metal surfaces by scanning tunneling microscopy [234], [235], indicating that large 2D sheets without bulk layered counterpart can be grown on a suitable substrate.

Here we report the structure and properties of a novel 2D material, copper oxide on graphene, observed by aberration-corrected STEM combined with EELS. In contrast to TEM images using bright field phase contrast [156], [232], ADF-STEM images are directly interpretable and useful for determining chemical species and number of atoms, as described in section 2-1. In STEM images, we observed one-atom-thick Cu clusters with a square lattice, while EELS analysis revealed that the 2D clusters contain oxygen. Density functional theory (DFT) calculations indicate that oxygen atoms play a key role in stabilizing the square 2D Cu lattice. They also predict that 2D copper oxide sheets have unusual electronic and magnetic properties different from 3D bulk copper oxide.

6-2 Methods

This section describes experimental methods that are specific to this chapter. Although the sample preparation methods are almost the same, experimental conditions are different from those described in Chapters 3–5. In particular, STEM-EELS experiments were conducted at room temperature without using a heating holder. The reported results are part of international collaborative research: the author experimentally observed 2D copper oxide on graphene, while Dr. Kvashnin (MISIS, Russia) performed first-principles calculations according to the experiments.

6-2-1 STEM-EELS experiments

The single-layer graphene on a Cu foil was transferred onto TEM grids. The grids were made of gold covered with an amorphous carbon support film with 2 μm diameter holes (Quantifoil[®], Quantifoil Micro Tools GmbH). Cu was then deposited using an ion beam etching system (PECS, Gatan Inc.). The samples include PMMA residue and were exposed to the atmosphere before STEM experiments, which consequently leads to incorporations of oxygen and hydrocarbon species. Those were attracted as contamination to the region where the focused electron beam was irradiated. As discussed above, heating inside the microscope reduced built-up contamination and chemical etching, but also reduced oxygen and led most of Cu atoms aggregate into 3D nanoparticles. When heated, 2D clusters have not been observed until now. Instead of heating, contamination was suppressed by wide-area electron-beam irradiation of the sample at room temperature.

Microscope (JEM-ARM200F, JEOL) was operated at 80 kV with a CEOS probe Cs corrector. The angular range of electrons that collected in the ADF detector was about 46–161 mrad. The incident beam current was ~ 55 pA, and a typical dose was $\sim 10^5$ electrons per \AA^2 per image. All the results about 2D copper oxide were obtained at room temperature. To improve the signal-to-noise ratio, STEM images were low-pass filtered, and the EEL spectrum of 2D copper oxide was spatially averaged. Image simulation was performed using multislice software (xHREMTM, HREM Research Inc.) under the following conditions: the convergence semi-angle 28.5 mrad, third- and fifth-order spherical aberration coefficients 5 μm , ADF detector angle 46–161 mrad, and probe size 0.8 \AA . Simulations included thermal diffuse scattering absorption with the Debye-Waller factors of each element taken from the literature [164]–[166].

6-2-2 First-principles calculations

All calculations of the atomic structure and stability of the 2D copper oxide were performed using DFT within the Perdew-Burke-Ernzerhof (PBE) functional [202]. We used the projector augmented wave method [236] approximation with the periodic boundary conditions and a Vienna Ab initio Simulation Package [237]–[240]. The plane-wave energy cut-off was set to 450 eV. To calculate the equilibrium atomic structures, the Brillouin zone was sampled according to the Monkhorst–Pack scheme [204] with a $16 \times 16 \times 1$ grid in the k space. The structural relaxation was performed until the forces acting on each atom became less than 0.001 eV/ \AA . The model of the 2D copper oxide cluster on graphene consisted of 161 C atoms, 22 Cu atoms and 24 O atoms, including atoms at the cluster edges. The cell size was larger than 15 \AA to avoid the interaction between clusters. For investigation of the stability, elastic, electronic and magnetic properties, we used infinite models with the unit cell comprising 4 Cu atoms and 4 O atoms. The evolution of 2D copper oxide cluster structure at the finite constant temperature was described in the framework of the molecular dynamics (MD) simulations using the Nosé–Hoover thermostat [241], [242]. Temperature was set at 300 K and 600 K to match the experimental conditions. The total time of the simulations was 0.45 ns with the time step of 1 fs. Atomic structure was written after every ionic steps.

6-3 Results and discussion

6-3-1 STEM-EELS observations

Figure 6-1 shows ADF-STEM images of Cu clusters and atoms on graphene observed at room temperature. Because of the electron irradiation prior to high-resolution imaging, contamination was suppressed, but it also damaged graphene (small pores shown in Fig. 6-1 (a)). When we magnified the light blue area in Fig. 6-1 (a), structure of the thin cluster slightly modified; the intensity of constituent atoms of the cluster became uniform (Fig. 6-1(b)). We colored the STEM images to enhance the intensity contrast (Fig. 6-1(c)). The blue areas correspond to graphene, isolated red dots are Cu atoms, and yellow to white parts correspond to 3D nanoparticles. Intensity of ADF-STEM images increases with the atomic number Z as about $Z^{1.5-1.8}$ and is proportional to the sample thickness [161]. In our images, Cu atoms were ~ 12 times brighter than C atoms of graphene. All atoms in the thin Cu cluster had almost the same intensity as single Cu atoms dispersed on graphene. This indicates that the clusters are composed of a 2D Cu sheet with one-atom thickness.

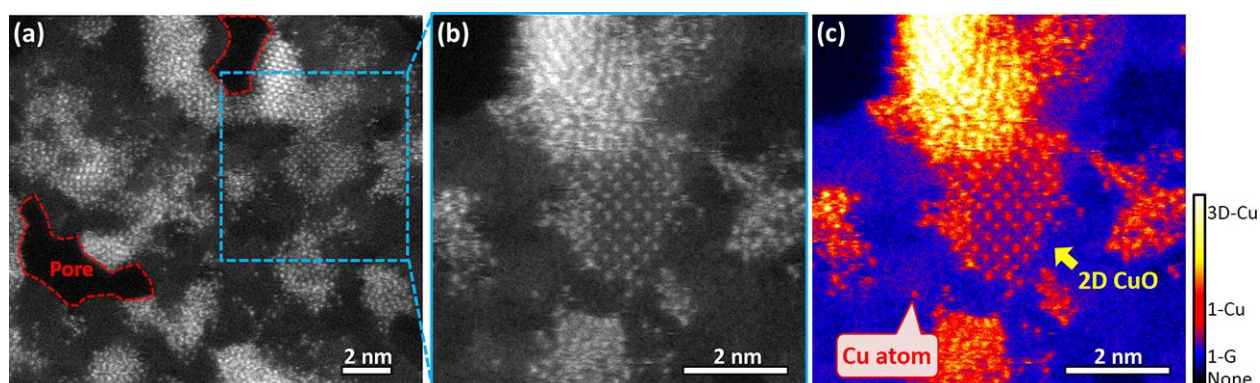


Figure 6-1 STEM images of copper oxide on a graphene sheet

(a) Low-magnification STEM image of Cu doped graphene, where red circle indicate graphene pores that made by electron irradiation at room temperature. (b) Magnified STEM image taken at blue box area in (a). (c) Colored version of (b) that highlights the contrast.

We performed EELS analysis to elucidate the composition of this 2D cluster. Figures 6-2(a) and (b) show another 2D cluster on graphene (indicated by the green arrow in (a)), where (b) is low-pass filtered, magnified and trimmed. EEL spectra from this cluster indicate the presence of C, O and Cu. Figure 6-2(c) shows a carbon K-edge spectrum, which exhibits the typical features of sp^2 -coordinated carbon, graphene. The top two spectra in Fig. 6-2(d) are the experimental spectra of the 2D copper oxide cluster (green) and 3D Cu nanoparticle (black), together with the reference spectra of bulk CuO and Cu [177]. In the green spectra, we can see the oxygen K-edge and sharp copper L_2 and L_3 peaks, the so-called white lines, indicate a partial emptying of the Cu 3d band caused by chemical bonds with oxygen [175], [176]. Although the black spectra also contain small oxygen peaks presumably originating from residues, they do not show sharp Cu threshold peaks. These results allow us to conclude that the 2D clusters consist of one-atom-thick copper oxide supported on a graphene sheet.

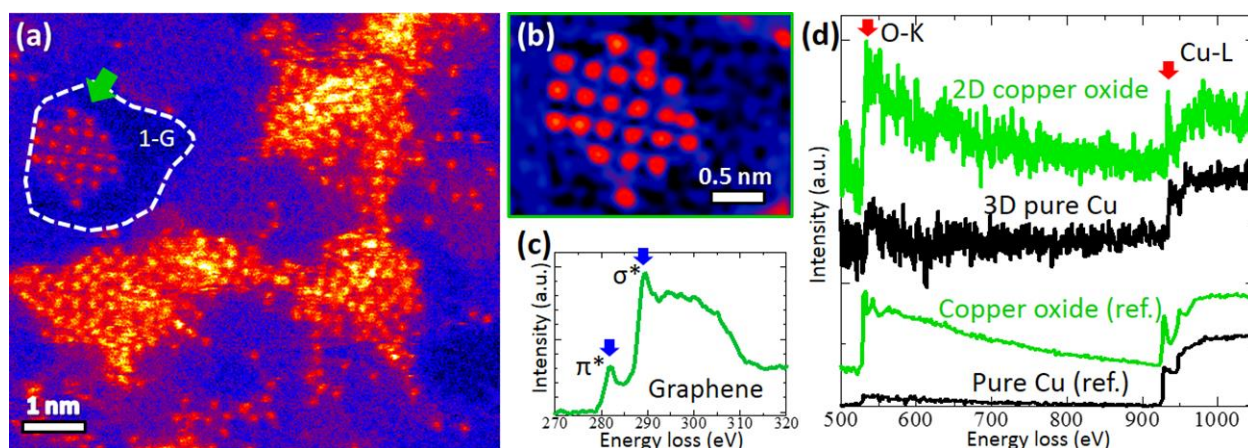


Figure 6-2 STEM-EELS analysis of 2D copper oxide on a graphene sheet

(a) Colored STEM image of a 2D cluster on graphene. The white dashed curve indicates boundaries between single- and double-layer graphene. (b) Low-pass filtered image of the 2D cluster marked by the green arrow in (a), where trimmed and magnified. (c) Extracted carbon K-edge spectrum obtained from the 2D cluster shown in (a) and (b). (d) Extracted copper L-edge EEL spectra. The top green spectrum was obtained from the 2D cluster at room temperature, while the second black spectrum was obtained from pure Cu nanoparticles aggregated at 300 °C. The bottom two spectra are reference spectra of copper oxide and pure copper [177].

2D copper oxide on graphene

Figure 6-3 shows other STEM images of 2D copper oxide clusters. The intensity line-profiles shown in Fig. 6-3(d) were taken along the white dashed lines in Fig. 6-3(b) and (c). As illustrated in Fig. 6-3(d), the cluster in Fig. 6-3(c) had several additional Cu atoms on the top of Cu atoms in the first Cu layer, judging from the fact that the intensities of the brighter dots on the dashed line were twice as large as that of the single Cu atom. Again, all atoms in the thinnest Cu cluster (e.g. Fig. 6-3(b)) had almost the same intensity as single Cu atoms dispersed on graphene, indicating that the clusters had one-atom thickness.

We measured the distances between Cu atoms in the 2D copper oxide cluster in Fig. 6-3(b). The 2D clusters had a square lattice with a different lattice spacing from that of a top-left 3D nanoparticle. The Cu–Cu distance in the 2D cluster (yellow square in Fig. 1a) was $2.83 \pm 0.06 \text{ \AA}$, while that of the 3D nanoparticle was $2.13 \pm 0.01 \text{ \AA}$. The latter value is identical to the spacing between (200) planes of bulk Cu_2O ; hence, we identify the 3D nanoparticle as Cu_2O . Meanwhile the former value of the 2D cluster does not fit into any lattice spacing of bulk Cu, Cu_2O or CuO .

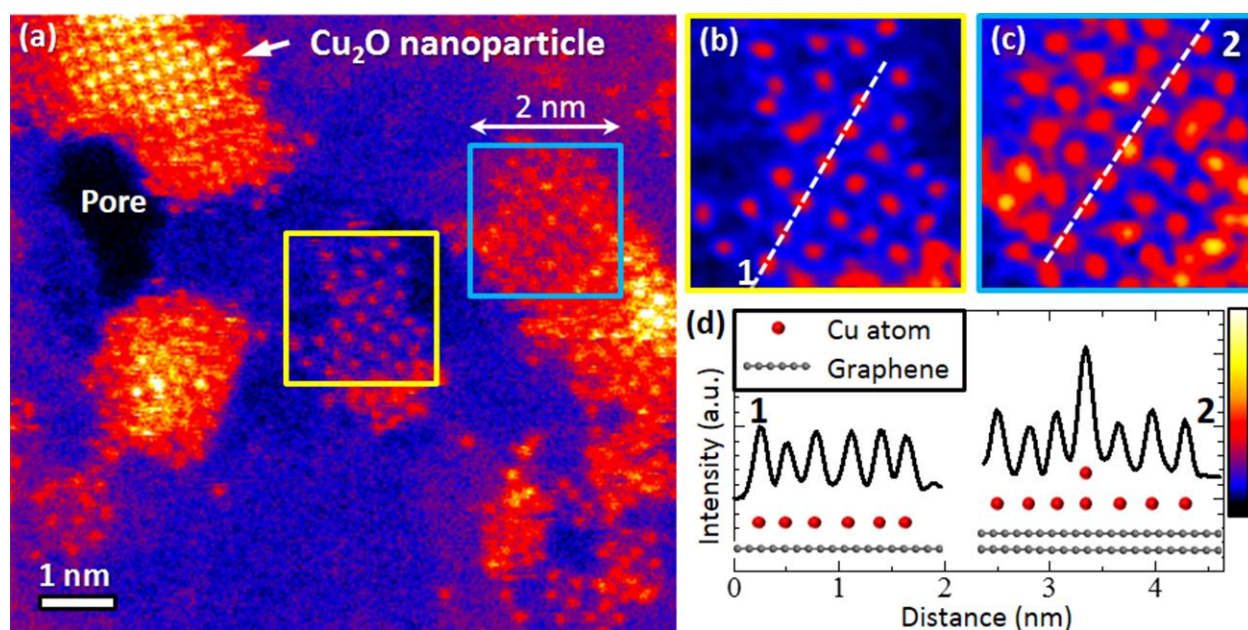


Figure 6-3 Distance between neighboring Cu atoms in 2D copper oxide

(a) Colored STEM images of Cu clusters on graphene. The 2D clusters marked by the yellow and light blue boxes in (a) were magnified and low-pass filtered in (b) and (c), respectively. (d) Line-profiles with schematic of 2D copper oxide and graphene taken through the white lines marked in (c) and (d).

These experimental results reveal that the observed 2D cluster consists of one-atom-thick copper oxide. From the measured Cu–Cu distance of $2.83 \pm 0.06 \text{ \AA}$, we presumed that the atomic positions of Cu and O in 2D clusters differ from general 3D bulk CuO or Cu₂O, as shown in Fig. 6-4. Bulk Cu₂O has a larger distance between neighboring Cu atoms of 3.02 \AA in a cubic structure. Figure 6-4(c) shows model of 2D copper oxide calculated using the CASTEP module of Materials Studio (BIOVIA). When we located O atoms at the center of the Cu square lattice, the Cu-Cu distance (2.75 \AA) agreed with the experiment. Bulk CuO does not have a cubic structure, but the O position in (010) plane is similar to our 2D atomic model.

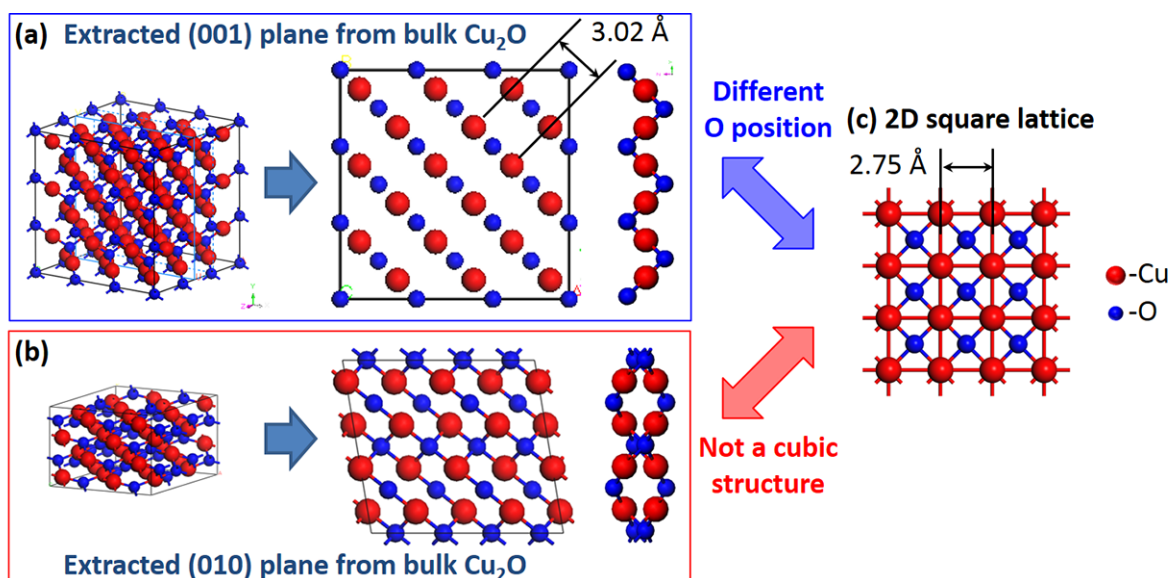


Figure 6-4 Bulk Cu₂O and 2D copper oxide

Atomic models of (a) bulk Cu₂O and its cross-section along the (001) plane and (b) bulk CuO and its cross-section along the (010) plane. (c) Atomic model of 2D flat copper oxide optimized using the CASTEP module of Materials Studio. Cu and O are illustrated by red and blue balls, respectively.

6-3-2 DFT calculations and image simulations

DFT calculations were performed to further investigate the structure and stability of 2D clusters. We designed models of 2D copper oxide, pure copper, and copper carbide with square lattices according to the experimental STEM image in Fig. 6-2. DFT calculations revealed that only copper oxide could maintain its square lattice on graphene (Fig. 6-5(a)), while other structures collapsed into an amorphous state even at 0 K (Fig. 6-5(b) and (c)). During the optimization, pure copper clusters transformed into a hexagonal lattice, while C atoms in copper carbide moved out from the Cu square lattice to form dimers.

These calculations allow us to exclude pure copper and copper carbide from consideration, and we conclude that only oxygen can stabilize a square 2D Cu lattice. The DFT calculations show that the O atoms locate at the center of the Cu squares; they strengthen the square lattice and suppress out-of-plane distortions. Compared with Cu-O bonds, Cu-C bonds have low polarity due to the small electronegativity difference between Cu and C; therefore, copper carbide prefers to form tetrahedral structures. Cu-O bonds are more flexible due to the polar covalent nature and can be uniformly arranged in a square lattice. This configuration is unusual and might be intrinsic to 2D metal oxides.

The arrangement of O atoms in 2D copper oxide was also confirmed by STEM. Figures 6-6(a) and (b) are experimental and simulated ADF-STEM images, and the intensity line profiles were obtained along the white dashed lines. The experimental line profile agrees well with the simulated one for both Cu and O atoms represented by the large and small peaks, respectively.

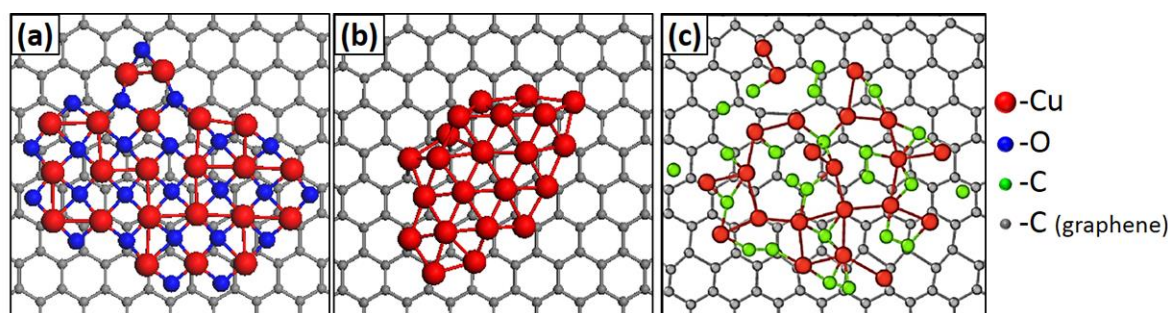


Figure 6-5 2D copper oxide, pure copper and copper carbide

Atomic models of (a) 2D copper oxide, (b) pure copper and (c) copper carbide after DFT relaxation at 0 K.

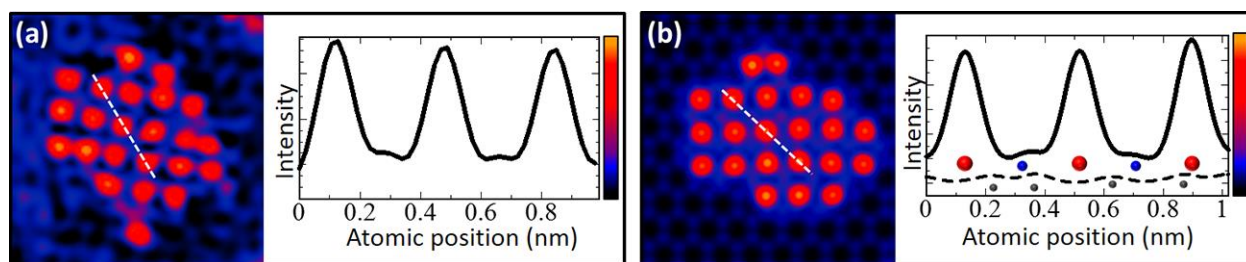


Figure 6-6 Comparison between experiment and image simulation

(a) Low-pass filtered STEM image of the 2D cluster and line-profile through the white line. (b) Simulated STEM image using the model of Fig. 6-5(a) and line-profiles through the white line. In the simulated line profiles, the positions of Cu, O, and C atoms are illustrated by red, blue, and gray balls, respectively. The dashed line profile in (b) indicates the intensity of the separately simulated image of the graphene sheet without the 2D cluster.

We calculated the activation energy and total energy change for the transformation between 2D infinite sheets of copper oxide and pure copper (Figure 6-7). During STEM experiment, a part of O might be removed from the Cu square lattice by strong electron irradiation, but O atoms can easily fill in the square Cu lattice without an energy barrier. Furthermore, the high energy-barrier suppresses removal of O atoms from 2D Cu_2O . These results explain how oxygen can stabilize 2D copper oxide, although we used simplified models not taking into account the effect of underlying graphene substrate. DFT calculations further suggest that O atoms at the cluster edges additionally stabilize the 2D square lattice. 2D copper oxide clusters bind with graphene only when the graphene sheet has vacancy defects, and even in that case the other parts of the cluster can maintain its structure without forming strong bonds with graphene.

Yang *et al.* [243], [244] reported that the hexagonal lattice is the most stable structure for the infinite 2D Ag or Au sheet; however, we should take into account the edge instability for finite 2D metal sheets. The edges of the hexagonal 2D Cu clusters are strained and chemically active; therefore, they bind with the graphene surface. The bonds distort the 2D structure and transform it into 3D structure.

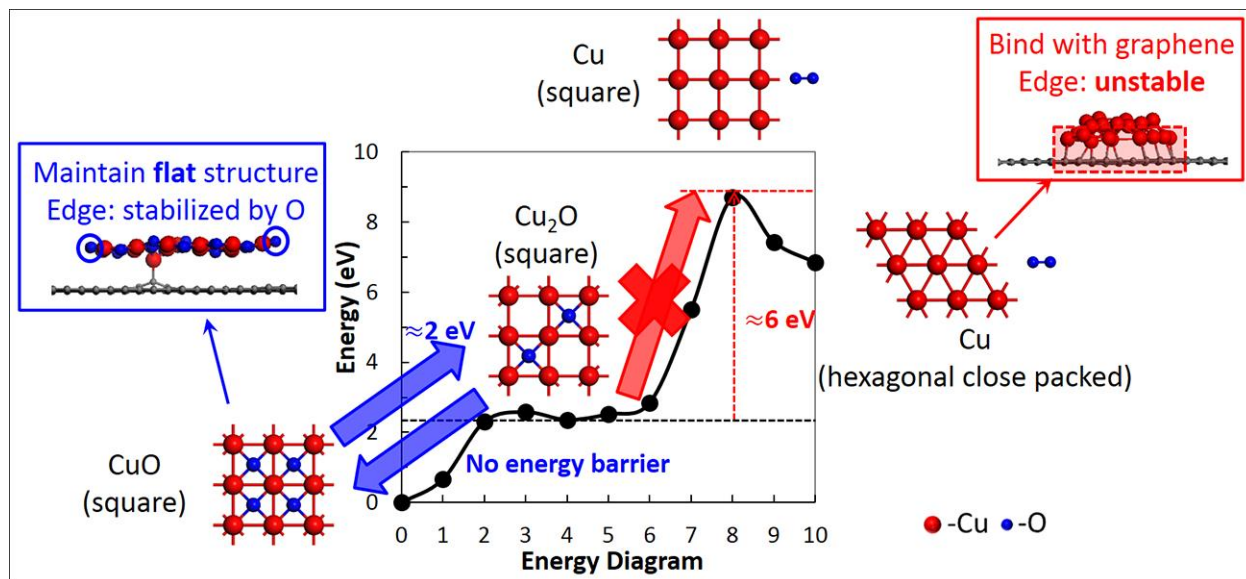


Figure 6-7 Energy diagram of transformation between CuO and Cu

Energy diagram of the simplified transformation between infinite square 2D CuO and hexagonal 2D Cu with physisorbed O₂ molecules, including the transition state of 2D Cu₂O. Desorption of O from 2D Cu₂O lattice requires huge energy penalty of ~6 eV/unit cell (the unit cell consisted of 4 Cu and 4 O atoms).

6-3-3 Properties of 2D copper oxide

The unusual atomic geometry of 2D copper oxide leads to unexpected electronic and magnetic properties. 2D copper oxide is predicted to have semiconducting properties with the band gap of 2.7 eV, and major contributions of Cu states at the bottom of the conduction band and O states at the top of the valence band. In contrast, bulk CuO is a semiconductor with the band gap of ~1.5 eV [245]. Furthermore, 2D copper oxide has an antiferromagnetic ground state, whereas bulk Cu and CuO are paramagnetic.

We also estimated the in-plane stiffness of 2D copper oxide at 123.7 N/m by *ab initio* calculation, which is lower than that of graphene (340 N/m) [246], but comparable with those of transition metal dichalcogenides (123–180 N/m for single-layer MoS₂ and WS₂) [247]–[249]. 2D copper oxide has a high stiffness because Cu and O atoms in the 2D sheet form strong covalent bonds with the binding energy of 4.07 eV. In addition, the mechanical stability of the 2D cluster against bending was examined by comparing the total energy of flat 2D copper oxide with copper oxide nanotubes. Calculations show that the copper oxide nanotube with a radius (~ 0.86 nm) is

energetically more stable than the 2D sheet, implying necessity of graphene as a substrate for the 2D copper oxide.

MD simulations further suggest that a small 2D copper oxide cluster (~1.4 nm in lateral size) on graphene has a curved structure slightly displaced from the graphene surface with keeping its square lattice at 300 K (Figure 6-8 (a)). In contrast, the simulation at 600 K shows that a 2D copper oxide cluster on graphene started to melt in a short time (~0.25 ns, Fig. 6-8(b)). These results explain the experimental fact that the 2D copper oxide clusters were observed in the present study at room temperature, but not observed when the sample was heated at 300 °C.

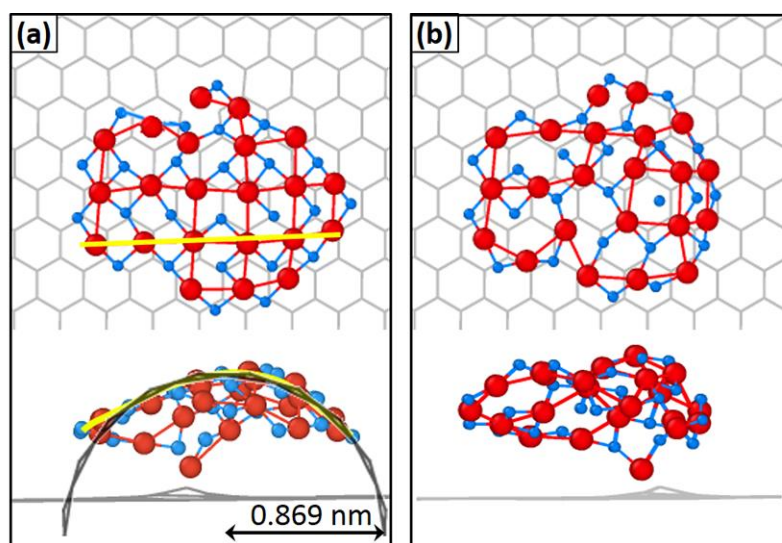


Figure 6-8 Molecular dynamics simulation of 2D cluster on graphene

Top and side views of the atomic structure of 2D copper oxide cluster on graphene (a) after 0.45 ns simulated at 300 K and (b) after 0.25 ns at 600 K. The curvature radius in (a) agree with the radius of the stable nanotube.

6-4 Summary

We have demonstrated and characterized one-atom-thick 2D copper oxide clusters with unusual square lattice on graphene. STEM-EELS observations and DFT modelling reveal that O is located at the center of the square Cu lattice and thereby stabilize it. Calculations show that 2D copper oxide has a metallic conductivity and antiferromagnetic spin ordering different from bulk copper oxide. We believe that the present results will pave the way for the investigation of novel 2D nanostructures with unusual lattice geometry.

Conclusions

Interaction dynamics between metals and graphene was observed by *in situ* aberration-corrected TEM and STEM combined with EELS. We have found following two interesting phenomena under electron beam irradiation:

- (1) Graphene reconstruction promoted by substitutional metal atoms in graphene lattice
 - ◆ Substitutional Cu atoms reconstruct graphene via repeated C–C rotation (Chapter 3)
 - ◆ Opposite effects of Cu and Pt at graphene edges: mending and etching (Chapter 4)
- (2) Self-assembly of novel low-dimensional structures on graphene surface
 - ◆ Pt- or Cu-terminated carbyne (Chapter 5)
 - ◆ One-atom-thick 2D copper oxide with unusual square lattice (Chapter 6)

Both phenomena were promoted by the energy transferred from incident electron beam, which offers enough energy to reconstruct graphene (1). The same electron beam also promoted migration of source atoms to create novel low-dimensional materials (2). Electron beam irradiation effects explain most phenomena reported in this thesis. An aberration-corrected microscope and a clean sample preparation technique allows us to observe dynamics of individual atoms on graphene.

In regards to (1), we demonstrated for the first time that single Cu atoms could catalyze reconstruction of graphene structures under electron irradiation. In this thesis we investigate noble metals, Cu, Pt and Au, because they are promising elements for single-atom catalysis. Indeed, we have found that substitutional Cu atoms promote reconstruction of single-layer graphene, via repeated rotation of C–C bonds near Cu atoms, see Chapter 3. Furthermore, we report that individual Cu and Pt atoms promote opposite effects on graphene edge: Cu mediated mending, while Pt mediated etching, promoted by electron beam irradiation, see Chapter 4. The difference can be explained by the binding energies to C. Strong Pt-C bond would strain graphene lattice and promote etching, while Cu can compensate such strain via C–C bond rotations.

Regarding (2), we observed bottom-up nucleation processes, i.e. self-assembly from single atoms or molecules of metal-terminated carbyne and 2D copper oxide cluster. Metal-doping in graphene served as a nucleation for the formation. Self-assembly offers an important advantage

Conclusions and Future perspectives

over top down fabrication. It potentially allows production of novel structures in parallel. In this case, graphene acted as a support membrane, an ultimate thin film for the visualization of small and thin materials in a TEM. It is difficult to produce and observe such small and thin materials; therefore, *in situ* TEM observations are important for understanding their structures and formation mechanisms.

Future perspectives

Thermal effects

We have demonstrated electron beam-induced transformation, which provides important insight in the materials. *In situ* heating was useful to prepare and observe clean graphene. Our improved the sample preparation methods allowed us to avoid unwanted metal impurities on graphene. Our methods can be applied to the other experiments where clean surface are essential. However, we cannot take into account thermal energy effect because 150–300 °C heating temperature was too low to become a main driving force of observed structural transformations. To consider growth mechanisms of nanocarbon materials, it would be desirable to observe the behavior of metal and C atoms at the higher temperatures. For reference, graphene and carbon nanotubes grow by CVD methods at ~1000 °C. Cu atoms and nanoparticles rapidly evaporated in vacuum at ~500 °C, thus a different element that strongly binds with graphene or that has a higher melting point may be suited for high-temperature experiments.

Substrate effects on the formation of novel structures

When considering self-assembly of novel structures, substrate would strongly affect their structure and stability. This thesis describes the formation of metal-terminated carbyne and 2D copper oxide on graphene surface. It is obvious that graphene acts as the ultimate-thin substrate. However, it is not entirely clear if graphene is essential not only for visualization but also for the growth of novel nanostructures. It is possible that both carbyne and 2D copper oxide could grow on the support materials because the interaction with graphene is expected to be weak. The source atoms or molecules are only weakly adsorbed on graphene and their diffusion is easily promoted by heating or by electron beam irradiation; therefore, their formation is possible on graphene. A

Conclusions and Future perspectives

strong interaction with substrate may strain and disturb the synthesized structure, for example due to a lattice mismatch.

Regarding the effect of substrate on nanostructure growth, other 2D materials, such as transition metal dichalcogenides or BN, may also be used as ultrathin substrates for the formation of novel nanostructures and for *in situ* TEM experiments. Many 2D materials can be utilized as a substrate, and the choice depends on the type of nanostructure to be deposited.

Analysis of clusters and nanoparticles

Although single-atom catalysis is an exciting fundamental research field, it is also important to investigate what happens when atoms form clusters or nanoparticles. Clusters containing only a handful of atoms may exhibit different features and structures that does not exist in the bulk. The analysis of small clusters and their interaction with graphene is an exciting direction of future research.

In closing, a variety of novel low-dimensional structures has been found so far, and it is likely that many more are still to be discovered. Although atomic-resolution imaging provides only local information, it is a powerful technique providing undisputable evidence of existence of the reported nanostructures and their crystallographic structure. In this thesis, we demonstrated that single metal atoms could catalyze modification of graphene structure. Electron beam irradiation can be utilized as a means of controlling and fabricating such new nanostructures, thereby opening a new field in material sciences. Our results provide fundamental insights into the interaction between metal atoms and graphene. Furthermore, our results offer a promising method of controlling structures at the atomic scale for future applications.

Appendix

Detector angle of ADF-STEM (cf. subsection 2-1-1)

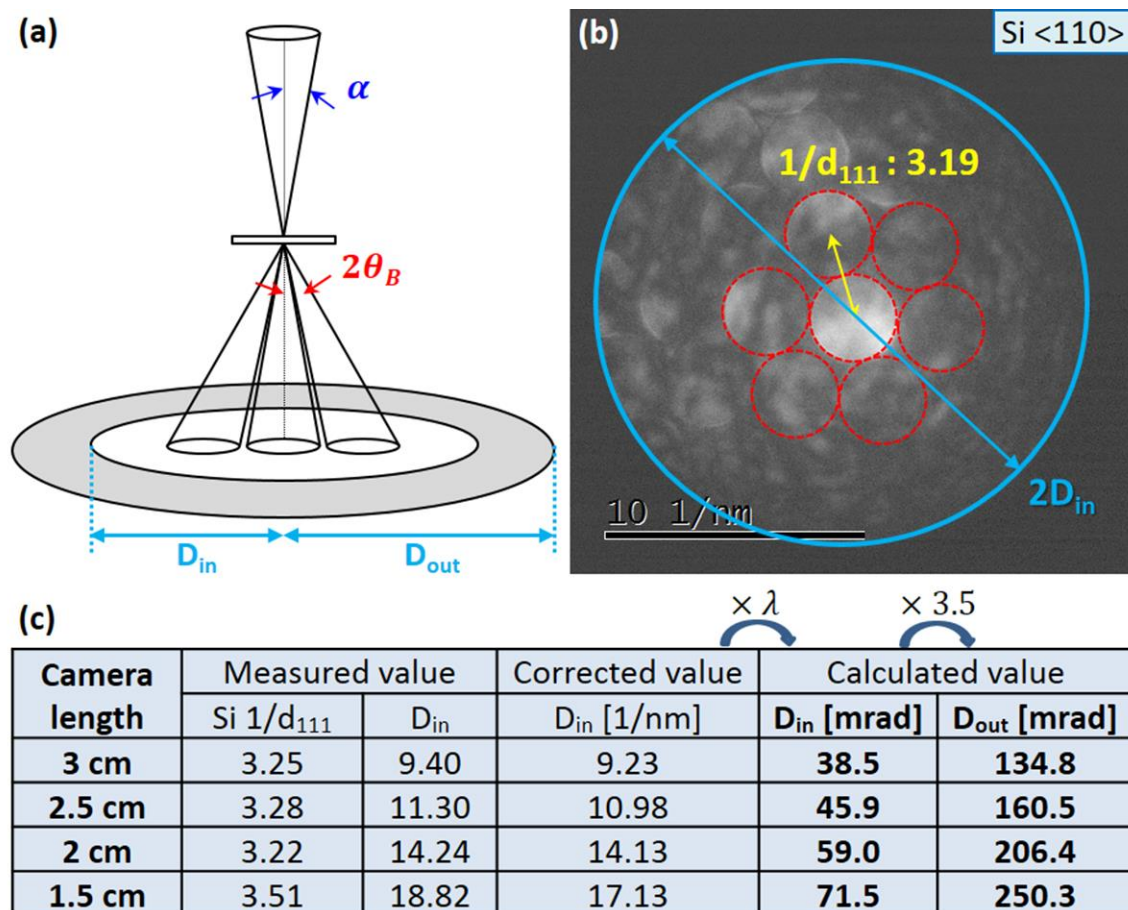


Figure A-1 Measurement of detector angle for ADF-STEM

(a) Schematics of convergent-beam electron-diffraction (CBED). (b) CBED pattern of Si sample taken at the detector plane. (c) Table of detector angle for each camera length L (wavelength $\lambda=0.00418 \text{ nm}$ for accelerating voltages of 80 kV). Our microscope (JEM-ARM 200F) equips two ADF detectors, and we used Gatan ADF detector with $L = 2.5 \text{ cm}$ for STEM-EELS measurements. The detector angles were measured using the smallest condenser aperture with a convergence semi-angle of 6.6 mrad, while high-resolution imaging were performed using larger aperture with that of 28.5 mrad.

EELS analysis (cf. section 2-1-3)

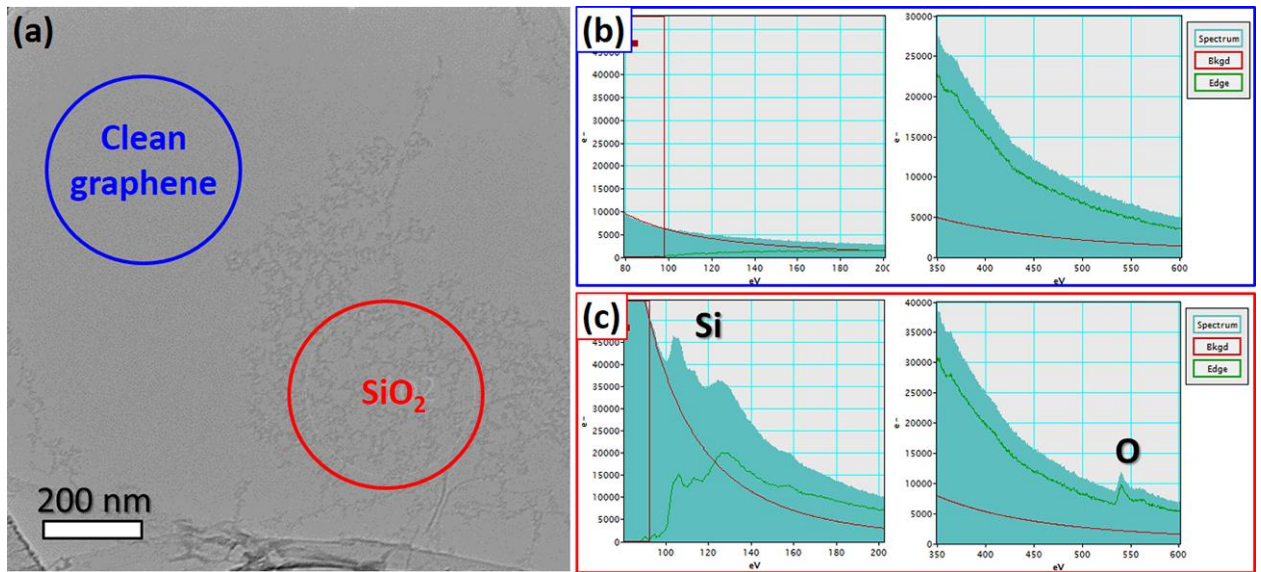


Figure A-2 TEM-EELS analysis of graphene on an *in situ* heating chip

(a) TEM image of single layer graphene taken at 1000 °C. (b) EEL spectra obtained from the clean graphene area in (a). (c) EEL spectra obtained from the SiO₂ contaminated area in (a). Graphene spectrum from clean graphene area is shown in Fig. 2-8(b) of the main text.

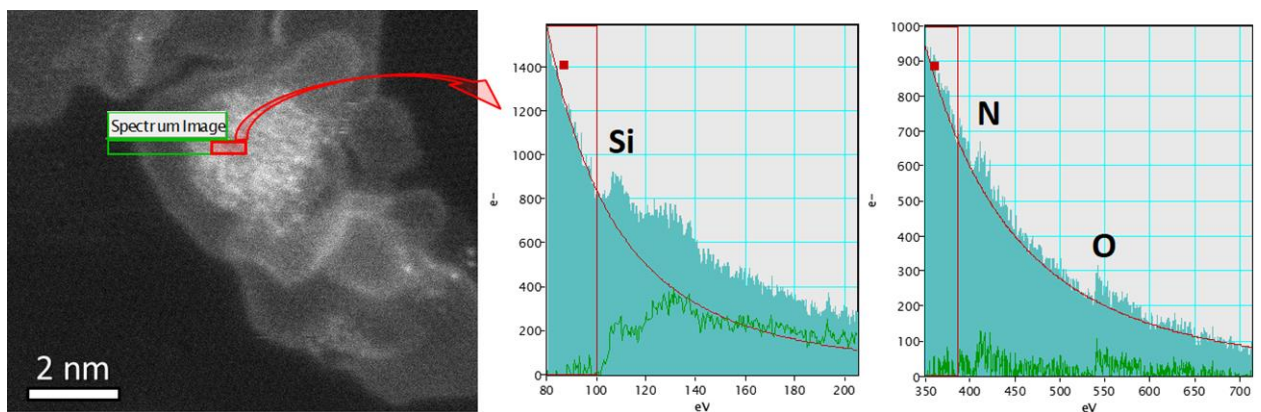


Figure A-3 STEM-EELS analysis of graphene on *in situ* heating chip

STEM image and corresponding EEL spectra of Cu-deposited graphene taken at 400 °C. Most Cu nanoparticles and atoms were evaporated at 400 °C. Furthermore, heating at temperatures above 400 °C for long time resulted in diffusion of Si-based impurities, although we excluded the heavily Si-contaminated areas, as discussed in subsection 3-2-1.

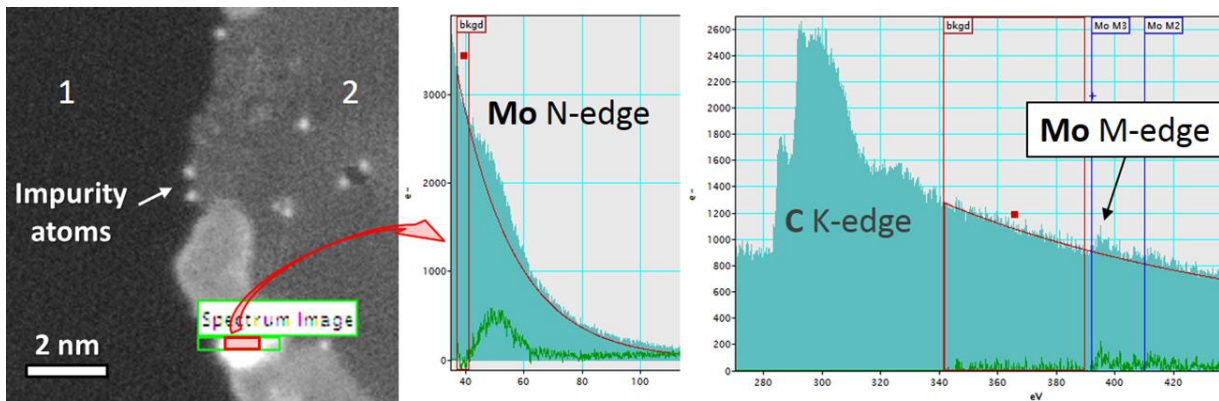


Figure A-4 STEM-EELS analysis of graphene on Mo grid

STEM image and corresponding EEL spectra of graphene taken at ~ 500 °C. The CVD graphene was transferred onto a TEM grid made of Mo covered with an amorphous carbon support film (Quantifoil[®], Quantifoil Micro Tools GmbH). As described in subsection 2-3-2, we used Au grids to avoid Mo impurities from the grids.

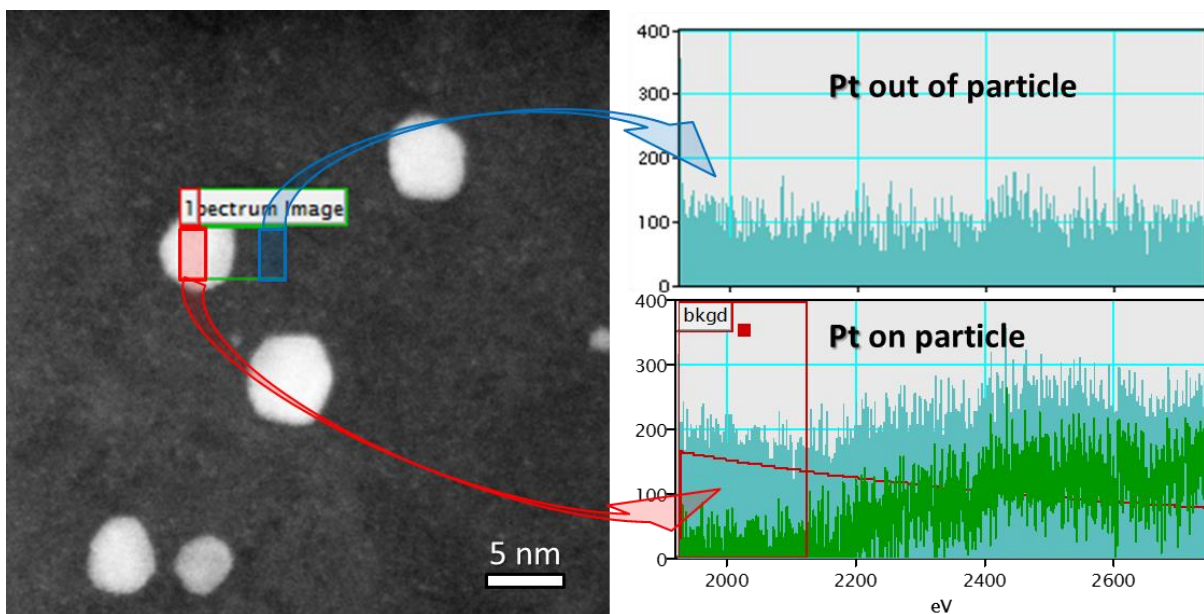


Figure A-5 STEM-EELS analysis of Pt-deposited graphene

STEM image and corresponding EEL spectra of Pt-deposited graphene taken at room temperature after heating at 1000 °C. Since it is hard to detect EELS signals from individual atoms, we analyzed nanoparticles and confirmed that the deposited metal was Pt. Furthermore, Pt atoms appear much brighter than C, Si, or Cu in both TEM and STEM images, as described in subsection 2-1-2, so that they are easy to detect by image intensity.

CVD graphene grown on Ni (cf. subsection 2-3-1)

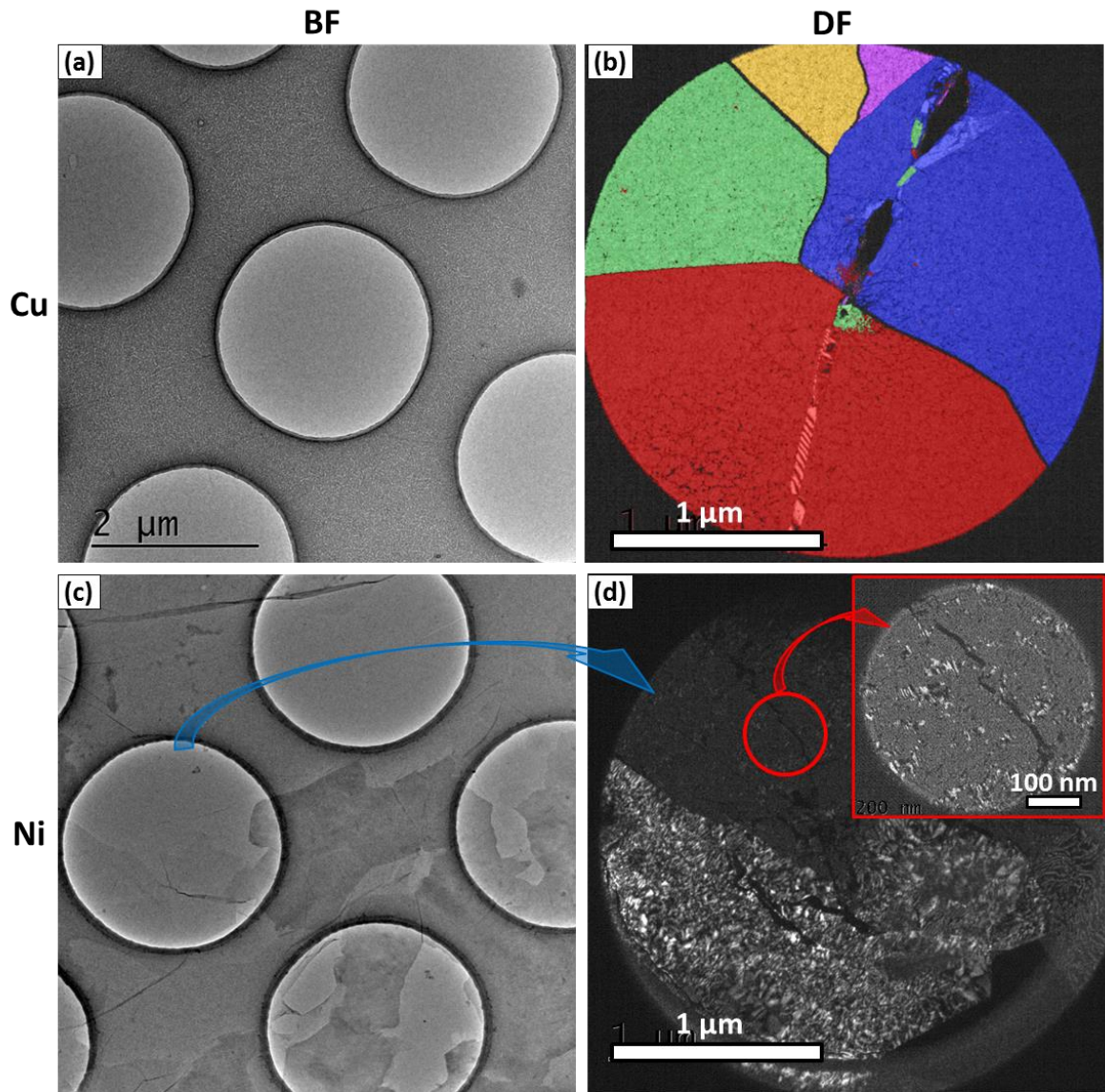


Figure A-6 Comparison between Cu-CVD and Ni-CVD graphene

(a) BF-TEM and (b) colored and overlaid DF-TEM images of uniform single-layer graphene grown on Cu foil (Graphene Platform Corporation). (c) BF-TEM and (d) DF-TEM images of nonuniform thick graphene grown on Ni (Graphene Supermarket®). In the Ni-CVD sample, there are tiny graphene flakes, as shown in the inset in (d)

Dynamics of Cu atoms substituted in a graphene lattice (cf. Chapter 3)

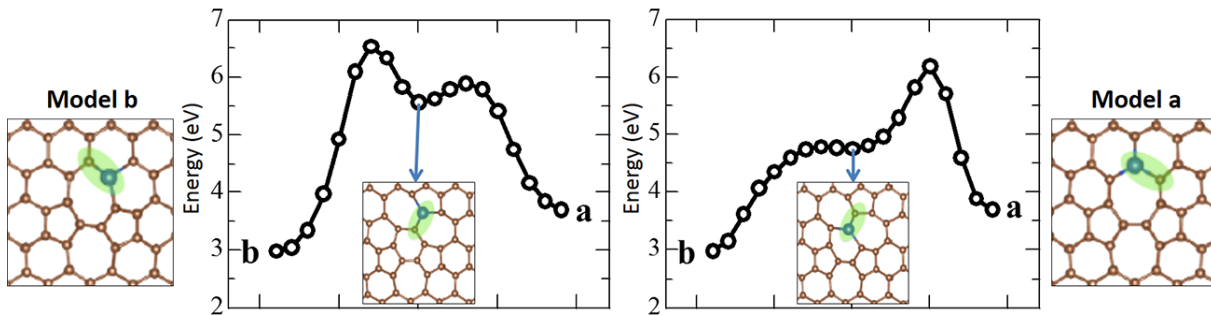


Figure A-7 DFT calculation of energy diagram of C–Cu rotation

There were two paths for the 180° C–Cu rotation (clockwise or counterclockwise) and two corresponding small valleys at 90° rotation. The 577 structure in the left diagram will easily transform into either the structure a or b (both energy barrier were smaller than 1 eV), whereas the 677 structure in the right diagram will preferentially transform into the structure b. These halfway structures contain multi SW defects and have higher total energies than the other structure. Therefore, whole transformations will proceed to reduce these defects, although both generation of defects and their healing will occur along the way.

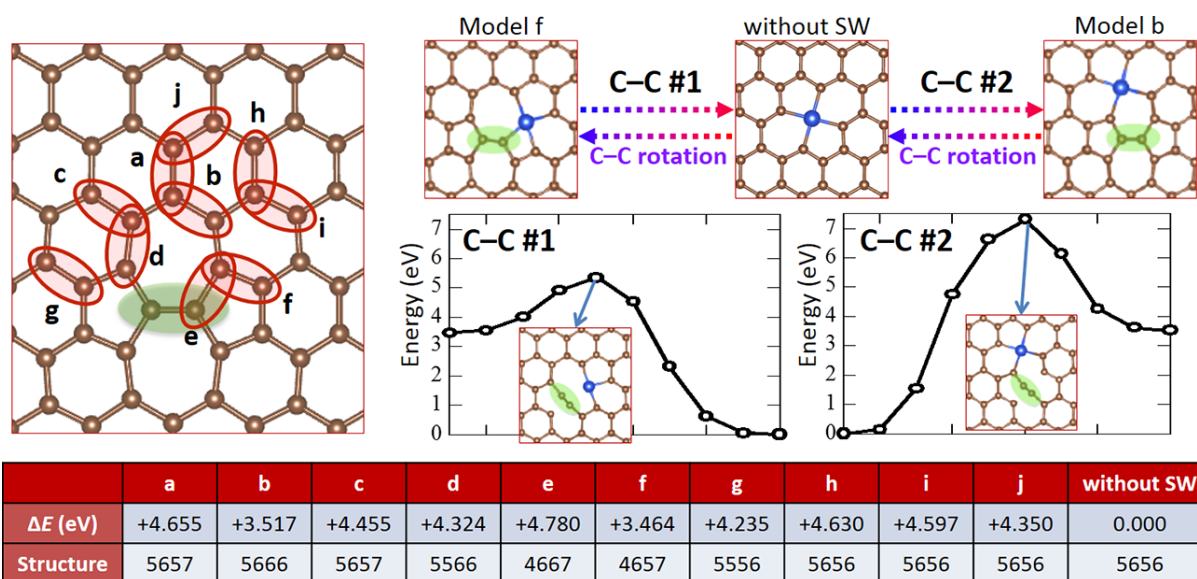


Figure A-8 DFT calculation for double vacancy

When a metal atom substitute two C atom at the positions indicated by the red rings, it forms four coordinated structures with the neighboring C atoms. We compared the energy difference ΔE between the structures with and without Stone-Wales (SW) defects. The table shows ΔE data for Cu at double vacancy, and energy diagrams of C–C rotations #1 and #2. As described in section 3-3, the energy barrier was smaller for C–C rotation #1 than #2; however, both rotations required higher energy at double vacancy than at single vacancy, because of the larger distance between the rotating C atoms and Cu atom.

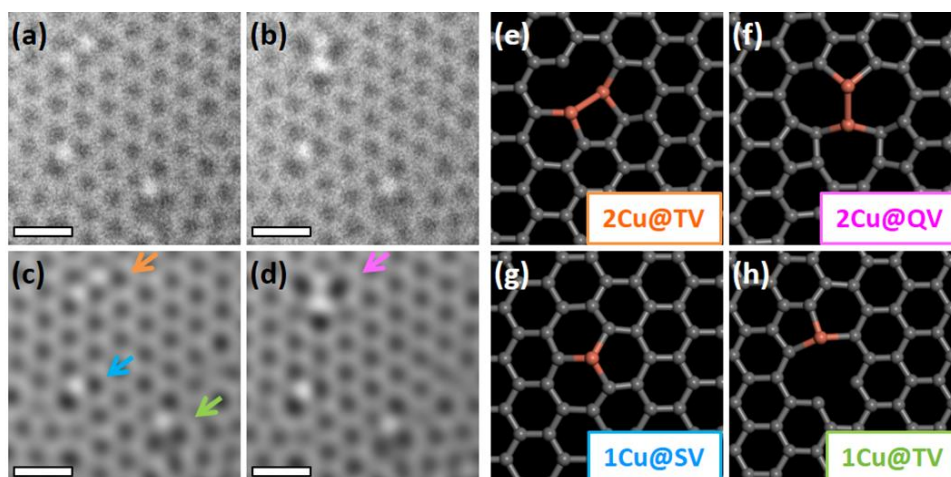


Figure A-9 Transformation of Cu dimer

(a), (b) Consecutive TEM images. (c), (d) Low-pass filtered images of (a) and (b). (e-h) atomic models of Cu atoms in graphene vacancies (SV: single vacancy, TV: tri-vacancy, QV: quad-vacancy) shown in (a-d). Metal dimers and trimers rotated more frequently than single atoms. Scale bars: 0.5 nm.

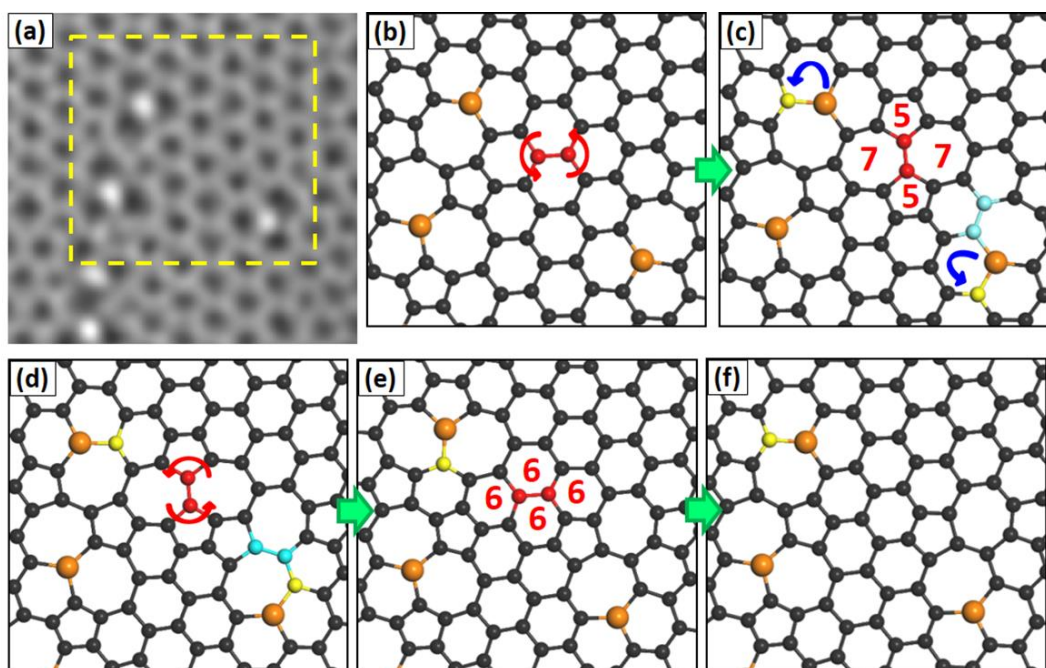


Figure A-10 Formation and mending of SW defects

(a) TEM image taken ~1 min after Fig. 3-5(b). The atomic model of yellow box area is shown in (b). (c)–(f) Atomic models of the observed transformations. C–Cu rotations were repeatedly occurred, possibly promoted via nearby C–C rotations (rotated atoms are highlighted in red and light blue). Orange balls present Cu, while C atoms in C–Cu rotation are highlighted in yellow.

Cu-mediated mending of graphene nanopores (cf. Chapter4)

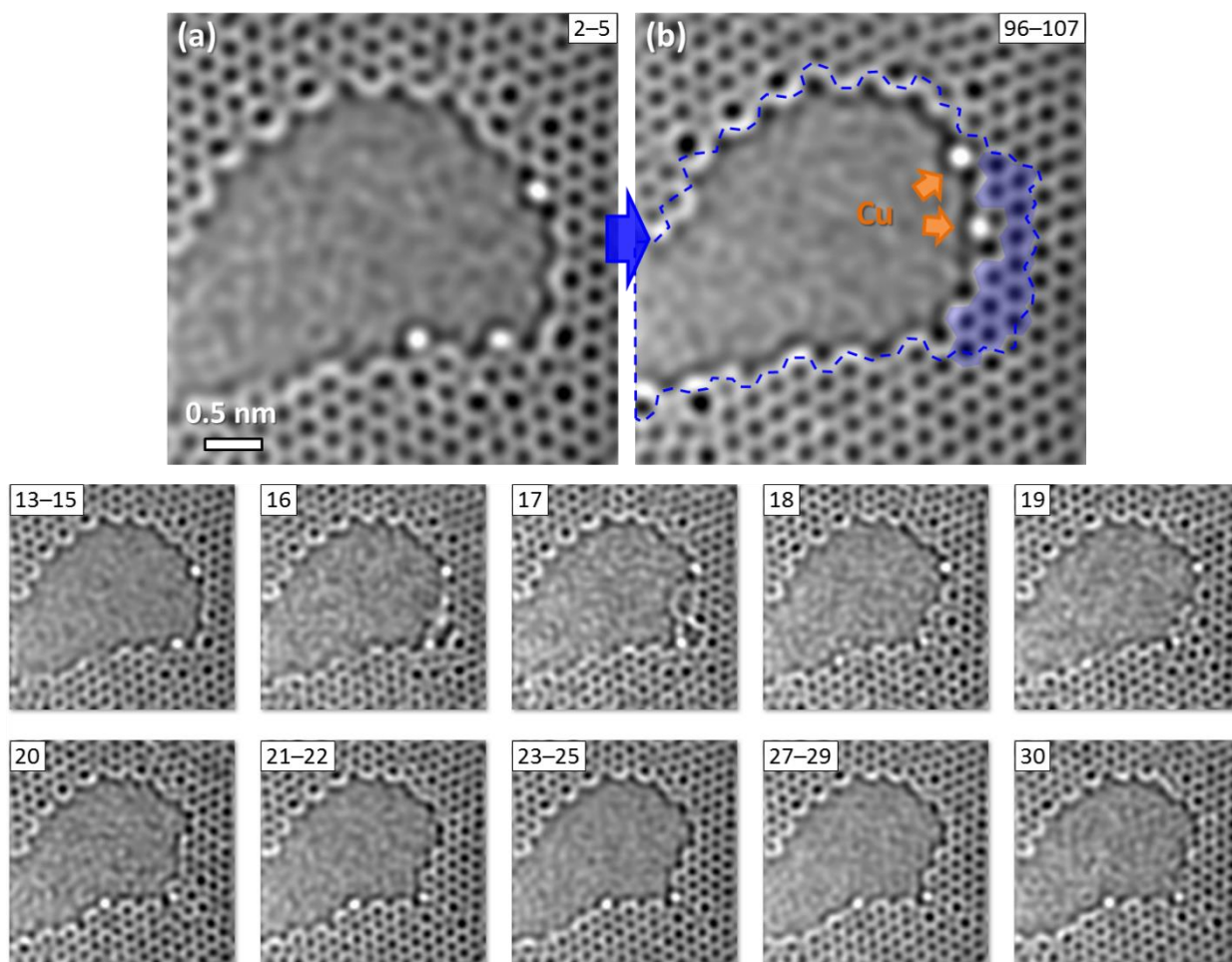


Figure A-11 Cu-mediated mending at 150 °C and current density $j = 250 \text{ A/cm}^2$

Low-pass filtered TEM images taken (a) before and (b) after the mending. The inset numbers indicate frame time. In this case, C atoms at first constructed chain-like structure, as shown in frame 17, and then reconstructed into honeycomb structure of graphene.

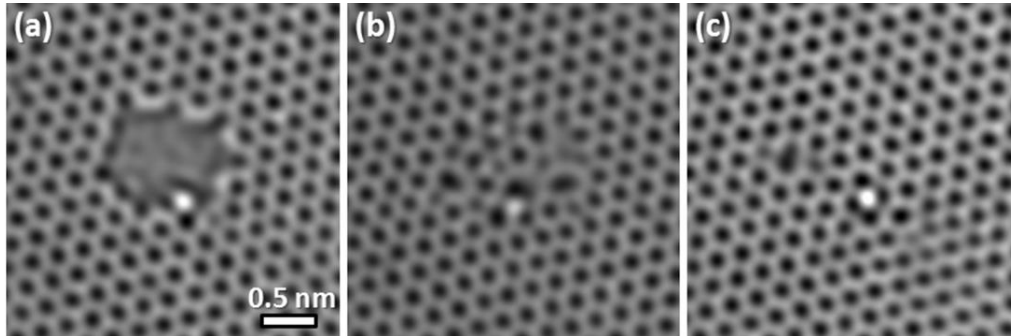


Figure A-12 Mending of small nanopore at 300 °C and current density $j = 250 \text{ A/cm}^2$

TEM images of (a) a graphene nanopore, (b) mended but defective graphene, and (c) mended graphene with less defects. Between panels (b) and (c), many SW defects were mended via repeated C–C rotations. We often observed mending of small nanopores ($< \sim 1 \text{ nm}$) into almost perfect graphene.

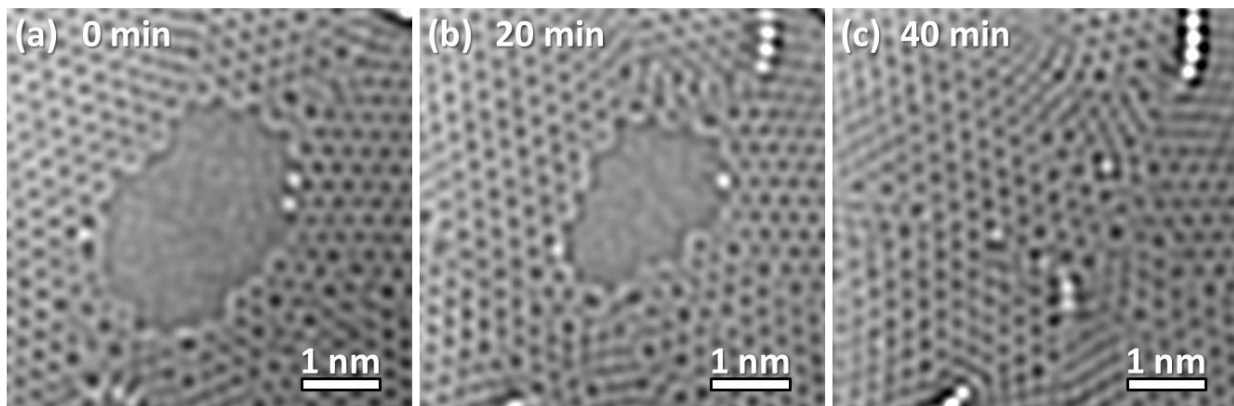


Figure A-13 Mending of nanopore at 150 °C without continuous electron irradiation

In contrast to other cases (Figs. 4-2, A-11 and A-12), we turned off the electron beam and took TEM images every 10 min. Larger nanopore was also mended without continuous electron irradiation, but it might be promoted by a short time electron irradiation while taking images.

List of Figures and Tables

Figures

Figure 1-1 Graphene isolation and its structure	2
Figure 1-2 Effective utilization of defects in graphene	4
Figure 1-3 Atomic-resolution imaging of graphene in an electron microscope	5
Figure 1-4 Roll-based production of graphene [11]	6
Figure 1-5 Single-atom spectroscopy at graphene edge [99].	7
Figure 1-6 Energy-transfer and defect formations in graphene.....	9
Figure 1-7 Decrease of knock-on energy threshold due to curvature in CNTs [110].....	13
Figure 1-8 Typical point defects [123]	13
Figure 1-9 Engineering nanocarbon materials by electron irradiation	14
Figure 1-10 Graphene defect mending or growth under electron irradiation.....	15
Figure 1-11 Metal mediated graphene etching [155]	18
Figure 1-12 Schematics of metal atoms in/on graphene	21
Figure 2-1 Spatial resolution and aberration corrector	23
Figure 2-2 Illumination systems of TEM and STEM.....	25
Figure 2-3 Simulated TEM images	26
Figure 2-4 Intensity in ADF-STEM images	28
Figure 2-5 Diffraction pattern of graphene [167]	29
Figure 2-6 Dark-field TEM	30
Figure 2-7 DF-TEM, TEM and ADF-STEM images of graphene	32
Figure 2-8 EEL spectra of C and Cu	34
Figure 2-9 Conservation of energy and momentum during elastic scattering.....	36
Figure 2-10 Binding energies of substitutional metal atoms in graphene [113].....	37
Figure 2-11 Energy transfer to C and its scattering cross section	39
Figure 2-12 Energy transfer to C, Cu and Pt from 80 keV incident electrons	40
Figure 2-13 Photographs of CVD equipment for graphene growth	43

Figure 2-14 Schematic of graphene transfer processes	44
Figure 2-15 PMMA coating and removal of extra graphene	45
Figure 2-16 Etching of Cu by $(\text{NH}_4)_2\text{S}_2\text{O}_8$ solution.....	46
Figure 2-17 Transfer onto TEM grids	47
Figure 2-18 Transfer onto <i>in situ</i> heating chips	48
Figure 2-19 Graphene before and after heating	50
Figure 2-20 Particle size difference on single- and double-layer graphene.....	52
Figure 3-1 Selecting observation areas	55
Figure 3-2 STEM-EELS data for Si and Cu	56
Figure 3-3 Cu atoms embedded in graphene	59
Figure 3-4 Cu sites in graphene	59
Figure 3-5 Reconstruction of graphene.....	61
Figure 3-6 Reconstruction of graphene.....	61
Figure 3-7 Selected snapshots of grain rotation.....	63
Figure 3-8 TEM images of the typical transformations	64
Figure 3-9 Comparison between three types of bond rotations	65
Figure 3-10 Energy required for the bond rotations.....	66
Figure 3-11 Analysis and averaged lifetimes of typical structures	68
Figure 3-12 Lifetime under electron irradiation	70
Figure 3-13 Binding energy between metal and C atoms	72
Figure 4-1 Different configurations of Cu and Pt atoms.....	76
Figure 4-2 (i) Cu-mediated mending and (ii) Pt-mediated etching.....	78
Figure 5-1 Observation of carbyne with Pt atoms.	84
Figure 5-2 Cu-terminated carbyne	85
Figure 6-1 STEM images of copper oxide on a graphene sheet	91
Figure 6-2 STEM-EELS analysis of 2D copper oxide on a graphene sheet.....	92
Figure 6-3 Distance between neighboring Cu atoms in 2D copper oxide	93
Figure 6-4 Bulk Cu_2O and 2D copper oxide.....	94
Figure 6-5 2D copper oxide, pure copper and copper carbide.....	95

Figure 6-6 Comparison between experiment and image simulation	96
Figure 6-7 Energy diagram of transformation between CuO and Cu.....	97
Figure 6-8 Molecular dynamics simulation of 2D cluster on graphene	98

List of Tables

Table 2-1 Energy transfer E_t	37
---------------------------------------	----

Figures in Appendix

Figure A-1 Measurement of detector angle for ADF-STEM.....	102
Figure A-2 TEM-EELS analysis of graphene on an <i>in situ</i> heating chip	103
Figure A-3 STEM-EELS analysis of graphene on <i>in situ</i> heating chip.....	103
Figure A-4 STEM-EELS analysis of graphene on Mo grid	104
Figure A-5 STEM-EELS analysis of Pt-deposited graphene	104
Figure A-6 Comparison between Cu-CVD and Ni-CVD graphene	105
Figure A-7 DFT calculation of energy diagram of C–Cu rotation	106
Figure A-8 DFT calculation for double vacancy	107
Figure A-9 Transformation of Cu dimer.....	108
Figure A-10 Formation and mending of SW defects.....	108
Figure A-11 Cu-mediated mending at 150 °C and current density $j = 250 \text{ A/cm}^2$	109
Figure A-12 Mending of small nanopore at 300 °C and current density $j = 250 \text{ A/cm}^2$	110
Figure A-13 Mending of nanopore at 150 °C without continuous electron irradiation..	110

List of Abbreviations

1D	one-dimensional
2D	two-dimensional
3D	three-dimensional
AFM	atomic force microscopy
ADF	annular dark field
BF	bright field
CNT	carbon nanotube
CVD	chemical vapor deposition
DF	dark-field
DFT	density functional theory
DI	deionized
EELS	electron energy loss spectroscopy
FEG	field emission electron gun
FFT	fast Fourier transform
h-BN	hexagonal boron nitride
MD	molecular dynamics
NP	nanoparticle
PET	polyethylene terephthalate
PMMA	poly(methyl methacrylate)
RT	room temperature
SEM	scanning electron microscopy
STEM	scanning transmission electron microscopy
STM	scanning tunneling microscopy
SW	Stone-Wales
TEM	transmission electron microscopy

List of Publications

Scientific papers

- [1] E. Kano, D. G. Kvashnin, S. Sakai, L. A. Chernozatonskii, P. B. Sorokin, A. Hashimoto, and M. Takeguchi, “One-atom-thick 2D copper oxide on graphene,” *Nanoscale*, accepted.
- [2] E. Kano, A. Hashimoto, and M. Takeguchi, “Opposite effects of Cu and Pt atoms on graphene edges,” *Appl. Phys. Express*, vol. 10, p. 25104, 2017.
- [3] E. Kano, A. Hashimoto, T. Kaneko, N. Tajima, T. Ohno, and M. Takeguchi, “Interactions between C and Cu atoms in single-layer graphene: direct observation and modelling,” *Nanoscale*, vol. 8, pp. 529–535, 2016.
- [4] E. Kano, M. Takeguchi, J. Fujita, and A. Hashimoto, “Direct observation of Pt-terminating carbyne on graphene,” *Carbon*, vol. 80, pp. 382–386, Dec. 2014.
- [5] S. M. Shinde, E. Kano, G. Kalita, M. Takeguchi, A. Hashimoto, and M. Tanemura, “Grain structures of nitrogen-doped graphene synthesized by solid source-based chemical vapor deposition,” *Carbon*, vol. 96, pp. 448–453, 2016.
- [6] K. Murakami, S. Tanaka, A. Hirukawa, T. Hiyama, T. Kuwajima, E. Kano, M. Takeguchi, and J. I. Fujita, “Direct synthesis of large area graphene on insulating substrate by gallium vapor-assisted chemical vapor deposition,” *Appl. Phys. Lett.*, vol. 106, p. 93112, 2015.
- [7] T. Nishijima, R. Ueki, E. Kano, and J. Fujita, “In-situ observation of current-pulse-induced curling of graphene edges and carbon-cages production,” *Jpn. J. Appl. Phys.*, vol. 51, p. 06FD20, Jun. 2012.

Conference proceedings

- [1] E. Kano, A. Hashimoto, and M. Takeguchi, “Cu atoms reknit the graphene structures,” *Microsc. Microanal.*, vol. 21, pp. 741–742, 2015.
- [2] E. Kano, A. Hashimoto, and M. Takeguchi, “In-situ TEM observation of Pt-terminating carbyne on graphene,” *Microsc. Microanal.*, vol. 20, pp. 1742–1743, 2014.

Conference awards

Sep. 2014	Young Scientist Presentation Award The 75th Autumn Meeting of The Japan Society of Applied Physics
Sep. 2014	IMC 2014 Scholarship 18 th International Microscopy Congress
Aug. 2014	M&M Student Awards Microscopy & Microanalysis 2014 Meeting
Jan. 2014	Excellent Student Poster Award CENIDE-CNMM-TIMS Joint Symposium on Interdisciplinary Nano-Science and Technology
Dec. 2012	Excellent Student Poster Award The 4th Tsukuba-Hsinchu Joint Symposium on Interdisciplinary Nano-Science and Technology

Conference presentations

International conferences

- [1] E. Kano, A. Hashimoto, M. Takeguchi, “Cu atoms at the edge of graphene” Asian Graphene Forum, Singapore, Singapore, Mar. 2017.
- [2] E. Kano, D. G. Kvashnin, S. Sakai, L. A. Chernozatonskii, P. B. Sorokin, A. Hashimoto, and M. Takeguchi, “One-atom thick two dimensional copper sheets on graphene” Microscopical Society of Canada 43rd Annual Meeting, Edmonton, Canada, Jun. 2016.
- [3] E. Kano, A. Hashimoto, M. Takeguchi, “In situ TEM observation of Cu-doped graphene” The 2nd East-Asia Microscopy Conference, Himeji, Japan, Nov. 2015.
- [4] E. Kano, A. Hashimoto, M. Takeguchi, “Cu Atoms Reknit the Graphene Structures” Microscopy & Microanalysis 2015 Meeting, Portland, USA, Aug. 2015.
- [5] E. Kano, A. Hashimoto, M. Takeguchi, “Pt-terminating Carbyne Observed by Aberration-Corrected TEM” 18th International Microscopy Congress, Sep. 2014.
- [6] E. Kano, A. Hashimoto, M. Takeguchi, “In-situ TEM Observation of Pt-terminating Carbyne on Graphene” Microscopy & Microanalysis 2014 Meeting, Aug. 2014.

Domestic conferences

- [7] E. Kano, A. Hashimoto, M. Takeguchi, “High-resolution STEM observation of Cu clusters on graphene” Tsukuba Global Science Week, Tsukuba, Japan, Sep. 2016.
- [8] 狩野 絵美、橋本 綾子、竹口 雅樹、” Cu 原子によるグラフェン再構成過程その場 TEM 観察”、共用・計測合同シンポジウム 2016、2016 年 3 月
- [9] 狩野 絵美、橋本 綾子、竹口 雅樹、”2 層グラフェンに形成したナノポアのエッジ構造”、第 63 回応用物理学会 春季学術講演会、21p-H137-2、2016 年 3 月
- [10] 狩野 絵美、橋本 綾子、竹口 雅樹、”グラフェン中 Cu 原子のその場 TEM 観察”、超高分解能顕微鏡法分科会 合宿研究会、2015 年 9 月
- [11] 狩野 絵美、橋本 綾子、竹口 雅樹、”2 層グラフェンへの安定な細孔の形成”、第 76 回応用物理学会 秋季学術講演会、15p-4E-3、2015 年 9 月
- [12] E. Kano, A. Hashimoto, M. Takeguchi, “In-situ TEM Observation of Cu Atoms in Graphene” NIMS Conference 2015, Jul. 2015.
- [13] 狩野 絵美、橋本 綾子、竹口 雅樹、”グラフェン空孔欠陥中の Cu 原子の面内拡散その場 TEM 観察”、日本顕微鏡学会 第 71 回学術講演会、14amC_M7-07、2015 年 5 月
- [14] 狩野 絵美、橋本 綾子、竹口 雅樹、” グラフェンのステップ成長のその場 TEM 観察”、第 62 回応用物理学会 春季学術講演会、2015 年 3 月
- [15] 狩野 絵美、”収差補正電子顕微鏡によるグラフェン上の白金終端カルビンのその場観察/実動環境対応物理分析 TEM”、SAT テクノロジー・ショーケース 2015、2015 年 1 月
- [16] 狩野 絵美、橋本 綾子、竹口 雅樹、”グラフェン上の金属原子のその場 TEM 観察”、第 75 回応用物理学会 秋季学術講演会、2014 年 9 月
- [17] 狩野 絵美、橋本 綾子、竹口 雅樹、”グラフェン上白金単原子の球面収差補正 TEM 観察”、日本顕微鏡学会 第 70 回記念学術講演会、2014 年 5 月
- [18] 狩野 絵美、橋本 綾子、竹口 雅樹、”白金/グラフェン上での炭素原子鎖形成その場観察”、日本顕微鏡学会 第 70 回記念学術講演会、2014 年 5 月

References

- [1] K. S. Novoselov, A. K. Geim, S. V. Morozov, D. Jiang, Y. Zhang, S. V. Dubonos, I. V. Grigorieva, and A. A. Firsov, “Electric Field Effect in Atomically Thin Carbon Films,” *Science*, vol. 306, no. 5696, pp. 666–669, Oct. 2004.
- [2] A. K. Geim and K. S. Novoselov, “The rise of graphene,” *Nat. Mater.*, vol. 6, no. 3, pp. 183–91, Mar. 2007.
- [3] S. Iijima, “Helical microtubules of graphitic carbon,” *Nature*, vol. 354, no. 6348, pp. 56–58, Nov. 1991.
- [4] H. W. Kroto, J. R. Heath, S. C. O’Brien, R. F. Curl, and R. E. Smalley, “C₆₀: Buckminsterfullerene,” *Nature*, vol. 318, no. 14, pp. 162–163, 1985.
- [5] T. Ohta, “Controlling the Electronic Structure of Bilayer Graphene,” *Science*, vol. 313, no. 5789, pp. 951–954, Aug. 2006.
- [6] P. K. Ang, S. Wang, Q. Bao, J. T. L. Thong, and K. P. Loh, “High-Throughput Synthesis of Graphene by Intercalation–Exfoliation of Graphite Oxide and Study of Ionic Screening in Graphene Transistor,” *ACS Nano*, vol. 3, no. 11, pp. 3587–3594, Nov. 2009.
- [7] C. Y. Su, Y. Xu, W. Zhang, J. Zhao, A. Liu, X. Tang, C. H. Tsai, Y. Huang, and L.-J. Li, “Highly efficient restoration of graphitic structure in graphene oxide using alcohol vapors,” *ACS Nano*, vol. 4, no. 9, pp. 5285–5292, 2010.
- [8] O. V Yazyev and S. G. Louie, “Electronic transport in polycrystalline graphene,” *Nat. Mater.*, vol. 9, no. 10, pp. 806–809, Oct. 2010.
- [9] A. W. Tsen, L. Brown, M. P. Levendorf, F. Ghahari, P. Y. Huang, R. W. Havener, C. S. Ruiz-Vargas, D. A. Muller, P. Kim, and J. Park, “Tailoring Electrical Transport Across Grain Boundaries in Polycrystalline Graphene,” *Science*, vol. 336, no. 6085, pp. 1143–1146, Jun. 2012.
- [10] P. Willke, J. A. Amani, A. Sinterhauf, S. Thakur, T. Kotzot, T. Druga, S. Weikert, K. Maiti, H. Hofsäss, and M. Wenderoth, “Doping of Graphene by Low-Energy Ion Beam Implantation: Structural, Electronic, and Transport Properties,” *Nano Lett.*, vol. 15, no. 8, pp. 5110–5115, Aug. 2015.
- [11] S. Bae, H. Kim, Y. Lee, X. Xu, J.-S. Park, Y. Zheng, J. Balakrishnan, T. Lei, H. Ri Kim, Y. Il Song, Y.-J. Kim, K. S. Kim, B. Özyilmaz, J.-H. Ahn, B. H. Hong, and S. Iijima, “Roll-to-roll production of 30-inch graphene films for transparent electrodes,” *Nat. Nanotechnol.*, vol. 5, no. 8, pp. 574–578, Aug. 2010.
- [12] X. Li, Y. Zhu, W. Cai, M. Borysiak, B. Han, D. Chen, R. D. Piner, L. Colombo, and R. S. Ruoff, “Transfer of Large-Area Graphene Films for High-Performance Transparent Conductive Electrodes,” *Nano Lett.*, vol. 9, no. 12, pp. 4359–4363, Dec. 2009.

- [13] K. S. Kim, Y. Zhao, H. Jang, S. Y. Lee, J. M. Kim, K. S. Kim, J.-H. Ahn, P. Kim, J.-Y. Choi, and B. H. Hong, "Large-scale pattern growth of graphene films for stretchable transparent electrodes," *Nature*, vol. 457, no. 7230, pp. 706–710, Feb. 2009.
- [14] A. V Zaretski, H. Moetazed, C. Kong, E. J. Sawyer, S. Savagatrup, E. Valle, T. F. O'Connor, A. D. Printz, and D. J. Lipomi, "Metal-assisted exfoliation (MAE): green, roll-to-roll compatible method for transferring graphene to flexible substrates.," *Nanotechnology*, vol. 26, no. 4, p. 45301, 2015.
- [15] E. Yoo, T. Okata, T. Akita, M. Kohyama, J. Nakamura, and I. Honma, "Enhanced Electrocatalytic Activity of Pt Subnanoclusters on Graphene Nanosheet Surface," *Nano Lett.*, vol. 9, no. 6, pp. 2255–2259, Jun. 2009.
- [16] B. Seger and P. V. Kamat, "Electrocatalytically Active Graphene-Platinum Nanocomposites. Role of 2-D Carbon Support in PEM Fuel Cells," *J. Phys. Chem. C*, vol. 113, no. 19, pp. 7990–7995, May 2009.
- [17] K. S. Subrahmanyam, A. K. Manna, S. K. Pati, and C. N. R. Rao, "A study of graphene decorated with metal nanoparticles," *Chem. Phys. Lett.*, vol. 497, no. 1–3, pp. 70–75, Sep. 2010.
- [18] E. Yoo, T. Okada, T. Akita, M. Kohyama, I. Honma, and J. Nakamura, "Sub-nano-Pt cluster supported on graphene nanosheets for CO tolerant catalysts in polymer electrolyte fuel cells," *J. Power Sources*, vol. 196, no. 1, pp. 110–115, Jan. 2011.
- [19] I. Janowska, M.-S. Moldovan, O. Ersen, H. Bulou, K. Chizari, M. J. Ledoux, and C. Pham-Huu, "High temperature stability of platinum nanoparticles on few-layer graphene investigated by In Situ high resolution transmission electron microscopy," *Nano Res.*, vol. 4, no. 5, pp. 511–521, May 2011.
- [20] R. Sibirian and J. Nakamura, "Formation Process of Pt Subnano-Clusters on Graphene Nanosheets," *J. Phys. Chem. C*, vol. 116, no. 43, pp. 22947–22953, Nov. 2012.
- [21] Y. Borodko, P. Ercius, V. Pushkarev, C. Thompson, and G. Somorjai, "From Single Pt Atoms to Pt Nanocrystals: Photoreduction of Pt 2+ Inside of a PAMAM Dendrimer," *J. Phys. Chem. Lett.*, vol. 3, no. 2, pp. 236–241, Jan. 2012.
- [22] D.-H. Lim and J. Wilcox, "Mechanisms of the Oxygen Reduction Reaction on Defective Graphene-Supported Pt Nanoparticles from First-Principles," *J. Phys. Chem. C*, vol. 116, no. 5, pp. 3653–3660, Feb. 2012.
- [23] J. C. Yang, M. W. Small, R. V. Grieshaber, and R. G. Nuzzo, "Recent developments and applications of electron microscopy to heterogeneous catalysis," *Chem. Soc. Rev.*, vol. 41, no. 24, pp. 8179–8194, 2012.
- [24] Y. Borodko, P. Ercius, D. Zherebetsky, Y. Wang, Y. Sun, and G. A. Somorjai, "From Single Atoms to Nanocrystals: Photoreduction of [PtCl₆]²⁻ in Aqueous and Tetrahydrofuran Solutions of PVP," *Phys. Chem. C*, vol. 117, pp. 26667–26674, 2013.
- [25] R. Sibirian, T. Kondo, and J. Nakamura, "Size Control to a Sub-Nanometer Scale in Platinum Catalysts on Graphene," *J. Phys. Chem. C*, vol. 117, no. 7, pp. 3635–3645, Feb. 2013.

- [26] T. Tomai, Y. Kawaguchi, S. Mitani, and I. Honma, "Pt sub-nano/nanoclusters stabilized at the edge of nanographene sheets and their catalytic performance," *Electrochim. Acta*, vol. 92, pp. 421–426, Mar. 2013.
- [27] S. Sun, G. Zhang, N. Gauquelin, N. Chen, J. Zhou, S. Yang, W. Chen, X. Meng, D. Geng, M. N. Banis, R. Li, S. Ye, S. Knights, G. A. Botton, T.-K. Sham, and X. Sun, "Single-atom Catalysis Using Pt/Graphene Achieved through Atomic Layer Deposition," *Sci. Rep.*, vol. 3, p. 1775, May 2013.
- [28] Y. Li, F. Huang, J. Chen, T. Mo, S. Li, F. Wang, and S. Feng, "A High Performance Enzyme-Free Glucose Sensor Based on the," *Int. J. Electrochem. Sci.*, vol. 8, pp. 6332–6342, 2013.
- [29] Y. Lee, S. Lee, Y. Hwang, and Y.-C. Chung, "Modulating magnetic characteristics of Pt embedded graphene by gas adsorption (N₂, O₂, NO₂, SO₂)," *Appl. Surf. Sci.*, vol. 289, no. 2, pp. 445–449, Jan. 2014.
- [30] K. S. Novoselov, D. Jiang, F. Schedin, T. J. Booth, V. V Khotkevich, S. V Morozov, and A. K. Geim, "Two-dimensional atomic crystals," *Proc. Natl. Acad. Sci.*, vol. 102, no. 30, pp. 10451–10453, Jul. 2005.
- [31] J. Kotakoski and J. C. Meyer, "Mechanical properties of polycrystalline graphene based on a realistic atomistic model," *Phys. Rev. B*, vol. 85, no. 19, p. 195447, May 2012.
- [32] S.-M. Lee, J.-H. Kim, and J.-H. Ahn, "Graphene as a flexible electronic material: mechanical limitations by defect formation and efforts to overcome," *Mater. Today*, vol. 18, no. 6, pp. 336–344, Jul. 2015.
- [33] J. Lahiri, Y. Lin, P. Bozkurt, I. I. Oleynik, and M. Batzill, "An extended defect in graphene as a metallic wire," *Nat. Nanotechnol.*, vol. 5, no. 5, pp. 326–329, May 2010.
- [34] J. Cai, P. Ruffieux, R. Jaafar, M. Bieri, T. Braun, S. Blankenburg, M. Muoth, A. P. Seitsonen, M. Saleh, X. Feng, K. Müllen, and R. Fasel, "Atomically precise bottom-up fabrication of graphene nanoribbons," *Nature*, vol. 466, no. 7305, pp. 470–473, Jul. 2010.
- [35] T. Shimizu, J. Haruyama, D. C. Marcano, D. V Kosinkin, J. M. Tour, K. Hirose, and K. Suenaga, "Large intrinsic energy bandgaps in annealed nanotube-derived graphene nanoribbons," *Nat. Nanotechnol.*, vol. 6, no. 1, pp. 45–50, Jan. 2011.
- [36] H. Terrones, R. Lv, M. Terrones, and M. S. Dresselhaus, "The role of defects and doping in 2D graphene sheets and 1D nanoribbons," *Reports Prog. Phys.*, vol. 75, no. 6, p. 62501, Jun. 2012.
- [37] L. Ma, J. Wang, and F. Ding, "Recent Progress and Challenges in Graphene Nanoribbon Synthesis," *ChemPhysChem*, vol. 14, no. 1, pp. 47–54, Jan. 2013.
- [38] P. B. Sorokin and L. A. Chernozatonskii, "Graphene-based semiconductor nanostructures," *Physics-Uspekhi*, vol. 56, no. 2, pp. 105–122, Feb. 2013.
- [39] J. Lu, P. S. E. Yeo, C. K. Gan, P. Wu, and K. P. Loh, "Transforming C₆₀ molecules into graphene quantum dots," *Nat. Nanotechnol.*, vol. 6, no. 4, pp. 247–252, 2011.

- [40] W. Zhou, S. J. Pennycook, and J.-C. Idrobo, "Probing the electronic structure and optical response of a graphene quantum disk supported on monolayer graphene," *J. Phys. Condens. Matter*, vol. 24, no. 31, p. 314213, Aug. 2012.
- [41] J. Peng, W. Gao, B. K. Gupta, Z. Liu, R. Romero-Aburto, L. Ge, L. Song, L. B. Alemany, X. Zhan, G. Gao, S. A. Vithayathil, B. A. Kaiparettu, A. a Marti, T. Hayashi, J. Zhu, and P. M. Ajayan, "Graphene Quantum Dots Derived from Carbon Fibers," *Nano Lett.*, vol. 12, no. 2, pp. 844–849, Feb. 2012.
- [42] H. Bayley, "Nanotechnology: Holes with an edge," *Nature*, vol. 467, no. 7312, pp. 164–165, Sep. 2010.
- [43] S. Garaj, W. Hubbard, A. Reina, J. Kong, D. Branton, and J. A. Golovchenko, "Graphene as a subnanometre trans-electrode membrane," *Nature*, vol. 467, no. 7312, pp. 190–193, 2010.
- [44] C. A. Merchant, K. Healy, M. Wanunu, V. Ray, N. Peterman, J. Bartel, M. D. Fischbein, K. Venta, Z. Luo, A. T. C. Johnson, and M. Drndić, "DNA Translocation through Graphene Nanopores," *Nano Lett.*, vol. 10, no. 8, pp. 2915–2921, Aug. 2010.
- [45] G. F. Schneider, S. W. Kowalczyk, V. E. Calado, G. Pandraud, H. W. Zandbergen, L. M. K. Vandersypen, and C. Dekker, "DNA Translocation through Graphene Nanopores," *Nano Lett.*, vol. 10, no. 8, pp. 3163–3167, Aug. 2010.
- [46] G. F. Schneider, Q. Xu, S. Hage, S. Luik, J. N. H. Spoor, S. Malladi, H. Zandbergen, and C. Dekker, "Tailoring the hydrophobicity of graphene for its use as nanopores for DNA translocation," *Nat. Commun.*, vol. 4, p. 2619, 2013.
- [47] S. Nam, I. Choi, C. Fu, K. Kim, S. Hong, Y. Choi, A. Zettl, and L. P. Lee, "Graphene Nanopore with a Self-Integrated Optical Antenna," *Nano Lett.*, vol. 14, pp. 5584–5589, 2014.
- [48] S. C. O'Hern, M. S. H. Boutilier, J.-C. Idrobo, Y. Song, J. Kong, T. Laoui, M. Atieh, and R. Karnik, "Selective Ionic Transport through Tunable Subnanometer Pores in Single-Layer Graphene Membranes," *Nano Lett.*, vol. 14, no. 3, pp. 1234–1241, Mar. 2014.
- [49] H. Arjmandi-Tash, L. A. Belyaeva, and G. F. Schneider, "Single molecule detection with graphene and other two-dimensional materials: nanopores and beyond," *Chem. Soc. Rev.*, vol. 45, pp. 476–493, 2015.
- [50] E. L. Bonome, R. Lepore, D. Raimondo, F. Cecconi, A. Tramontano, and M. Chinappi, "Multistep Current Signal in Protein Translocation through Graphene Nanopores," *J. Phys. Chem. B*, vol. 119, no. 18, pp. 5815–5823, May 2015.
- [51] K. A. Mahmoud, B. Mansoor, A. Mansour, and M. Khraisheh, "Functional graphene nanosheets: The next generation membranes for water desalination," *Desalination*, vol. 356, no. August 2016, pp. 208–225, Jan. 2015.
- [52] J. A. Rodríguez-Manzo, M. Puster, A. Nicolai, V. Meunier, and M. Drndić, "DNA Translocation in Nanometer Thick Silicon Nanopores," *ACS Nano*, vol. 9, no. 6, pp. 6555–6564, Jun. 2015.
- [53] S. P. Surwade, S. N. Smirnov, I. V. Vlassioug, R. R. Unocic, G. M. Veith, S. Dai, and S. M. Mahurin, "Water desalination using nanoporous single-layer graphene," *Nat. Nanotechnol.*, vol. 10, no. 5, pp. 459–464, Mar. 2015.

- [54] M. Taniguchi, "Selective Multidetector Using Nanopores," *Anal. Chem.*, vol. 87, pp. 188–199, 2015.
- [55] Y. Wang, Q. Yang, and Z. Wang, "The evolution of nanopore sequencing," *Front. Genet.*, vol. 5, no. DEC, pp. 1–20, Jan. 2015.
- [56] S. J. Heerema and C. Dekker, "Graphene nanodevices for DNA sequencing," *Nat. Nanotechnol.*, vol. 11, no. 2, pp. 127–136, 2016.
- [57] C. Yu, B. Zhang, F. Yan, J. Zhao, J. Li, L. Li, and J. Li, "Engineering nano-porous graphene oxide by hydroxyl radicals," *Carbon*, vol. 105, no. August, pp. 291–296, Aug. 2016.
- [58] R. C. Rollings, A. T. Kuan, and J. A. Golovchenko, "Ion selectivity of graphene nanopores," *Nat. Commun.*, vol. 7, p. 11408, Apr. 2016.
- [59] U. Heiz, A. Sanchez, S. Abbet, and W.-D. Schneider, "Catalytic Oxidation of Carbon Monoxide on Monodispersed Platinum Clusters: Each Atom Counts," *J. Am. Chem. Soc.*, vol. 121, no. 13, pp. 3214–3217, Apr. 1999.
- [60] R. Kou, Y. Shao, D. Wang, M. H. Engelhard, J. H. Kwak, J. Wang, V. V. Viswanathan, C. Wang, Y. Lin, Y. Wang, I. A. Aksay, and J. Liu, "Enhanced activity and stability of Pt catalysts on functionalized graphene sheets for electrocatalytic oxygen reduction," *Electrochem. Commun.*, vol. 11, no. 5, pp. 954–957, May 2009.
- [61] L.-S. Zhang, X.-Q. Liang, W.-G. Song, and Z.-Y. Wu, "Identification of the nitrogen species on N-doped graphene layers and Pt/NG composite catalyst for direct methanol fuel cell," *Phys. Chem. Chem. Phys.*, vol. 12, no. 38, p. 12055, Oct. 2010.
- [62] R. Imran Jafri, N. Rajalakshmi, and S. Ramaprabhu, "Nitrogen doped graphene nanoplatelets as catalyst support for oxygen reduction reaction in proton exchange membrane fuel cell," *J. Mater. Chem.*, vol. 20, no. 34, pp. 7114–7117, 2010.
- [63] T. Kondo, T. Suzuki, and J. Nakamura, "Nitrogen Doping of Graphite for Enhancement of Durability of Supported Platinum Clusters," *J. Phys. Chem. Lett.*, vol. 2, no. 6, pp. 577–580, Mar. 2011.
- [64] N. Kannari and J. Ozaki, "Formation of uniformly and finely dispersed nanoshells by carbonization of cobalt-coordinated oxine–formaldehyde resin and their electrochemical oxygen reduction activity," *Carbon*, vol. 50, no. 8, pp. 2941–2952, Jul. 2012.
- [65] Y. Li, W. Zhou, H. Wang, L. Xie, Y. Liang, F. Wei, J.-C. Idrobo, S. J. Pennycook, and H. Dai, "An oxygen reduction electrocatalyst based on carbon nanotube–graphene complexes," *Nat. Nanotechnol.*, vol. 7, no. 6, pp. 394–400, May 2012.
- [66] W. Zhou, J. Lee, J. Nanda, S. T. Pantelides, S. J. Pennycook, and J. Idrobo, "Atomically localized plasmon enhancement in monolayer graphene," *Nat. Nanotechnol.*, vol. 7, no. 3, pp. 161–165, Jan. 2012.
- [67] Y. Zhao, Y. Zhou, B. Xiong, J. Wang, X. Chen, R. O'Hayre, and Z. Shao, "Facile single-step preparation of Pt/N-graphene catalysts with improved methanol electrooxidation activity," *J. Solid State Electrochem.*, vol. 17, no. 4, pp. 1089–1098, Apr. 2013.

- [68] B. Xiong, Y. Zhou, Y. Zhao, J. Wang, X. Chen, R. O'Hayre, and Z. Shao, "The use of nitrogen-doped graphene supporting Pt nanoparticles as a catalyst for methanol electrocatalytic oxidation," *Carbon*, vol. 52, pp. 181–192, Feb. 2013.
- [69] Z. Hou, X. Wang, T. Ikeda, K. Terakura, M. Oshima, and M. Kakimoto, "Electronic structure of N-doped graphene with native point defects," *Phys. Rev. B*, vol. 87, no. 16, p. 165401, Apr. 2013.
- [70] X. Yang, A. Wang, B. Qiao, J. Li, J. Liu, and T. Zhang, "Single-Atom Catalysts: A New Frontier in Heterogeneous Catalysis," *Acc. Chem. Res.*, vol. 46, no. 8, pp. 1740–1748, Aug. 2013.
- [71] G. Luo, L. Liu, J. Zhang, G. Li, B. Wang, and J. Zhao, "Hole Defects and Nitrogen Doping in Graphene: Implication for Supercapacitor Applications," *ACS Appl. Mater. Interfaces*, vol. 5, pp. 11184–11193, 2013.
- [72] S. Stambula, N. Gauquelin, M. Bugnet, S. Gorantla, S. Turner, S. Sun, J. Liu, G. Zhang, X. Sun, and G. A. Botton, "Chemical Structure of Nitrogen-Doped Graphene with Single Platinum Atoms and Atomic Clusters as a Platform for the PEMFC Electrode," *J. Phys. Chem. C*, vol. 118, no. 8, pp. 3890–3900, Feb. 2014.
- [73] R.-X. Wang, J.-J. Fan, Y.-J. Fan, J.-P. Zhong, L. Wang, S.-G. Sun, and X.-C. Shen, "Platinum nanoparticles on porphyrin functionalized graphene nanosheets as a superior catalyst for methanol electrooxidation," *Nanoscale*, vol. 6, no. 24, pp. 14999–15007, Oct. 2014.
- [74] Y.-C. Lin, P.-Y. Teng, C.-H. Yeh, M. Koshino, P.-W. Chiu, and K. Suenaga, "Structural and Chemical Dynamics of Pyridinic-Nitrogen Defects in Graphene," *Nano Lett.*, vol. 15, no. 11, pp. 7408–7413, Nov. 2015.
- [75] C. M. Sims, A. A. Ponce, K. J. Gaskell, and B. W. Eichhorn, "CO tolerance of Pt and PtSn intermetallic electrocatalysts on synthetically modified reduced graphene oxide supports," *Dalt. Trans.*, vol. 44, no. 3, pp. 977–987, 2015.
- [76] Y. Song, R. Peng, D. K. Hensley, P. V. Bonnesen, L. Liang, Z. Wu, H. M. Meyer, M. Chi, C. Ma, B. G. Sumpter, and A. J. Rondinone, "High-Selectivity Electrochemical Conversion of CO₂ to Ethanol using a Copper Nanoparticle/N-Doped Graphene Electrode," *ChemistrySelect*, vol. 1, pp. 1–8, Sep. 2016.
- [77] D. Deng, K. S. Novoselov, Q. Fu, N. Zheng, Z. Tian, and X. Bao, "Catalysis with two-dimensional materials and their heterostructures," *Nat. Nanotechnol.*, vol. 11, no. 3, pp. 218–230, 2016.
- [78] M. Haider, S. Uhlemann, E. Schwan, and H. Rose, "Electron microscopy image enhanced," *Nature*, vol. 392, pp. 768–769, 1998.
- [79] P. W. Hawkes, "Aberration correction past and present," *Philos. Trans. R. Soc. A*, vol. 367, no. 1903, pp. 3637–3664, 2009.
- [80] J. C. Meyer, C. Kisielowski, R. Erni, M. D. Rossell, M. F. Crommie, and A. Zettl, "Direct Imaging of Lattice Atoms and Topological Defects in Graphene Membranes," *Nano Lett.*, vol. 8, no. 11, pp. 3582–3586, Nov. 2008.

- [81] M. H. Gass, U. Bangert, A. L. Bleloch, P. Wang, R. R. Nair, and A. K. Geim, “Free-standing graphene at atomic resolution,” *Nat. Nanotechnol.*, vol. 3, no. 11, pp. 676–681, Nov. 2008.
- [82] X. Li, W. Cai, J. An, S. Kim, J. Nah, D. Yang, R. Piner, A. Velamakanni, I. Jung, E. Tutuc, S. K. Banerjee, L. Colombo, and R. S. Ruoff, “Large-Area Synthesis of High-Quality and Uniform Graphene Films on Copper Foils,” *Science*, vol. 324, no. 5932, pp. 1312–1314, Jun. 2009.
- [83] W. Regan, N. Alem, B. Alemán, B. Geng, Ç. Ö. Girit, L. Maserati, F. Wang, M. Crommie, and A. Zettl, “A direct transfer of layer-area graphene,” *Appl. Phys. Lett.*, vol. 96, no. 11, p. 113102, 2010.
- [84] Y.-C. Lin, C. Jin, J.-C. Lee, S.-F. Jen, K. Suenaga, and P.-W. Chiu, “Clean Transfer of Graphene for Isolation and Suspension,” *ACS Nano*, vol. 5, no. 3, pp. 2362–2368, Mar. 2011.
- [85] Y.-C. Lin, C.-C. Lu, C.-H. Yeh, C. Jin, K. Suenaga, and P.-W. Chiu, “Graphene Annealing: How Clean Can It Be?,” *Nano Lett.*, vol. 12, no. 1, pp. 414–419, Jan. 2012.
- [86] A. Oberlin, M. Endo, and T. Koyama, “Filamentous growth of carbon through benzene decomposition,” *J. Cryst. Growth*, vol. 32, no. 3, pp. 335–349, Mar. 1976.
- [87] A. Hashimoto, K. Suenaga, A. Gloter, K. Urita, and S. Iijima, “Direct evidence for atomic defects in graphene layers,” *Nature*, vol. 430, no. 7002, pp. 870–873, Aug. 2004.
- [88] K. Hata, “Water-Assisted Highly Efficient Synthesis of Impurity-Free Single-Walled Carbon Nanotubes,” *Science*, vol. 306, no. 5700, pp. 1362–1364, Nov. 2004.
- [89] T. Matsumoto, T. Komatsu, H. Nakano, K. Arai, Y. Nagashima, E. Yoo, T. Yamazaki, M. Kijima, H. Shimizu, Y. Takasawa, and J. Nakamura, “Efficient usage of highly dispersed Pt on carbon nanotubes for electrode catalysts of polymer electrolyte fuel cells,” *Catal. Today*, vol. 90, no. 3–4, pp. 277–281, Jul. 2004.
- [90] J. Tang, G. Yang, Q. Zhang, A. Parhat, B. Maynor, J. Liu, L.-C. Qin, O. Zhou, D. Liu, L. C. Din, and O. Zhou, “Rapid and reproducible fabrication of carbon nanotube AFM probes by dielectrophoresis,” *Nano Lett.*, vol. 5, no. 1, pp. 11–14, Jan. 2005.
- [91] T. Kamino, “In situ high temperature TEM observation of interaction between multi-walled carbon nanotube and in situ deposited gold nano-particles,” *J. Electron Microsc.*, vol. 54, no. 5, pp. 461–465, Sep. 2005.
- [92] D. Takagi, Y. Homma, H. Hibino, S. Suzuki, and Y. Kobayashi, “Single-Walled Carbon Nanotube Growth from Highly Activated Metal Nanoparticles,” *Nano Lett.*, vol. 6, no. 12, pp. 2642–2645, Dec. 2006.
- [93] H. Yoshida, S. Takeda, T. Uchiyama, H. Kohno, and Y. Homma, “Atomic-Scale In-situ Observation of Carbon Nanotube Growth from Solid State Iron Carbide Nanoparticles,” *Nano Lett.*, vol. 8, no. 7, pp. 2082–2086, Jul. 2008.
- [94] M. R. Berber, T. Fujigaya, K. Sasaki, and N. Nakashima, “Remarkably Durable High Temperature Polymer Electrolyte Fuel Cell Based on Poly(vinylphosphonic acid)-doped Polybenzimidazole,” *Sci. Rep.*, vol. 3, p. 1764, May 2013.

- [95] Z. Liu, K. Suenaga, P. J. F. Harris, and S. Iijima, "Open and Closed Edges of Graphene Layers," *Phys. Rev. Lett.*, vol. 102, no. 1, p. 15501, Jan. 2009.
- [96] K. Suenaga, Y. Sato, Z. Liu, H. Kataura, T. Okazaki, K. Kimoto, H. Sawada, T. Sasaki, K. Omoto, T. Tomita, T. Kaneyama, and Y. Kondo, "Visualizing and identifying single atoms using electron energy-loss spectroscopy with low accelerating voltage," *Nat. Chem.*, vol. 1, no. 5, pp. 415–418, Aug. 2009.
- [97] C. Jin, H. Lan, L. Peng, K. Suenaga, and S. Iijima, "Deriving Carbon Atomic Chains from Graphene," *Phys. Rev. Lett.*, vol. 102, no. 20, p. 205501, May 2009.
- [98] T. Sasaki, H. Sawada, F. Hosokawa, Y. Kohno, T. Tomita, T. Kaneyama, Y. Kondo, K. Kimoto, Y. Sato, and K. Suenaga, "Performance of low-voltage STEM/TEM with delta corrector and cold field emission gun," *J. Electron Microsc.*, vol. 59, no. S1, pp. S7–S13, Aug. 2010.
- [99] K. Suenaga and M. Koshino, "Atom-by-atom spectroscopy at graphene edge," *Nature*, vol. 468, no. 7327, pp. 1088–1090, Dec. 2010.
- [100] M. Koshino, Y. Niimi, E. Nakamura, H. Kataura, T. Okazaki, K. Suenaga, and S. Iijima, "Analysis of the reactivity and selectivity of fullerene dimerization reactions at the atomic level," *Nat. Chem.*, vol. 2, no. 2, pp. 117–124, Feb. 2010.
- [101] Z. Liu, K. Suenaga, Z. Wang, Z. Shi, E. Okunishi, and S. Iijima, "Identification of active atomic defects in a monolayered tungsten disulphide nanoribbon," *Nat. Commun.*, vol. 2, p. 213, Mar. 2011.
- [102] J. H. Warner, Z. Liu, K. He, A. W. Robertson, and K. Suenaga, "Sensitivity of Graphene Edge States to Surface Adatom Interactions," *Nano Lett.*, vol. 13, no. 10, pp. 4820–4826, Oct. 2013.
- [103] O. Cretu, H.-P. Komsa, O. Lehtinen, G. Algara-Siller, U. Kaiser, K. Suenaga, and A. V. Krasheninnikov, "Experimental Observation of Boron Nitride Chains," *ACS Nano*, vol. 8, no. 12, pp. 11950–11957, Dec. 2014.
- [104] J. H. Warner, Y. Lin, K. He, M. Koshino, K. Suenaga, and W. E. T. Al, "Stability and Spectroscopy of Single Nitrogen Dopants in Graphene at Elevated Temperatures," *ACS Nano*, vol. 8, no. 11, pp. 11806–11815, 2014.
- [105] Z. Liu, Y.-C. Lin, C.-C. Lu, C.-H. Yeh, P.-W. Chiu, S. Iijima, and K. Suenaga, "In situ observation of step-edge in-plane growth of graphene in a STEM," *Nat. Commun.*, vol. 5, no. May, p. 4055, Jun. 2014.
- [106] K. He, A. W. Robertson, Y. Fan, C. S. Allen, Y.-C. Lin, K. Suenaga, A. I. Kirkland, and J. H. Warner, "Temperature Dependence of the Reconstruction of Zigzag Edges in Graphene," *ACS Nano*, vol. 9, no. 5, pp. 4786–4795, May 2015.
- [107] R. Senga and K. Suenaga, "Single-atom electron energy loss spectroscopy of light elements," *Nat. Commun.*, vol. 6, p. 7943, Jul. 2015.
- [108] H. Sawada, T. Sasaki, F. Hosokawa, and K. Suenaga, "Atomic-Resolution STEM Imaging of Graphene at Low Voltage of 30 kV with Resolution Enhancement by Using Large Convergence Angle," *Phys. Rev. Lett.*, vol. 114, no. 16, p. 166102, Apr. 2015.

- [109] S. Morishita, M. Mukai, K. Suenaga, and H. Sawada, “Atomic Resolution Imaging at an Ultralow Accelerating Voltage by a Monochromatic Transmission Electron Microscope,” *Phys. Rev. Lett.*, vol. 117, no. 15, p. 153004, Oct. 2016.
- [110] A. V. Krasheninnikov, F. Banhart, J. X. Li, A. S. Foster, and R. M. Nieminen, “Stability of carbon nanotubes under electron irradiation: Role of tube diameter and chirality,” *Phys. Rev. B*, vol. 72, no. 12, p. 125428, Sep. 2005.
- [111] A. Zobelli, A. Gloter, C. P. Ewels, G. Seifert, and C. Colliex, “Electron knock-on cross section of carbon and boron nitride nanotubes,” *Phys. Rev. B*, vol. 75, no. 24, p. 245402, Jun. 2007.
- [112] L. Li, S. Reich, and J. Robertson, “Defect energies of graphite: Density-functional calculations,” *Phys. Rev. B*, vol. 72, no. 18, p. 184109, Nov. 2005.
- [113] A. V. Krasheninnikov, P. O. Lehtinen, A. S. Foster, P. Pyykkö, and R. M. Nieminen, “Embedding Transition-Metal Atoms in Graphene: Structure, Bonding, and Magnetism,” *Phys. Rev. Lett.*, vol. 102, no. 12, p. 126807, Mar. 2009.
- [114] E. J. G. Santos, A. Ayuela, and D. Sánchez-Portal, “First-principles study of substitutional metal impurities in graphene: structural, electronic and magnetic properties,” *New J. Phys.*, vol. 12, no. 5, p. 53012, May 2010.
- [115] J. C. Meyer, J. Kotakoski, and C. Mangler, “Atomic structure from large-area, low-dose exposures of materials: A new route to circumvent radiation damage,” *Ultramicroscopy*, vol. 145, pp. 13–21, Oct. 2014.
- [116] R. S. Pantelic, J. W. Suk, Y. Hao, R. S. Ruoff, and H. Stahlberg, “Oxidative Doping Renders Graphene Hydrophilic, Facilitating Its Use As a Support in Biological TEM,” *Nano Lett.*, vol. 11, no. 10, pp. 4319–4323, Oct. 2011.
- [117] O. V. Yazyev and A. Pasquarello, “Metal adatoms on graphene and hexagonal boron nitride: Towards rational design of self-assembly templates,” *Phys. Rev. B*, vol. 82, no. 4, p. 45407, Jul. 2010.
- [118] A. W. Robertson, C. S. Allen, Y. A. Wu, K. He, J. Olivier, J. Neethling, A. I. Kirkland, and J. H. Warner, “Spatial control of defect creation in graphene at the nanoscale,” *Nat. Commun.*, vol. 3, p. 1144, Oct. 2012.
- [119] A. V. Krasheninnikov and F. Banhart, “Engineering of nanostructured carbon materials with electron or ion beams,” *Nat. Mater.*, vol. 6, no. 10, pp. 723–733, Oct. 2007.
- [120] J. H. Warner and M. Rummeli, “Direct imaging of rotational stacking faults in few layer graphene,” *Nano Lett.*, vol. 9, no. 1, pp. 102–106, 2009.
- [121] B. W. Smith and D. E. Luzzi, “Electron irradiation effects in single wall carbon nanotubes,” *J. Appl. Phys.*, vol. 90, no. 7, pp. 3509–3015, 2001.
- [122] K. Suenaga, H. Wakabayashi, M. Koshino, Y. Sato, K. Urita, and S. Iijima, “Imaging active topological defects in carbon nanotubes,” *Nat. Nanotechnol.*, vol. 2, no. 6, pp. 358–360, Jun. 2007.

- [123] A. W. Robertson and J. H. Warner, “Atomic resolution imaging of graphene by transmission electron microscopy,” *Nanoscale*, vol. 5, no. 10, pp. 4079–4093, May 2013.
- [124] A. A. El-Barbary, R. H. Telling, C. P. Ewels, M. I. Heggie, and P. R. Briddon, “Structure and energetics of the vacancy in graphite,” *Phys. Rev. B*, vol. 68, no. 14, p. 144107, Oct. 2003.
- [125] J. H. Warner, E. R. Margine, M. Mukai, A. W. Robertson, F. Giustino, and A. I. Kirkland, “Dislocation-Driven Deformations in Graphene,” *Science*, vol. 337, no. 6091, pp. 209–212, Jul. 2012.
- [126] J. Kotakoski, A. V. Krasheninnikov, U. Kaiser, and J. C. Meyer, “From Point Defects in Graphene to Two-Dimensional Amorphous Carbon,” *Phys. Rev. Lett.*, vol. 106, no. 10, p. 105505, Mar. 2011.
- [127] F. R. Eder, J. Kotakoski, U. Kaiser, and J. C. Meyer, “A journey from order to disorder — Atom by atom transformation from graphene to a 2D carbon glass,” *Sci. Rep.*, vol. 4, p. 4060, Feb. 2014.
- [128] K. He, A. W. Robertson, S. Lee, E. Yoon, G. Lee, and J. H. Warner, “Extended Klein Edges in Graphene,” *ACS Nano*, vol. 8, no. 12, pp. 12272–12279, Dec. 2014.
- [129] H. E. Troiani, M. Miki-Yoshida, G. A. Camacho-Bragado, M. A. L. Marques, A. Rubio, J. A. Ascencio, and M. Jose-Yacamán, “Direct Observation of the Mechanical Properties of Single-Walled Carbon Nanotubes and Their Junctions at the Atomic Level,” *Nano Lett.*, vol. 3, no. 6, pp. 751–755, Jun. 2003.
- [130] A. Chuvilin, J. C. Meyer, G. Algara-Siller, and U. Kaiser, “From graphene constrictions to single carbon chains,” *New J. Phys.*, vol. 11, no. 8, p. 83019, Aug. 2009.
- [131] G. Casillas, A. Mayoral, M. Liu, A. Ponce, V. I. Artyukhov, B. I. Yakobson, and M. Jose-Yacamán, “New insights into the properties and interactions of carbon chains as revealed by HRTEM and DFT analysis,” *Carbon*, vol. 66, pp. 436–441, Jan. 2014.
- [132] A. La Torre, A. Botello-Mendez, W. Baaziz, J.-C. Charlier, and F. Banhart, “Strain-induced metal–semiconductor transition observed in atomic carbon chains,” *Nat. Commun.*, vol. 6, p. 6636, Mar. 2015.
- [133] J. Lin, O. Cretu, W. Zhou, K. Suenaga, D. Prasai, K. I. Bolotin, N. T. Cuong, M. Otani, S. Okada, A. R. Lupini, J.-C. Idrobo, D. Caudel, A. Burger, N. J. Ghimire, J. Yan, D. G. Mandrus, S. J. Pennycook, and S. T. Pantelides, “Flexible metallic nanowires with self-adaptive contacts to semiconducting transition-metal dichalcogenide monolayers,” *Nat. Nanotechnol.*, vol. 9, no. 6, pp. 436–442, Apr. 2014.
- [134] M. Kertesz, J. Koller, and A. Aman, “Ab initio Hartree–Fock crystal orbital studies. II. Energy bands of an infinite carbon chain,” *J. Chem. Phys.*, vol. 68, no. 6, pp. 2779–2782, 1978.
- [135] F. Banhart, “Chains of carbon atoms: A vision or a new nanomaterial?,” *Beilstein J. Nanotechnol.*, vol. 6, pp. 559–569, 2015.
- [136] R. Zan, Q. M. Ramasse, U. Bangert, and K. S. Novoselov, “Graphene Reknits Its Holes,” *Nano Lett.*, vol. 12, no. 8, pp. 3936–3940, Aug. 2012.
- [137] B. Westenfelder, J. C. Meyer, J. Biskupek, S. Kurasch, F. Scholz, C. E. Krill, and U. Kaiser, “Transformations of Carbon Adsorbates on Graphene Substrates under Extreme Heat,” *Nano Lett.*, vol. 11, no. 12, pp. 5123–5127, Dec. 2011.

- [138] W. L. Wang, E. J. G. Santos, B. Jiang, E. D. Cubuk, C. Ophus, A. Centeno, A. Pesquera, A. Zurutuza, J. Ciston, R. Westervelt, and E. Kaxiras, “Direct Observation of a Long-Lived Single-Atom Catalyst Chiseling Atomic Structures in Graphene,” *Nano Lett.*, vol. 14, no. 2, pp. 450–455, Feb. 2014.
- [139] J. Lee, W. Zhou, S. J. Pennycook, J.-C. Idrobo, and S. T. Pantelides, “Direct visualization of reversible dynamics in a Si₆ cluster embedded in a graphene pore,” *Nat. Commun.*, vol. 4, p. 1650, Apr. 2013.
- [140] Z. Yang, L. Yin, J. Lee, W. Ren, H.-M. Cheng, H. Ye, S. T. Pantelides, S. J. Pennycook, and M. F. Chisholm, “Direct Observation of Atomic Dynamics and Silicon Doping at a Topological Defect in Graphene,” *Angew. Chemie Int. Ed.*, vol. 53, no. 34, pp. 8908–8912, Aug. 2014.
- [141] J. Lee, Z. Yang, W. Zhou, S. J. Pennycook, S. T. Pantelides, and M. F. Chisholm, “Stabilization of graphene nanopore,” *Proc. Natl. Acad. Sci.*, vol. 111, no. 21, pp. 7522–7526, May 2014.
- [142] Q. Chen, A. W. Robertson, K. He, C. Gong, E. Yoon, A. I. Kirkland, G.-D. Lee, and J. H. Warner, “Elongated Silicon–Carbon Bonds at Graphene Edges,” *ACS Nano*, vol. 10, no. 1, pp. 142–149, Jan. 2016.
- [143] Y. Shao, G. Yin, and Y. Gao, “Understanding and approaches for the durability issues of Pt-based catalysts for PEM fuel cell,” *J. Power Sources*, vol. 171, no. 2, pp. 558–566, Sep. 2007.
- [144] K. Yoshida, S. Arai, Y. Sasaki, and N. Tanaka, “Catalytic behavior of noble metal nanoparticles for the hydrogenation and oxidation of multiwalled carbon nanotubes,” *Microscopy*, vol. 65, no. 4, pp. 309–315, Aug. 2016.
- [145] L. Ci, Z. Xu, L. Wang, W. Gao, F. Ding, K. F. Kelly, B. I. Yakobson, and P. M. Ajayan, “Controlled nanocutting of graphene,” *Nano Res.*, vol. 1, no. 2, pp. 116–122, Aug. 2008.
- [146] L. C. Campos, V. R. Manfrinato, J. D. Sanchez-Yamagishi, J. Kong, and P. Jarillo-Herrero, “Anisotropic Etching and Nanoribbon Formation in Single-Layer Graphene,” *Nano Lett.*, vol. 9, no. 7, pp. 2600–2604, Jul. 2009.
- [147] F. Schäffel, M. Wilson, A. Bachmatiuk, M. H. Rummeli, U. Queitsch, B. Rellinghaus, G. A. D. Briggs, and J. H. Warner, “Atomic Resolution Imaging of the Edges of Catalytically Etched Suspended Few-Layer Graphene,” *ACS Nano*, vol. 5, no. 3, pp. 1975–1983, Mar. 2011.
- [148] F. Pizzocchero, M. Vanin, J. Kling, T. W. Hansen, K. W. Jacobsen, P. Bøggild, and T. J. Booth, “Graphene Edges Dictate the Morphology of Nanoparticles during Catalytic Channeling,” *J. Phys. Chem. C*, vol. 118, no. 8, pp. 4296–4302, Feb. 2014.
- [149] H. Cao, X. Zhou, C. Zheng, and Z. Liu, “Metal etching method for preparing porous graphene as high performance anode material for lithium-ion batteries,” *Carbon*, vol. 89, pp. 41–46, Aug. 2015.
- [150] A. W. Robertson, B. Montanari, K. He, J. Kim, C. S. Allen, Y. A. Wu, J. Olivier, J. Neethling, N. Harrison, A. I. Kirkland, and J. H. Warner, “Dynamics of Single Fe Atoms in Graphene Vacancies,” *Nano Lett.*, vol. 13, no. 4, pp. 1468–1475, Apr. 2013.

- [151] Z. He, K. He, A. W. Robertson, A. I. Kirkland, D. Kim, J. Ihm, E. Yoon, G.-D. Lee, and J. H. Warner, “Atomic Structure and Dynamics of Metal Dopant Pairs in Graphene,” *Nano Lett.*, vol. 14, no. 7, pp. 3766–3772, Jul. 2014.
- [152] H. Wang, Q. Wang, Y. Cheng, K. Li, Y. Yao, Q. Zhang, C. Dong, P. Wang, U. Schwingenschlögl, W. Yang, and X. X. Zhang, “Doping Monolayer Graphene with Single Atom Substitutions,” *Nano Lett.*, vol. 12, no. 1, pp. 141–144, Jan. 2012.
- [153] H. Wang, K. Li, Y. Cheng, Q. Wang, Y. Yao, U. Schwingenschlögl, X. Zhang, and W. Yang, “Interaction between single gold atom and the graphene edge: A study via aberration-corrected transmission electron microscopy,” *Nanoscale*, vol. 4, no. 9, pp. 2920–2925, 2012.
- [154] J. Zhao, Q. Deng, S. M. Avdoshenko, L. Fu, J. Eckert, and M. H. Rummeli, “Direct in situ observations of single Fe atom catalytic processes and anomalous diffusion at graphene edges,” *Proc. Natl. Acad. Sci.*, vol. 111, no. 44, pp. 15641–15646, Nov. 2014.
- [155] Q. M. Ramasse, R. Zan, U. Bangert, D. W. Boukhvalov, Y.-W. Son, and K. S. Novoselov, “Direct Experimental Evidence of Metal-Mediated Etching of Suspended Graphene,” *ACS Nano*, vol. 6, no. 5, pp. 4063–4071, May 2012.
- [156] J. Zhao, Q. Deng, A. Bachmatiuk, G. Sandeep, A. Popov, J. Eckert, and M. H. Rummeli, “Free-Standing Single-Atom-Thick Iron Membranes Suspended in Graphene Pores,” *Science*, vol. 343, no. 6176, pp. 1228–1232, Mar. 2014.
- [157] Q. Chen, A. L. Koh, A. W. Robertson, K. He, S. Lee, E. Yoon, G. Do Lee, R. Sinclair, and J. H. Warner, “Rotating Anisotropic Crystalline Silicon Nanoclusters in Graphene,” *ACS Nano*, vol. 9, no. 10, pp. 9497–9506, 2015.
- [158] M. Haider, P. Hartel, H. Muller, S. Uhlemann, and J. Zach, “Current and future aberration correctors for the improvement of resolution in electron microscopy,” *Philos. Trans. R. Soc. A*, vol. 367, no. 1903, pp. 3665–3682, Sep. 2009.
- [159] O. L. Krivanek, N. Dellby, and A. R. Lupini, “Towards sub-Å electron beams,” *Ultramicroscopy*, vol. 78, pp. 1–11, 1999.
- [160] D. A. Muller, “Structure and bonding at the atomic scale by scanning transmission electron microscopy,” *Nat. Mater.*, vol. 8, no. 4, pp. 263–270, Apr. 2009.
- [161] O. L. Krivanek, M. F. Chisholm, V. Nicolosi, T. J. Pennycook, G. J. Corbin, N. Dellby, M. F. Murfitt, C. S. Own, Z. S. Szilagy, M. P. Oxley, S. T. Pantelides, and S. J. Pennycook, “Atom-by-atom structural and chemical analysis by annular dark-field electron microscopy,” *Nature*, vol. 464, no. 7288, pp. 571–574, Mar. 2010.
- [162] D. Kepaptsoglou, T. P. Hardcastle, C. R. Seabourne, U. Bangert, R. Zan, J. A. Amani, H. Hofsäss, R. J. Nicholls, R. M. D. Brydson, A. J. Scott, and Q. M. Ramasse, “Electronic Structure Modification of Ion Implanted Graphene: The Spectroscopic Signatures of p- and n-Type Doping,” *ACS Nano*, vol. 9, no. 11, pp. 11398–11407, Nov. 2015.

- [163] R. J. Nicholls, A. T. Murdock, J. Tsang, J. Britton, T. J. Pennycook, A. Koós, P. D. Nellist, N. Grobert, and J. R. Yates, “Probing the Bonding in Nitrogen-Doped Graphene Using Electron Energy Loss Spectroscopy,” *ACS Nano*, vol. 7, no. 8, pp. 7145–7150, Aug. 2013.
- [164] J. S. Reid, “Debye–Waller factors of zinc-blende-structure materials – a lattice dynamical comparison,” *Acta Cryst.*, vol. 39, no. 1, pp. 1–13, Jan. 1983.
- [165] V. F. Sears and S. A. Shelley, “Debye–Waller factor for elemental crystals,” *Acta Cryst.*, vol. 47, no. 4, pp. 441–446, Jul. 1991.
- [166] H. X. Gao and L.-M. Peng, “Parameterization of the temperature dependence of the Debye–Waller factors,” *Acta Cryst.*, vol. 55, no. 5, pp. 926–932, Sep. 1999.
- [167] J. C. Meyer, A. K. Geim, M. I. Katsnelson, K. S. Novoselov, D. Obergfell, S. Roth, Ç. Ö. Girit, and A. Zettl, “On the roughness of single- and bi-layer graphene membranes,” *Solid State Commun.*, vol. 143, no. 1–2, pp. 101–109, Jul. 2007.
- [168] P. Y. Huang, C. S. Ruiz-Vargas, A. M. van der Zande, W. S. Whitney, M. P. Levendorf, J. W. Kevek, S. Garg, J. S. Alden, C. J. Hustedt, Y. Zhu, J. Park, P. L. McEuen, and D. A. Muller, “Grains and grain boundaries in single-layer graphene atomic patchwork quilts,” *Nature*, vol. 469, no. 7330, pp. 389–392, Jan. 2011.
- [169] K. Kim, Z. Lee, W. Regan, C. Kisielowski, M. F. Crommie, and A. Zettl, “Grain Boundary Mapping in Polycrystalline Graphene,” *ACS Nano*, vol. 5, no. 3, pp. 2142–2146, Mar. 2011.
- [170] J. Lin, W. Fang, W. Zhou, A. R. Lupini, J. C. Idrobo, J. Kong, S. J. Pennycook, and S. T. Pantelides, “AC/AB Stacking Boundaries in Bilayer Graphene,” *Nano Lett.*, vol. 13, no. 7, pp. 3262–3268, Jul. 2013.
- [171] B. Shevitski, M. Mecklenburg, W. A. Hubbard, E. R. White, B. Dawson, M. S. Lodge, M. Ishigami, and B. C. Regan, “Dark-field transmission electron microscopy and the Debye-Waller factor of graphene,” *Phys. Rev. B*, vol. 87, no. 4, p. 45417, Jan. 2013.
- [172] K. Murakami, S. Tanaka, A. Hirukawa, T. Hiyama, T. Kuwajima, E. Kano, M. Takeguchi, and J. I. Fujita, “Direct synthesis of large area graphene on insulating substrate by gallium vapor-assisted chemical vapor deposition,” *Appl. Phys. Lett.*, vol. 106, p. 93112, 2015.
- [173] S. M. Shinde, E. Kano, G. Kalita, M. Takeguchi, A. Hashimoto, and M. Tanemura, “Grain structures of nitrogen-doped graphene synthesized by solid source-based chemical vapor deposition,” *Carbon*, vol. 96, pp. 448–453, 2016.
- [174] R. F. Egerton, *Energy loss spectroscopy*. .
- [175] R. D. Leapman, L. A. Grunes, and P. L. Fejes, “Study of the L23 edges in the 3d transition metals and their oxides by electron-energy-loss spectroscopy with comparisons to theory,” *Phys. Rev. B*, vol. 26, pp. 614–635, 1982.
- [176] S. L. Hulbert, B. A. Bunker, F. C. Brown, and P. Pianetta, “Copper L2,3 near-edge structure in Cu2O,” *Phys. Rev. B*, vol. 30, no. 4, pp. 2120–2126, Aug. 1984.

- [177] C. C. Ahn, *Transmission Electron Energy Loss Spectrometry in Materials Science and the EELS Atlas*. 2006.
- [178] L. Reimer and H. Kohl, *Transmission Electron Microscopy*, Fifth edit. Springer, 2008.
- [179] K. Kim, S. Coh, C. Kisielowski, M. F. Crommie, S. G. Louie, M. L. Cohen, and A. Zettl, “Atomically perfect torn graphene edges and their reversible reconstruction.,” *Nat. Commun.*, vol. 4, p. 2723, Nov. 2013.
- [180] G. Wang, B. Wang, J. Park, Y. Wang, B. Sun, and J. Yao, “Highly efficient and large-scale synthesis of graphene by electrolytic exfoliation,” *Carbon*, vol. 47, no. 14, pp. 3242–3246, 2009.
- [181] C.-Y. Su, A.-Y. Lu, Y. Xu, F.-R. Chen, A. N. Khlobystov, and L.-J. Li, “High-Quality Thin Graphene Films from Fast Electrochemical Exfoliation,” *ACS Nano*, vol. 5, no. 3, pp. 2332–2339, Mar. 2011.
- [182] J. N. Coleman, “Liquid Exfoliation of Defect-Free Graphene,” *Acc. Chem. Res.*, vol. 46, no. 1, pp. 14–22, Jan. 2013.
- [183] C. Gómez-Navarro, J. C. Meyer, R. S. Sundaram, A. Chuvilin, S. Kurasch, M. Burghard, K. Kern, and U. Kaiser, “Atomic Structure of Reduced Graphene Oxide,” *Nano Lett.*, vol. 10, no. 4, pp. 1144–1148, Apr. 2010.
- [184] Y. Hernandez, V. Nicolosi, M. Lotya, F. M. Blighe, Z. Sun, S. De, I. T. McGovern, B. Holland, M. Byrne, Y. K. Gun’Ko, J. J. Boland, P. Niraj, G. Duesberg, S. Krishnamurthy, R. Goodhue, J. Hutchison, V. Scardaci, A. C. Ferrari, and J. N. Coleman, “High-yield production of graphene by liquid-phase exfoliation of graphite,” *Nat. Nanotechnol.*, vol. 3, no. 9, pp. 563–568, Sep. 2008.
- [185] X. Li, W. Cai, L. Colombo, and R. S. Ruoff, “Evolution of Graphene Growth on Ni and Cu by Carbon Isotope Labeling,” *Nano Lett.*, vol. 9, no. 12, pp. 4268–4272, Dec. 2009.
- [186] W. Norimatsu and M. Kusunoki, “Formation process of graphene on SiC (0001),” *Phys. E Low-dimensional Syst. Nanostructures*, vol. 42, no. 4, pp. 691–694, Feb. 2010.
- [187] C. Mattevi, H. Kim, and M. Chhowalla, “A review of chemical vapour deposition of graphene on copper,” *J. Mater. Chem.*, vol. 21, no. 10, pp. 3324–3334, 2011.
- [188] X. Wang and Y. Shi, “CHAPTER 1. Fabrication Techniques of Graphene Nanostructures,” in *Nanofabrication and its Application in Renewable Energy*, no. 32, 2014, pp. 1–30.
- [189] C. Gong, A. W. Robertson, K. He, C. Ford, A. A. R. Watt, and J. H. Warner, “Interactions of Pb and Te atoms with graphene,” *Dalt. Trans.*, vol. 43, no. 20, pp. 7442–7448, Feb. 2014.
- [190] L. H. Karlsson, J. Birch, A. Mockute, A. S. Ingason, H. Q. Ta, M. H. Rummeli, J. Rosen, and P. O. Å. Persson, “Residue reduction and intersurface interaction on single graphene sheets,” *Carbon*, vol. 100, pp. 345–350, 2016.
- [191] J. W. Suk, A. Kitt, C. W. Magnuson, Y. Hao, S. Ahmed, J. An, A. K. Swan, B. B. Goldberg, and R. S. Ruoff, “Transfer of CVD-Grown Monolayer Graphene onto Arbitrary Substrates,” *ACS Nano*, vol. 5, no. 9, pp. 6916–6924, Sep. 2011.

- [192] G. Algara-Siller, O. Lehtinen, A. Turchanin, and U. Kaiser, “Dry-cleaning of graphene,” *Appl. Phys. Lett.*, vol. 104, no. 15, p. 153115, Apr. 2014.
- [193] J.-N. Longchamp, C. Escher, and H.-W. Fink, “Ultraclean freestanding graphene by platinum-metal catalysis,” *J. Vac. Sci. Technol. B Microelectron. Nanom. Struct.*, vol. 31, no. 2, p. 20605, 2013.
- [194] T. D. Yuzvinsky, A. M. Fennimore, W. Mickelson, C. Esquivias, and A. Zettl, “Precision cutting of nanotubes with a low-energy electron beam,” *Appl. Phys. Lett.*, vol. 86, no. 5, p. 53109, Jan. 2005.
- [195] K. Pi, K. M. McCreary, W. Bao, W. Han, Y. F. Chiang, Y. Li, S.-W. Tsai, C. N. Lau, and R. K. Kawakami, “Electronic doping and scattering by transition metals on graphene,” *Phys. Rev. B*, vol. 80, no. 7, p. 75406, Aug. 2009.
- [196] S. Saadi, F. Abild-Pedersen, S. Helveg, J. Sehested, B. Hinnemann, C. C. Appel, and J. K. Nørskov, “On the Role of Metal Step-Edges in Graphene Growth,” *J. Phys. Chem. C*, vol. 114, no. 25, pp. 11221–11227, Jul. 2010.
- [197] P. Han, K. Akagi, F. F. Canova, H. Mutoh, S. Shiraki, K. Iwaya, P. S. Weiss, N. Asao, and T. Hitosugi, “Bottom-Up Graphene-Nanoribbon Fabrication Reveals Chiral Edges and Enantioselectivity,” *ACS Nano*, vol. 8, no. 9, pp. 9181–9187, 2014.
- [198] J.-Y. Raty, F. Gygi, and G. Galli, “Growth of Carbon Nanotubes on Metal Nanoparticles: A Microscopic Mechanism from Ab Initio Molecular Dynamics Simulations,” *Phys. Rev. Lett.*, vol. 95, no. 9, p. 96103, Aug. 2005.
- [199] Z. Ning, Z. Chen, X. Du, R. Ran, W. Dong, and C. Chen, “Structural Stability, Electronic and Magnetic Properties of Cu Adsorption on Defected Graphene: A First Principles Study,” *J. Supercond. Nov. Magn.*, vol. 27, no. 1, pp. 115–120, Jan. 2014.
- [200] Q. Yu, L. A. Jauregui, W. Wu, R. Colby, J. Tian, Z. Su, H. Cao, Z. Liu, D. Pandey, D. Wei, T. F. Chung, P. Peng, N. P. Guisinger, E. A. Stach, J. Bao, S.-S. Pei, and Y. P. Chen, “Control and characterization of individual grains and grain boundaries in graphene grown by chemical vapour deposition,” *Nat. Mater.*, vol. 10, no. 6, pp. 443–449, Jun. 2011.
- [201] “<https://azuma.nims.go.jp/>.”
- [202] J. P. Perdew, K. Burke, and M. Ernzerhof, “Generalized Gradient Approximation Made Simple,” *Phys. Rev. Lett.*, vol. 77, no. 18, pp. 3865–3868, Oct. 1996.
- [203] D. Vanderbilt, “Soft self-consistent pseudopotentials in a generalized eigenvalue formalism,” *Phys. Rev. B*, vol. 41, no. 11, pp. 7892–7895, Apr. 1990.
- [204] H. J. Monkhorst and J. D. Pack, “Special points for Brillouin-zone integrations,” *Phys. Rev. B*, vol. 13, no. 12, pp. 5188–5192, Jun. 1976.
- [205] G. Henkelman, B. P. Uberuaga, and H. Jónsson, “A climbing image nudged elastic band method for finding saddle points and minimum energy paths,” *J. Chem. Phys.*, vol. 113, no. 22, pp. 9901–9904, 2000.

- [206] S. Malola, H. Häkkinen, and P. Koskinen, “Gold in graphene: In-plane adsorption and diffusion,” *Appl. Phys. Lett.*, vol. 94, no. 4, p. 43106, 2009.
- [207] O. Lehtinen, N. Vats, G. Algara-Siller, P. Knyrim, and U. Kaiser, “Implantation and Atomic-Scale Investigation of Self-Interstitials in Graphene,” *Nano Lett.*, vol. 15, no. 1, pp. 235–241, Jan. 2015.
- [208] J. Ma, D. Alfè, A. Michaelides, and E. Wang, “Stone-Wales defects in graphene and other planar sp²-bonded materials,” *Phys. Rev. B*, vol. 80, no. 3, p. 33407, Jul. 2009.
- [209] W. Zhang, L. Sun, Z. Xu, A. V. Krasheninnikov, P. Huai, Z. Zhu, and F. Banhart, “Migration of gold atoms in graphene ribbons: Role of the edges,” *Phys. Rev. B*, vol. 81, no. 12, p. 125425, Mar. 2010.
- [210] P. Koskinen, S. Malola, and H. Häkkinen, “Self-passivating edge reconstructions of graphene,” *Phys. Rev. Lett.*, vol. 101, no. 11, p. 115502, Sep. 2008.
- [211] D. W. Boukhvalov and M. I. Katsnelson, “Destruction of graphene by metal adatoms,” *Appl. Phys. Lett.*, vol. 95, no. 2, p. 23109, 2009.
- [212] U. Bangert and R. Zan, “Electronic functionalisation of graphene via external doping and dosing,” *Int. Mater. Rev.*, vol. 60, no. 3, pp. 133–149, Apr. 2015.
- [213] M. Wu, E.-Z. Liu, M. Y. Ge, and J. Z. Jiang, “Stability, electronic, and magnetic behaviors of Cu adsorbed graphene: A first-principles study,” *Appl. Phys. Lett.*, vol. 94, no. 10, p. 102505, 2009.
- [214] J. Kotakoski, D. Santos-Cottin, and A. V. Krasheninnikov, “Stability of Graphene Edges under Electron Beam: Equilibrium Energetics versus Dynamic Effects,” *ACS Nano*, vol. 6, no. 1, pp. 671–676, Jan. 2012.
- [215] K. Kong, Y. Choi, B.-H. Ryu, J.-O. Lee, and H. Chang, “Investigation of metal/carbon-related materials for fuel cell applications by electronic structure calculations,” *Mater. Sci. Eng. C*, vol. 26, no. 5–7, pp. 1207–1210, Jul. 2006.
- [216] K. Okazaki-Maeda, Y. Morikawa, S. Tanaka, and M. Kohyama, “Structures of Pt clusters on graphene by first-principles calculations,” *Surf. Sci.*, vol. 604, no. 2, pp. 144–154, Jan. 2010.
- [217] I. Fampiou and A. Ramasubramaniam, “Binding of Pt Nanoclusters to Point Defects in Graphene: Adsorption, Morphology, and Electronic Structure,” *J. Phys. Chem. C*, vol. 116, no. 11, pp. 6543–6555, Mar. 2012.
- [218] M. Liu, V. I. Artyukhov, H. Lee, F. Xu, and B. I. Yakobson, “Carbyne from First Principles: Chain of C Atoms, a Nanorod or a Nanorope,” *ACS Nano*, vol. 7, no. 11, pp. 10075–10082, Nov. 2013.
- [219] H. Dai, J. Kong, C. Zhou, N. Franklin, T. Tombler, A. Cassell, S. Fan, and M. Chapline, “Controlled Chemical Routes to Nanotube Architectures, Physics, and Devices,” *J. Phys. Chem. B*, vol. 103, no. 51, pp. 11246–11255, Dec. 1999.
- [220] D. Yuan, L. Ding, H. Chu, Y. Feng, T. P. McNicholas, and J. Liu, “Horizontally Aligned Single-Walled Carbon Nanotube on Quartz from a Large Variety of Metal Catalysts,” *Nano Lett.*, vol. 8, no. 8, pp. 2576–2579, Aug. 2008.

- [221] C. S. Casari, A. Li Bassi, L. Ravagnan, F. Siviero, C. Lenardi, P. Piseri, G. Bongiorno, C. E. Bottani, and P. Milani, “Chemical and thermal stability of carbyne-like structures in cluster-assembled carbon films,” *Phys. Rev. B*, vol. 69, no. 7, p. 75422, Feb. 2004.
- [222] W. A. Chalifoux and R. R. Tykwinski, “Synthesis of polyynes to model the sp-carbon allotrope carbyne,” *Nat. Chem.*, vol. 2, no. 11, pp. 967–971, Nov. 2010.
- [223] Y. H. Hu, “Bending Effect of sp-Hybridized Carbon (Carbyne) Chains on Their Structures and Properties,” *J. Phys. Chem. C*, vol. 115, no. 5, pp. 1843–1850, Feb. 2011.
- [224] E. A. Belenkov and F. K. Shabiev, “Structure of new carbon phases from carbyne nanorings,” *Crystallogr. Reports*, vol. 52, no. 2, pp. 343–348, Mar. 2007.
- [225] N. Alem, R. Erni, C. Kisielowski, M. D. Rossell, W. Gannett, and A. Zettl, “Atomically thin hexagonal boron nitride probed by ultrahigh-resolution transmission electron microscopy,” *Phys. Rev. B*, vol. 80, no. 15, p. 155425, Oct. 2009.
- [226] L. Song, L. Ci, H. Lu, P. B. Sorokin, C. Jin, J. Ni, A. G. Kvashnin, D. G. Kvashnin, J. Lou, B. I. Yakobson, and P. M. Ajayan, “Large Scale Growth and Characterization of Atomic Hexagonal Boron Nitride Layers,” *Nano Lett.*, vol. 10, no. 8, pp. 3209–3215, Aug. 2010.
- [227] Q. H. Wang, K. Kalantar-Zadeh, A. Kis, J. N. Coleman, and M. S. Strano, “Electronics and optoelectronics of two-dimensional transition metal dichalcogenides,” *Nat. Nanotechnol.*, vol. 7, no. 11, pp. 699–712, Nov. 2012.
- [228] M. Osada and T. Sasaki, “Two-Dimensional Dielectric Nanosheets: Novel Nanoelectronics From Nanocrystal Building Blocks,” *Adv. Mater.*, vol. 24, no. 2, pp. 210–228, Jan. 2012.
- [229] R. Mas-Ballesté, C. Gómez-Navarro, J. Gómez-Herrero, and F. Zamora, “2D materials: to graphene and beyond,” *Nanoscale*, vol. 3, no. 1, pp. 20–30, 2011.
- [230] C. L. Freeman, F. Claeysens, N. L. Allan, and J. H. Harding, “Graphitic Nanofilms as Precursors to Wurtzite Films: Theory,” *Phys. Rev. Lett.*, vol. 96, no. 6, p. 66102, Feb. 2006.
- [231] P. B. Sorokin, A. G. Kvashnin, Z. Zhu, and D. Tománek, “Spontaneous Graphitization of Ultrathin Cubic Structures: A Computational Study,” *Nano Lett.*, vol. 14, no. 12, pp. 7126–7130, Dec. 2014.
- [232] H. T. Quang, A. Bachmatiuk, A. Dianat, F. Ortmann, J. Zhao, J. H. Warner, J. Eckert, G. Cuniberti, and M. H. Rummeli, “In Situ Observations of Free-Standing Graphene-like Mono- and Bilayer ZnO Membranes,” *ACS Nano*, vol. 9, no. 11, pp. 11408–11413, Nov. 2015.
- [233] Y. Shao, R. Pang, and X. Shi, “Stability of Two-Dimensional Iron Carbides Suspended across Graphene Pores: First-Principles Particle Swarm Optimization,” *J. Phys. Chem. C*, vol. 119, no. 40, pp. 22954–22960, Oct. 2015.
- [234] C. Tusche, H. L. Meyerheim, and J. Kirschner, “Observation of Depolarized ZnO(0001) Monolayers: Formation of Unreconstructed Planar Sheets,” *Phys. Rev. Lett.*, vol. 99, no. 2, p. 26102, Jul. 2007.
- [235] J. Lee, D. C. Sorescu, and X. Deng, “Tunable Lattice Constant and Band Gap of Single- and Few-Layer ZnO,” *J. Phys. Chem. Lett.*, vol. 7, no. 7, pp. 1335–1340, Apr. 2016.

- [236] P. E. Blöchl, “Projector augmented-wave method,” *Phys. Rev. B*, vol. 50, no. 24, pp. 17953–17979, Dec. 1994.
- [237] G. Kresse and J. Furthmüller, “Efficiency of ab-initio total energy calculations for metals and semiconductors using a plane-wave basis set,” *Comput. Mater. Sci.*, vol. 6, no. 1, pp. 15–50, Jul. 1996.
- [238] G. Kresse and J. Furthmüller, “Efficient iterative schemes for ab initio total-energy calculations using a plane-wave basis set,” *Phys. Rev. B*, vol. 54, no. 16, pp. 11169–11186, Oct. 1996.
- [239] G. Kresse and J. Hafner, “Ab initio molecular dynamics for liquid metals,” *Phys. Rev. B*, vol. 47, no. 1, pp. 558–561, Jan. 1993.
- [240] G. Kresse and J. Hafner, “Ab initio molecular-dynamics simulation of the liquid-metal–amorphous-semiconductor transition in germanium,” *Phys. Rev. B*, vol. 49, no. 20, pp. 14251–14269, May 1994.
- [241] W. G. Hoover, “Canonical dynamics: Equilibrium phase-space distributions,” *Phys. Rev. A*, vol. 31, no. 3, pp. 1695–1697, Mar. 1985.
- [242] S. Nosé, “A unified formulation of the constant temperature molecular dynamics methods,” *J. Chem. Phys.*, vol. 81, no. 1, pp. 511–519, 1984.
- [243] L.-M. Yang, T. Frauenheim, and E. Ganz, “The new dimension of silver,” *Phys. Chem. Chem. Phys.*, vol. 17, no. 30, pp. 19695–19699, 2015.
- [244] L.-M. Yang, M. Dornfeld, T. Frauenheim, and E. Ganz, “Glitter in a 2D monolayer,” *Phys. Chem. Chem. Phys.*, vol. 17, no. 39, pp. 26036–26042, 2015.
- [245] M. Heinemann, B. Eifert, and C. Heiliger, “Band structure and phase stability of the copper oxides Cu_2O , CuO , and Cu_4O_3 ,” *Phys. Rev. B*, vol. 87, no. 11, p. 115111, Mar. 2013.
- [246] C. Lee, X. Wei, J. W. Kysar, and J. Hone, “Measurement of the Elastic Properties and Intrinsic Strength of Monolayer Graphene,” *Science*, vol. 321, no. 5887, pp. 385–388, Jul. 2008.
- [247] Z. Fan, Z. Wei-Bing, and T. Bi-Yu, “Electronic structures and elastic properties of monolayer and bilayer transition metal dichalcogenides MX_2 ($M = \text{Mo}, \text{W}$; $X = \text{O}, \text{S}, \text{Se}, \text{Te}$): A comparative first-principles study,” *Chinese Phys. B*, vol. 24, no. 9, p. 97103, 2015.
- [248] J. Kang, S. Tongay, J. Zhou, J. Li, and J. Wu, “Band offsets and heterostructures of two-dimensional semiconductors,” *Appl. Phys. Lett.*, vol. 102, no. 1, p. 12111, 2013.
- [249] D. Çakır, F. M. Peeters, and C. Sevik, “Mechanical and thermal properties of h- MX_2 ($M = \text{Cr}, \text{Mo}, \text{W}$; $X = \text{O}, \text{S}, \text{Se}, \text{Te}$) monolayers: A comparative study,” *Appl. Phys. Lett.*, vol. 104, no. 20, p. 203110, May 2014.

Acknowledgements

First of all, I would like to express my sincere gratitude to Prof. Takashi Sekiguchi as my doctoral thesis chair, for his patience, continuous support of my study and review of this thesis. I owe my deepest appreciation to Associate Professor Ayako Hashimoto and Affiliate Professor Masaki Takeguchi as my supervisors. Without their persistent help, not only this thesis, but also my entire research life would not have been possible. I would also like to thank my thesis committee, Professor Junji Nakamura and Professor Jie Tang for their fruitful comments on my thesis.

I would like to thank my collaborators: Dr. Tomoaki Kaneko, Dr. Nobuo Tajima, Dr. Takahisa Ohno, Dr. Dmitry G. Kvashnin, Dr. Pavel B. Sorokin, Dr. Leonid A. Chernozatonskii and Dr. Seiji Sakai for their calculations and discussions related to this thesis and future collaborative studies. I am also grateful to Dr. Misa Hayashida and Dr. Marek Malac (including his family and lab members) for accepting me to visit Canada and carry out research there during last summer and in the near future.

During the past six years, since I was an undergraduate student, I had a great benefit to work with the members — not only the researchers, but also all staff — of TEM station at NIMS. Especially, I am deeply grateful to Dr. Konstantin Iakoubovskii for his prompt and precise proofreading of my research papers and Dr. Kazutaka Mitsuishi's group members for their valuable comments on my presentations in meetings. Furthermore, I sincerely express my appreciation to Hashimoto laboratory members: Ms. Yuki Nireki for her consistent care and assistance, and Mr. Hajime Akimoto for cooperation and studying together.

I acknowledge the financial support from NIMS as a NIMS Junior Researcher, from GREEN as a Long-term Research Assistant, and from JSPS as a JSPS Research Fellow. This supports allowed me to attend many international conferences.

Finally, I thank my parents for their continuous love, support and encouragement.

February 2017

Emi Kano